Master thesis and internship[BR]- Master's thesis : Boundary layer stability and shock interactions in a high-speed low pressure turbine cascade[BR]- Integration Internship : The von Karman Institute

Auteur : Borbouse, Maxime
Promoteur(s) : Hillewaert, Koen
Faculté : Faculté des Sciences appliquées
Diplôme : Master en ingénieur civil en aérospatiale, à finalité spécialisée en "aerospace engineering"
Année académique : 2022-2023
URI/URL : http://hdl.handle.net/2268.2/17744

UNIVERSITY OF LIÈGE - SCHOOL OF ENGINEERING

Boundary layer stability and shock interactions in a high-speed low pressure turbine cascade

————————

Master thesis presented by
Borbouse Maxime
in partial fulfillment of the requirements for the degree of Master of
Science in Aerospace Engineering

————————

Thesis supervisors
Professor Koen Hillewaert
University of Liège

Professor Sergio Lavagnoli
von Karman Institute for Fluid Dynamics

Jury members
Prof. Koen Hillewaert, Prof. Sergio Lavagnoli, Prof. Vincent Terrapon

Liège, Academic year 2022-2023

Abstract

A DNS numerical test case used the discontinuous Galerkin method and the Walloon super-computer Zenobe to study transonic aerodynamics of a linear low pressure turbine cascade, mimicking geared turbofan conditions during cruise. Separation, transition, and losses were examined at Mach 0.7, 0.9, and 0.95, with a constant Reynolds number of $70 \cdot 10^3$ based on the true chord. The objective was to understand blade behavior without inlet turbulence, comparing results to experimental data.

The pressure distribution was slightly overestimated. Separation occurs over the suction side (SS) at 58% and 69% of blade length for the first two Mach numbers. Skin friction is low in the Mach 0.95 case, but separation does not take place for this case. The shock was considered as influencing factor. Shock appears at Mach 0.9 or higher, with a choked passage at 0.95. Separation bubbles with turbulent reattachment are formed on the pressure side (PS) between 0% and 50% of the SS. Separation on the SS was identified as laminar separation long bubble, while reversed transition develops on the PS after reattachment.

Wake losses increase with higher Mach numbers, and turbulence is more prominent at lower Mach numbers. The turbulent decay is more important at low Mach. Vortex shedding frequencies were computed at 43 kHz, 52 kHz, and 59 kHz, and compared with Roshko correlation.

This investigation provided insights into the aerodynamic characteristics of the linear low pressure turbine cascade, addressing separation, transition, losses, and wake behavior.

Keywords: LPT, transonic, DNS, DGM, separation, transition, turbulence, shock

Acknowledgements

Contents

Chapter 1

Introduction

1.1 Motivations

In recent decades, turbofan engines have been of particular interest in the field of aeronautical research, with a specific aim: to optimize fuel efficiency. The engine efficiency can be increased through an increase of the thermodynamic efficiency and propulsive efficiency. They have been studied to such an extent that the turbine blades have reached high aerodynamics performance, leaving not many possibilities to further increase the propulsive efficiency. Current limitations in materials make the increase in thermodynamic efficiency quite challeging. Besides, propulsive efficiency still offers room for improvement, particularly through an increase of the engine bypass ratio as shown in Figure 1.1 (from [38]). Unfortunately, the size of
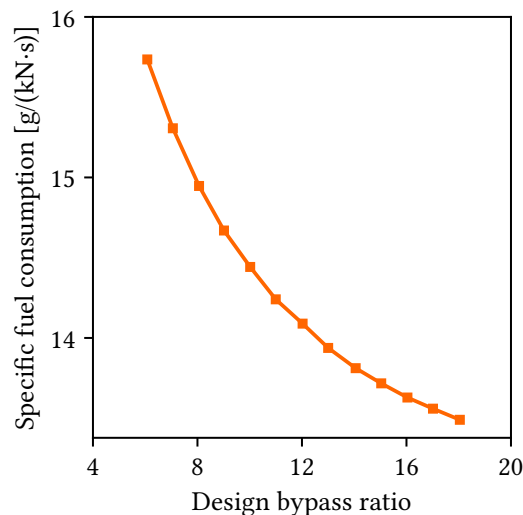
Figure 1.1: Specific fuel consumption with respect to the bypass ratio at an altitude of $35,000$ ft and at $M = 0.8$, reproduced from [38].

the fan itself is an important limitation: the larger the diameter, the faster the tip of the blade. Achieving transonic conditions at the blade tip can be problematic because efficiency is driven by compressibility effects. For a long time, the problem was avoided by restricting the speed of the low pressure shaft, which in turn restricted the speed of the low pressure turbine (LPT). In such engines, the low velocities of the turbine only permit a certain level of diffusion per stage, and therefore a lot of stages are necessary to provide a sufficient power to the fan for

compression. Alternatively, the radius of the flowpath in the LPT can be increased to extract more work. However, this cannot be done indefinitely. This high number of stages makes of the turbine an important contributor to the engine weight. The solution of curbing the low pressure shaft speed gave rise to a trade-off between propulsive efficiency, LPT efficiency and, indirectly, engine weight. This compromise can be circumvented by a way that has been proposed in 2008 by Pratt & Whitney[1] for the PW1000G, also called the *Geared Turbofan* (GTF), shown in Figure 1.2.
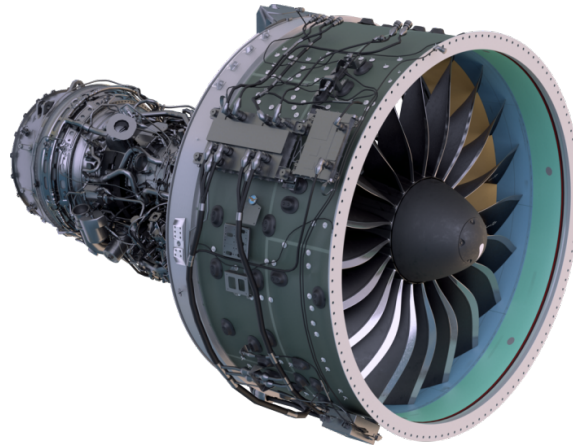
Figure 1.2: View of the Pratt & Whitney PW1000G geared turbofan, taken from [55].

The idea behind the GTF is to decouple the rotation of the fan from that of the turbine using a gearbox (see [38]). On one hand, this type of engine allows to decrease the specific fuel consumption (SFC), as soon as the bypass ratio is increased enough. But the main point of Kurzke [38] is the significant reduction in parts number that can be achieved for the GTF. The gearbox can bring some drawbacks since it transfers large amount of power in a harsh environment. The weight of the gearbox can also be a drawback if it's badly designed, otherwise it can considerably decrease the total weight of the engine by reducing the number of stages and blades in the LPT for the same diffusion level, the latter rotating at a higher speed. These are called the *high-speed low pressure turbines*. Since the weight of this type of engine is lower, the fuel consumption as well as the environmental impacts and the operational costs are reduced, which is of an important interest for the next generation of aircraft. Moreover, it authorizes savings in space.

The conditions met in high-speed low pressure turbines, that are not met in typical turbofans or turbojet, are transonic conditions and low Reynolds numbers. Loss mechanisms and blade aerodynamics are thus greatly driven by compressibility effects which may be critical. As discussed in several papers as [47, 50], the suction side (SS) boundary layer (BL) of the blade constitutes the greatest contribution in profile loss (up to 85%, see [50]). At these conditions, where the Reynolds number is low, separation could occur on the SS, causing a significant increase in losses. An example of separated flow in the rear portion of the SS of the T106 blade is shown in Figure 1.3.

To overcome this potential separation, it is possible to take advantage of turbulence and wake-induced transition as detailed in several works as [11, 14, 25, 33, 82]. These were a major interest in low pressure turbines and were explored for a large range of conditions. In cascade experimental cases, incoming wakes are generally studied by adding a wake generator (WG) which consists of bars rotating in front of the cascade. In addition to the experimental

---

[1] Actually, CMF International and GE Aviation considered this technology for the CMF LEAP. However, due to its heavy weight and lack of reliability, it hasn't been retained (see [76]).
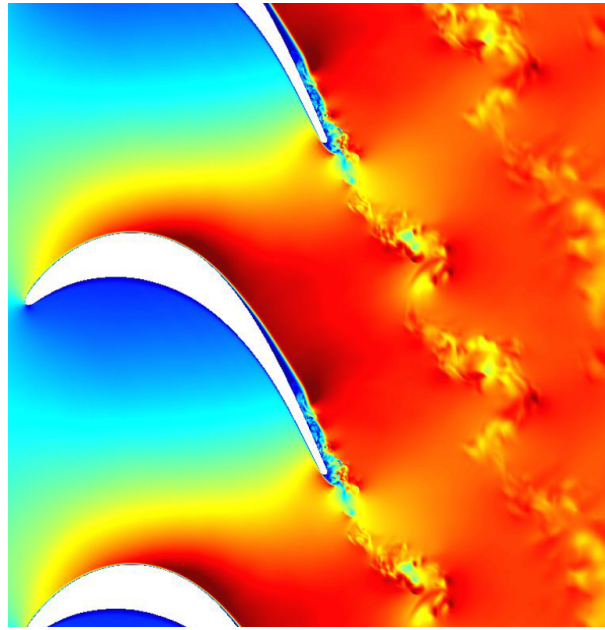
Figure 1.3: Mach number contour in the flow of a T106A cascade at Re $= 60 \cdot 10^3$ without free-stream turbulence, taken from [26].

study in such conditions, validating numerical studies are also performed. The occuring separation can either be an open separation (no reattachment) associated with high losses, or a closed bubble which can follow different modes. It can be controlled by passing wakes or by the type of blade, i.e. front or aft loaded. Transition can take place in different ways: natural, bypass, separated-flow, reverse or, as introduced above, wake-induced. Reattachment is allowed thanks to this transition and give rise to separation bubble. A description of the different typologies of separation bubbles is proposed in [45] and detailed studies of transition and separation are proposed in [24, 47]. By investigating the aerodynamics of the blades, the interest is to understand the state of BL at separation in order to understand the bubble mode it undergoes.

As regarded from a numerical point of view, the treated subject is not the easiest. Steady and unsteady Reynolds averaged Navier Stokes simulations (resp. RANS and URANS) as well as large eddy simulations (LES) suffer from difficulties in resolving transition, which is a problem for turbomachinery flows: those methods are much cheaper in terms of computational cost but do not allow to fully describe the features interacting in turbulent flows. For RANS and URANS, some turbulence models that are transition sensitive have been developed in [49, 50, 51, 59], based for the most on the intermittency or on the laminar kinetic energy (LKE) concepts. Those models are able to predict separation and bubble-bursting phenomenon. In order to understand and characterize transition, shocks and other complex mechanisms, high fidelity numerical methods have to be employed, otherwise the features of the flows can be missed. The most reliable way to do this is by direct numerical simulation (DNS) which allows to capture all the length scales of the flow at the expense of a high numerical cost. Lately, with the enhancements in numerical abilities and the development of high performance computing (HPC), turbomachinery flows have been easier to be computed. A method that has shown very good results in solving compressible flows is the discontinuous Galerkin method (DGM), which consitutes a higher order method combining strength of finite volume method (FVM) for convection-diffusion problem and finite element method (FEM).

The SPLEEN project (**S**econdary and Leakage Flow Effects in High-S**P**eed **L**ow Pr**E**ssur**E**

TurbiNe) headed by the von Karman Institute for Fluid Dynamics (VKI) in collaboration with SAFRAN and funded by the European Union's Horizon 2020 research and innovation program, has set itself the objective to investigate the aerodynamics of the next-generation high-speed LPT. The main interest in this document is therefore the aerodynamics of the blades at the on- and off-design conditions met in a GTF, especially cruise conditions. A high-fidelity experimental study on the subject was performed in [43, 44] and the results of this campaign are compared with DNS calculations in this thesis. The ultimate end of the project is to characterize the aerodynamics of high-speed LPTs under the impact of unsteady wakes and purge flows. Results should in turn aid the development of low-order models for profile and secondary losses, mature transition models, help validating high-order CFD codes and allow to design lighter LPT that achieve higher fuel and propulsive efficiency. Moreover, the project aims to fill the gap in available experimental and simulations data for on- and off-design conditions in high-speed LPT. Finally, this work can further be considered to validate the used method to study the flows in high-speed LPT by comparing experimental and DNS data. The focus in this thesis isn't the behavior of the cascade with incoming wakes, but the behavior and the effect of the blade itself, without any inlet turbulence. As the experimental analysis has already been performed, it is not a part of the objectives to provide its full analysis.

1.2   Methodology and overview

Studying the performances of a linear LPT cascade is a challenging task. On one hand, it has to be concise, i.e. the outputs must be easily usable by the designers, allowing them to conceptualize more efficient LPT blades. On the other hand, the physics must be understood as presicely as possible, which requires to dive deeper into details. To these ends, the tools used by the turbines designers and a description of the whole flow are to be provided. The first consideration concerns the foundations of the subject, the physics behind it and the state of the art. This is the goal of Chapter 2, dedicated to the descriptions of the physical and mathematical tools that are used troughout the thesis. It begins with a description of the operating conditions and the performance parameters. As introduced above, these are the most important considerations for designers. The two sections are followed by a series of sections detailing the encountered physics: turbulence, boundary layer, transition, shocks, von Karman vortex street. Subsequently, statistical tools used when dealing with turbulent flows are presented. It is completed by a state of the art, presenting the most important results to this date in LPT performances.

Since an experimental campaign was already undertaken, the second important topic to address is the test cases that were performed. This is the subject of Chapter 3 that goes through the experimental setup. The cascade design is introduced for the first time in this document. Moreover, the instrumentation is briefly described: the probes and the blade surface measurement techniques. The operating conditions of the test case are then detailed, using the concepts introduced in Chapter 2.

This directly leads to the main part of this work: the numerical contribution. Numerical tools as the environment and the used method is to be discussed. Most importantly, the setup has to be investigated and convergence must be reached. Besides, numerical computations also have limitations that have to be noted and are discussed in Chapter 4: HPC, ArgoDG (detailed in [9, 27]) and the simulation setup that was created and detailed in [6, 35].

Following the same line of thoughts, the penultimate chapter is dedicated to the presentation of results. The methodology that drives this thesis is quite straightforward, giving importance to intuition at first. In CFD of turbomachinery, an interesting feature to observe is the flow passage. Using a visualization tool such as ParaView, it is possible to visualize the flow

field quantities (Mach number, vorticity, density variations). It is this early glance on the flow that leads to the first tracks to understand the flow behavior. Loads acting on the blade are then computed and presented through the pressure distribution (or isentropic Mach number, see Chapter 2). Afterwards, BL is explored, characterizing separation and transition in the way of Hatman and Wang [24] along with Mayle [47]. Turbulent losses in the wake are presented and a loss breakdown following Denton [17] is achieved. Finally, a spectral analysis of the wake and the passage is performed with a view to explain some observed phenomena.

Chapter 2

Flow physics

Flow behavior in gas turbines was investigated in a lot of different configurations and conditions during the past years. The produced works showed that three main phenomena are impacting LPT performances: BL separation, transition and shocks. The former can have dramatic effects on turbine performance, especially when occuring on SS. Besides, transition is omnipresent in turbomachinery flows. One of the few components of turbomachines where the flow may be laminar is the LPT, generally experiencing low Reynolds numbers. Transition and separation are closely related: transition allows reattachment and may even permit to dodge it. In addition, at transonic conditions, the physics is in large part driven by compressibility effects and shocks. These can interact with the two aforementionned features.

As turbine performances are strongly impacted by the flow physics, it is of prime importance to introduce the concepts involved. A good visualization of the flow associated to the right mathematical tools are required to perform a reliable study of LPT. This chapter emphasizes on this science. Turbine designers make extensive use of operating conditions and performance parameters as they are the quantities which set the scales and quantify LPT efficiency. These are firstly reviewed. Fundamentals of fluid dynamics in turbines are then recalled: turbulence, boundary layer, transition, separation bubbles, shocks, wake. Statistical tools are then addressed. The chapter ends on a literature review of flows in low-pressure turbines. A particular focus is made on laminar-turbulent transition, loss in turbomachines and turbine trailing edge (base) flow. These central points are respectively supported by the work of Mayle [47], Denton [17] and Sieverding et al. [62].

2.1   Operating conditions

Turbines operating conditions are often defined by the inlet and outlet flow angles, the outlet isentropic Reynolds number and the outlet isentropic Mach number. The two latter allow to give an order of magnitude of turbulence and compressibility effects, respectively. The isentropic outlet Mach number is defined by

$$M_{\text{is,out}} = \sqrt{\frac{2}{\gamma - 1}\left[\left(\frac{p_{0,\text{in}}}{p_{\text{out}}}\right)^{\frac{\gamma-1}{\gamma}} - 1\right]}, \tag{2.1}$$

where $\gamma = 1.4$ is the heat capacity ratio[1], p_{out} is the outlet static pressure [Pa] and $p_{0,\text{in}}$ is the inlet total pressure [Pa]. It represents the ratio between the velocity and the speed of sound at

---

[1]Note that this assumption is acceptable for the studied conditions but it isn't allways the case.

the outlet computed with the perfect gas law and from static quantities. The outlet isentropic Reynolds number is mathematically defined as

$$\mathrm{Re}_{\mathrm{is,out}} = \frac{\rho_{\mathrm{is,out}} U_{\mathrm{is,out}} c}{\mu(T_{\mathrm{out}})}, \tag{2.2}$$

where $\rho_{\mathrm{is,out}}$ is the outlet isentropic density $[\mathrm{kg\,m^{-3}}]$, $U_{\mathrm{is,out}}$ is the outlet isentropic velocity magnitude $[\mathrm{m\,s^{-1}}]$, c is the blade chord $[\mathrm{m}]$ and $\mu(T_{\mathrm{out}})$ is the dynamic viscosity $[\mathrm{kg\,m^{-1}\,s^{-1}}]$ function of T_{out}, the outlet static temperature $[\mathrm{K}]$. It can be seen as the ratio between destibilizing inertia forces and stabilizing viscous forces: the greater the Reynolds number, the greater the instabilities, leading to transition and turbulence. In this thesis, by abuse of notation the subscripts are often dropped for these quantities, such that they are noted M and Re. When speaking of flow conditions of the LPT, we generally refer to both of these quantities together at the outlet. It is interesting to note that for compressors, inlet rather than outlet quantities are used. To compute them, the outlet isentropic density, the temperature and the viscosity are needed. The outlet isentropic density is given by the perfect gas law:

$$\rho_{\mathrm{is,out}} = \frac{p_{\mathrm{out}}}{R T_{\mathrm{out}}}, \tag{2.3}$$

where $R = 287.06\ [\mathrm{J\,kg^{-1}\,K^{-1}}]$ is the gas constant and the outlet static temperature is given by

$$T_{\mathrm{out}} = T_{0,\mathrm{in}} \left(1 + \frac{\gamma - 1}{2} M_{\mathrm{is,out}}^2 \right)^{-1}, \tag{2.4}$$

where $T_{0,\mathrm{in}}$ is the inlet total temperature $[\mathrm{K}]$. This allows to compute the outlet isentropic velocity:

$$U_{\mathrm{is,out}} = M_{\mathrm{is,out}} \sqrt{\gamma R T_{\mathrm{out}}}, \tag{2.5}$$

and the outlet isentropic dynamic viscosity, following the semi-empirical Sutherland's law, introduce by Sutherland [64] in 1893:

$$\mu_{\mathrm{is,out}} = \frac{1.458 \cdot 10^{-6} \cdot T_{\mathrm{out}}^{3/2}}{T_{\mathrm{out}} + 110.4}. \tag{2.6}$$

Low pressure turbine operating conditions have a substantial impact on their performance and reliability but also the blades durability. Geometry of the turbine blades is another crucial consideration to examine because it affects the flow patterns and turbulence intensity within the turbine, as well as the efficiency and longevity of the blades themselves. Finally, the turbine blades material qualities are crucial to their overall performance and durability. High-temperature alloys are commonly employed to survive the high temperatures (especially for high pressure turbines) and stresses experienced in turbines, but these materials can also be prone to creep, oxidation, and other forms of degradation over time. Careful consideration of the operating conditions is thus required to guarantee that the turbine blades are constructed and maintained in such a way that their performance and lifespan are maximized.

Research sector has already investigated a large range of Reynolds and Mach numbers for LPT since they are studied for several decades. However, as introduced above, new limiting losses technologies increasing the efficiency and reducing weight such as the GTF, make appear new conditions for which there is a lack of knowledge. Several works, especially experimental studies, considered high-speed LPT, e.g. [71, 72, 73, 74]. Börner and Niehuis [7] also worked on a blade designed to recreate the flow encountered in LPTs, i.e. separation bubble and supersonic conditions to investigate the impact of the shock on the BL. This thesis focuses on low Reynolds and transonic Mach numbers.

2.2 Performance parameters

Turbine designers are often interested in performances, loading of the blades and their calculations by means of simple parameters. This method has the benefit of being concise but fails to explain the complex features of the flow. The aim is to be able to design and fabricate LPT blades with optimal profiles depending on the physics without having to understand it in details. Even if this thesis focuses on the precise characteristics of the problem, it is important to introduce these parameters in order to state of the global performances of the cascade.

Aerodynamics tells us that the forces of the flow on a body originate from two contributions: pressure and shear stress. For this reason, blade aerodynamic performances are characterized by distributions of pressure and shear stress along the blade along with losses in the wake. The formers constitute the blade loading. A good practice in turbomachinery is to derive the isentropic Mach number from pressure distribution, which represents the velocity distribution outside the BL and is defined as

$$M_{\text{is}} = \sqrt{\frac{2}{\gamma - 1} \left[\left(\frac{p_{0,\text{in}}}{p} \right)^{\frac{\gamma - 1}{\gamma}} - 1 \right]}, \tag{2.7}$$

where p is the static pressure over the blade [Pa]. It has to be noted that the pressure coefficient

$$c_p = \frac{p - p_{\text{out}}}{(1/2)\rho_{\text{out}} U_{\text{out}}^2}, \tag{2.8}$$

where ρ_{out} and U_{out} are outlet characteristic (usually isentropic) quantities, and the pressure ratio p/p_{out} can be used equivalently. Nonetheless, the isentropic Mach number is used in this study since it provides a robust way to investigate blade loading. In addition it brings a quantification of the flow sonic behavior just outside the BL. Besides, it also permits to compare with the large number of studies that are using this parameter.

The other contribution to the loading is the wall shear stress acting over the surface and is defined as

$$\tau_w = \mu \frac{\partial u}{\partial y} \bigg|_{y=0}, \tag{2.9}$$

where μ [$\text{kg}\,\text{m}^{-1}\,\text{s}^{-1}$] is the dynamic viscosity of the fluid, u is the velocity parallel to the surface [$\text{m}\,\text{s}^{-1}$] and y is the distance from the surface [m]. The wall shear stress is non-dimensionalized to provide the skin-friction coefficient:

$$c_f = \frac{\tau_w}{(1/2)\rho_{\text{out}} U_{\text{out}}^2}. \tag{2.10}$$

It is used to predict separation and transition, as detailed in following sections.

Distributions may either be represented along the x-axis normalized by the axial chord of the blade c_{ax} or along the curvilinear length of the SS, noted S, normalized by the total length S_0 or S_L, which is more useful because a large extent of studies are performed with flat plates.

In addition to the investigation of blade loading, the wake has to be studied. Understanding the wake is at least as important as blade loading to have a complete description of performance. The energy and pressure loss coefficients are respectively defined as

$$\xi = 1 - \frac{1 - \left(\frac{p_{\text{out}}}{p_{0,\text{out}}} \right)^{\frac{\gamma - 1}{\gamma}}}{1 - \left(\frac{p_{\text{out}}}{p_{0,\text{in}}} \right)^{\frac{\gamma - 1}{\gamma}}}, \tag{2.11}$$

$$\zeta = \frac{p_{0,\text{out}} - p_{0,\text{in}}}{p_{0,\text{in}}}.$$

2.3 Turbulence

Turbulence is a random phenomenon characterized by vorticity, high rate of mixing, dissipation and large range of scales as detailed in [16, 20, 52, 68]. It is a large set of eddies that stretch and move accordingly to their induced velocity, with diffusion localized to regions of large vorticity gradients. Turbulence is a flow characteristic which comes from an increase in relative contribution of nonlinearities, i.e. increase in Reynolds number, and in turn increases the complexity of the flow.

Turbulence being chaotic and non reproducible, it is generally described by statistics. The most common method to treat the equations is the Reynolds averaged Navier-Stokes equations (NSE) consisting in introducing the Reynolds decomposition in the equations and average them. The idea behind the Reynolds decomposition is splitting the flow quantities between the average quantity and the small perturbation around this average, e.g. $u = U + u'$ for the x-component of the velocity, where U is the mean and u' it the small perturbation. Performing this method with the NSE leads to

$$\rho(\overline{\mathbf{u}} \cdot \mathbf{V})\overline{u}_i = -\frac{\partial \overline{p}}{\partial x_i} + \frac{\partial}{\partial x_j}\Big[\overline{\tau}_{ij} - \rho\overline{u_i'u_j'}\Big],\tag{2.12}$$

where $\tau_{ij} = \mu\partial u_i/\partial x_j$. The last term of the equation, $\tau_{ij}^R = -\rho\overline{u_i'u_j'}$, called the Reynolds stresses, is a turbulent quantity and comes directly from the non-linear inertia term. This tensor introduces a closure problem since these Reynolds stresses constitute a new unknown that has to be solved. From this quantity, the turbulent kinetic energy (TKE) can be derived as

$$k = \frac{1}{2}\overline{u_j'u_j'}.\tag{2.13}$$

The TKE is a useful way to quantify the turbulent degree of the flow. When defining operating conditions, turbine designers are also interested in the level of turbulence of the flow, specified by the inlet turbulence level, or the turbulence intensity:

$$\mathrm{Tu} = \frac{\sqrt{(2/3)k}}{U_\infty},\tag{2.14}$$

where U_∞ is a characteristic velocity (e.g. at the inlet if the computed quantity is the inlet free-stream turbulence). As discussed later in the document, inlet turbulence intensity plays a very important role when speaking of separation: the transition mechanisms can be completely different for two inlet turbulence levels.

2.3.1 Kolmogorov cascade and Taylor's hypothesis

In 1922, Richardson [56] suggested the qualitative idea of a turbulent cascade as the mechanism of energy transfer from the large to the small length scales. Kolmogorov [36] took back this idea in 1941 which led to the well known $-5/3$-law. This law, illustrated in Figure 2.1, comes directly from dimensional considerations and tells us that the energy spectrum $E(\kappa)$, κ being the wave number, is proportional to $\varepsilon^{2/3}\kappa^{-5/3}$, i.e.

$$E(\kappa) = \varepsilon^{2/3}\kappa^{-5/3},\tag{2.15}$$

where ε is the rate of energy of the cascade. Here it is expressed in Fourier space but it may also be expressed as the 2/3-law:

$$E(r) = (\varepsilon r)^{2/3},\tag{2.16}$$
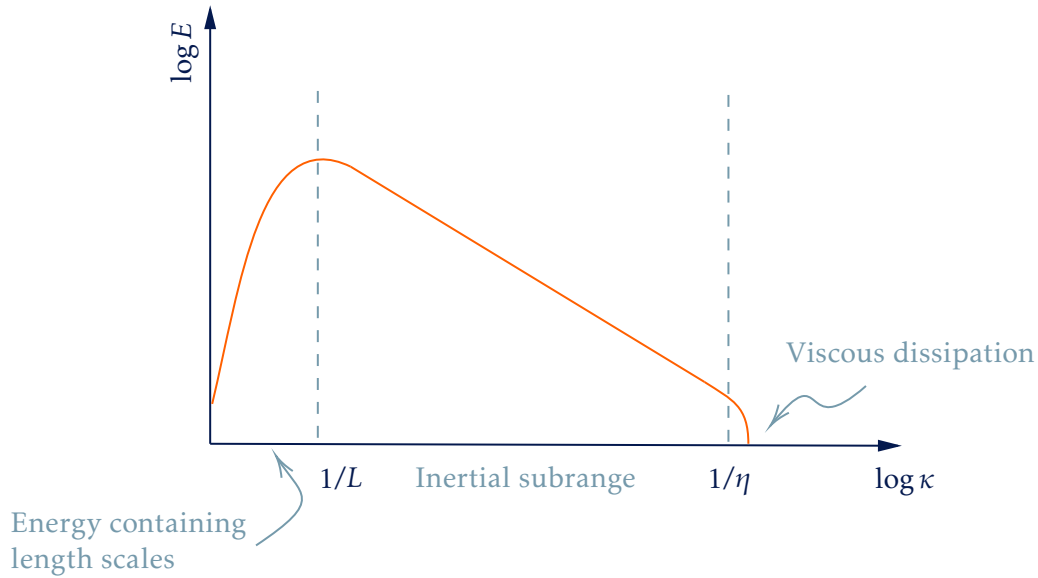
Figure 2.1: Schematics of the Kolmogorov energy cascade. It represents the energy decay from the macroscopic length scale ($1/L$) towards the Kolmogorov length scale ($1/\eta$) where it is dissipated by viscosity. The slope of the line is $-5/3$ (not to scale.) Similar graphs containing experimental data can be found in an extensive number of fluid dynamics books (e.g. [16, 20, 52].)

where r is the eddy size.

Taylor's hypothesis, introduced by Taylor [65] in 1938, derives from this law. As detailed in [20], in order to measure $E(\kappa)$, two probes that have variable separation are needed. In practice, a single probe is used and only the frequency spectrum $E(\omega)$ of vortices convected past the probes is measured. Considering an eddy of size r convected by a velocity U_c passing the probe with a time $t = O(r/U_c)$, we know from the 2/3-law that the energy spectrum is of the shape $(U_c t)^{2/3}$. Further using a Fourier transform, it comes

$$E(\omega) \sim (\omega/U_c)^{-5/3}. \tag{2.17}$$

The Taylor's hypothesis consists then to equate κ to ω/U_c which permits to convert from temporal to spatial spectra by the mean of a convection velocity. It constitutes an accurate approximation as soon as the time to pass the probe is short to the eddy time-scale, which requires the turbulence intensity Tu to be low for large scales:

$$L/U_c \ll T \qquad \Rightarrow \qquad \sqrt{k}/U_c \ll 1. \tag{2.18}$$

The inequality demonstrate how scale analysis can be used to determine the necessary instruments for measuring turbulent flows, specifically with regards to the Taylor hypothesis. In other words, the Taylor hypothesis assumes that turbulent fluctuations can be represented by a time-delayed shift of the mean flow.

2.4 Boundary layer

In 1904, L. Prandtl [46] introduced the boundary layer as the thin layer close to the wall in which the velocity transitions from zero values at the wall to finite values close to the wall as shown in Figure 2.2. To satisfy the no-slip condition, the velocity has to vanish at the wall

($y = 0$). Hence, a velocity gradient develops in the y direction, forming the BL, which grows with x according to different trends depending on whether the flow is laminar or turbulent. It
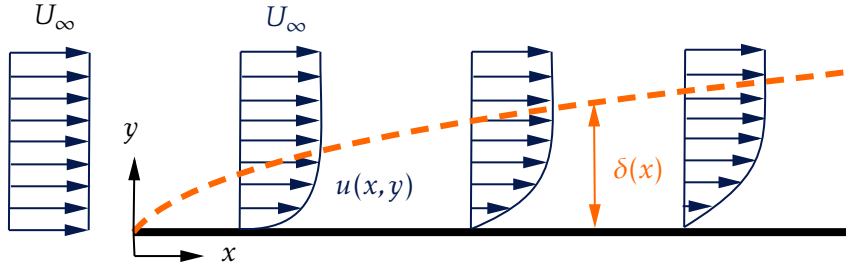
Figure 2.2: Boundary layer developing on a flat plate at zero incidence, reproduced from [60].

has to be noted that, in the case of the flat plate, the free stream velocity U_∞ is used. This is generalized for more complex geometries by the local free stream velocity $U_e(x)$.

Four quantities are usually used to describe the BL state as detailed by Schlichting and Gersten [60]:

1. the BL thickness $\delta(x)$, that is schematically shown in Figure 2.2,

2. the wall shear stress τ_w defined in Equation (2.9) or the skin friction coefficient c_f defined in equation (2.10),

3. the displacement thickness δ^*, measuring how much the streamlines are displaced due to the BL:

$$\delta^*(x) = \int_0^\infty \left(1 - \frac{\rho}{\rho_e}\frac{u}{U_e}\right)\mathrm{d}y, \tag{2.19}$$

4. the momentum thickness θ, that can be interpreted as a measure the drag:

$$\theta(x) = \int_0^\infty \frac{\rho}{\rho_e}\frac{u}{U_e}\left(1 - \frac{u}{U_e}\right)\mathrm{d}y, \tag{2.20}$$

and / or the shape factor $H = \delta^*/\theta$, a non-dimensional parameter that can be seen as a measure of the stability of the BL to separation. It is greater than 2 for laminar BL and lower than 2, usually close to 1.4, for turbulent BL.

Note that the density profiles are used to take compressibility effects into account.

Boundary layer state is often resolved with the von Karman momentum integral equation, introduced in [75] associated with a method prediction the velocity profile (e.g. Pohlhausen's method, see [53]) or other concepts as the Falker-skan method (see [8]). There are intrinsic differences between laminar and turbulent boundary layers: turbulent BL are thicker and grow faster than laminar ones but are less prone to separation thanks to their more important mixing. However this mixing is behind greater shear stress such that friction loss are more important as well. This leads to higher thicknesses but lower shape factors for turbulent BL.

Boundary layer analysis is done by introducing the undimensional wall units:

$$n+ = \frac{n u_*}{\nu}, \; s+ = \frac{s u_*}{\nu},$$
$$U+ = \frac{\overline{U}}{u_*}, \tag{2.21}$$

where n is the normal distance from the wall, s the tangential distance along the surface, ν is the kinematic viscosity and u_* is the friction velocity given by

$$u_* = \sqrt{\frac{\tau}{\rho}}, \tag{2.22}$$

with τ the wall shear stress and ρ the density. The boundary layer developing on the surface can be divided in different regions as follows and as shown in Figure 2.3a (see [60]).

1. The inner layer, where wall units are relevant but outer dimensions are not relevant and the eddies scale with the distance to the wall. This layer is divided in three sublayers of which the velocity profiles are shown in Figure 2.3b:

   (a) the viscous sublayer, where the flow is laminar, dominated by viscosity (no Reynolds stress),
   (b) the buffer layer, that is a transition layer where the production of turbulent kinetic energy is maximum,
   (c) the log layer belonging both to inner and overlapping region, where the viscosity nor the outer scales are relevant.

2. The outer layer, where viscosity is not relevant (no laminar stress) and the gradients are of the order of the macroscopic length scale.

3. The overlap region where viscosity nor outer scales aren't relevant.
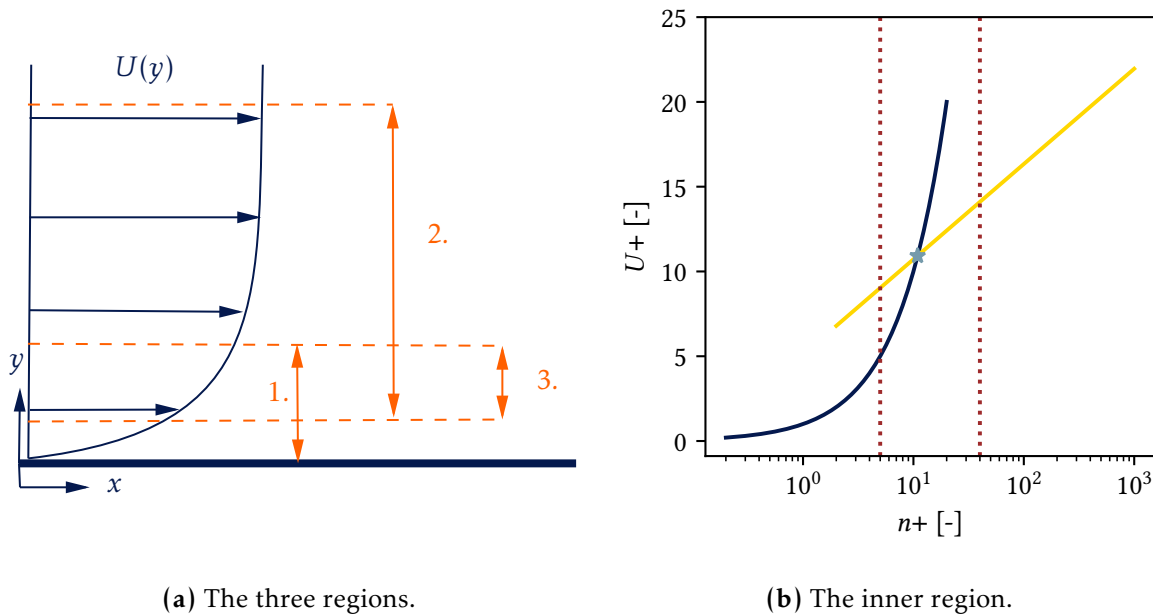
(a) The three regions.

(b) The inner region.

Figure 2.3: Schematic view of boundary layer regions and sublayers, adapted from [68].

In Figure 2.3a, the boundary inner (1.), outer (2.) and overlap (3.) regions are illustrated. In Figure 2.3b, the velocity profile in the sublayers is drawn. The blue line represents the curve $U+ = n+$, corresponding to the viscous sublayer ranging from $n+ = 0$ to ~ 5. The yellow line represents the curve $n+ = 2.44 \cdot \log(n+) + 5.1$, corresponding to the log layer ranging from $n+ =\sim 40$ to ~ 1000. The region ranging from $n+ \approx 5$ to ~ 40 corresponds to the buffer layer, a gray zone where the turbulent mixing is maximum. The velocity profile in this layer is interpolated from the two embracing layers (see [16, 20, 52, 68]).

2.4.1   Boundary layer separation

In presence of adverse pressure gradient, BL might detach from the surface. This phenomenon is called BL separation and can be detected by the value of the wall shear stress τ_w, or equivalently the skin friction coefficient c_f, that is zero at the wall. In other words, this is the point where the velocity gradient perpendicular to the wall is zero at the wall:

$$\tau_w = 0. \tag{2.23}$$

After that point, the flow is reversed and the wall shear stress is negative. This is an important condition which will be used later in this thesis. It is illustrated in Figure 2.4 where the recirculating zone is separated from the outer flow by the dividing streamline originating from the point S.
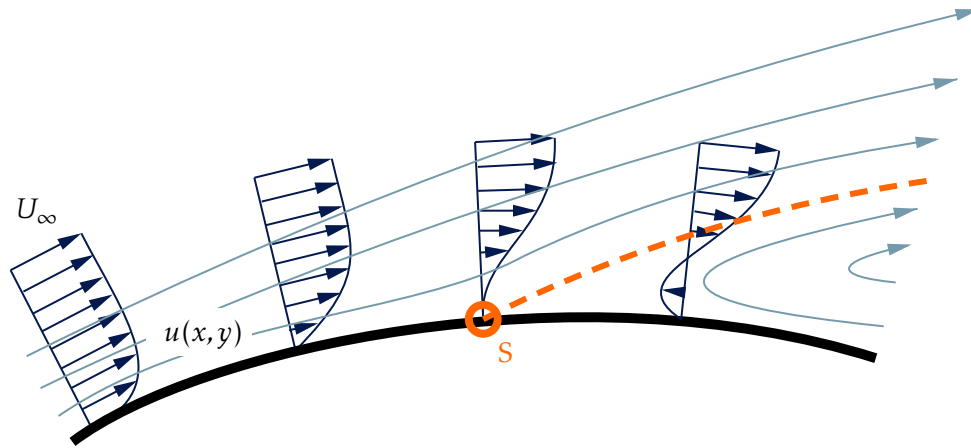
Figure 2.4: Boundary layer separation on a curved surface. The separation location is distinguished by the S point.

2.4.2   Transition in the boundary layer

Transition in boundary layer is impacted by different parameters as the Reynolds number, the pressure gradient, the surface roughness and the turbulence intensity. Mechanisms that induce transition from laminar to turbulent flow are axisymmetric waves. They initiate the transition to turbulent flow via three-dimensional structures formation and are called the Tollmien-Schlichting (TS) waves (e.g. see [54, 60, 61, 80]). Figure 2.5 shows the typical experimental shape of transition for the flat plate[2]. In 1, the flow is stable and laminar. In 2, the momentum thickness Reynolds number ($\mathrm{Re}_\theta = U\theta/\nu$) reaches a critical value and instabilities develop in the laminar BL: the unstable Tollmien-Schlichting waves appear and induce three-dimensional waves and vortex formation in 3. In 4, there is a vortex decay which leads to spots formation in 5 and fully turbulent flow in 6.

   Transition in BL can be studied by stability theory, i.e. consider the laminar flow as basic flow motions superimposed with a perturbation motion that is small compared to the mean flow. These perturbations are represented by modes, where each mode is associated with a wave propagating in the x direction. This idea leads to Orr-Sommerfeld equation (see [3, 60, 78, 79]), which in turn allows to see the stability analysis of laminar flows as an eigenvalue problem, fully developed in [60].

---

[2]This figure schematizes turbulent spots by simple circular dots. Note however that the shape of these spots is well known and detailed in a large extent of studies as in [47].
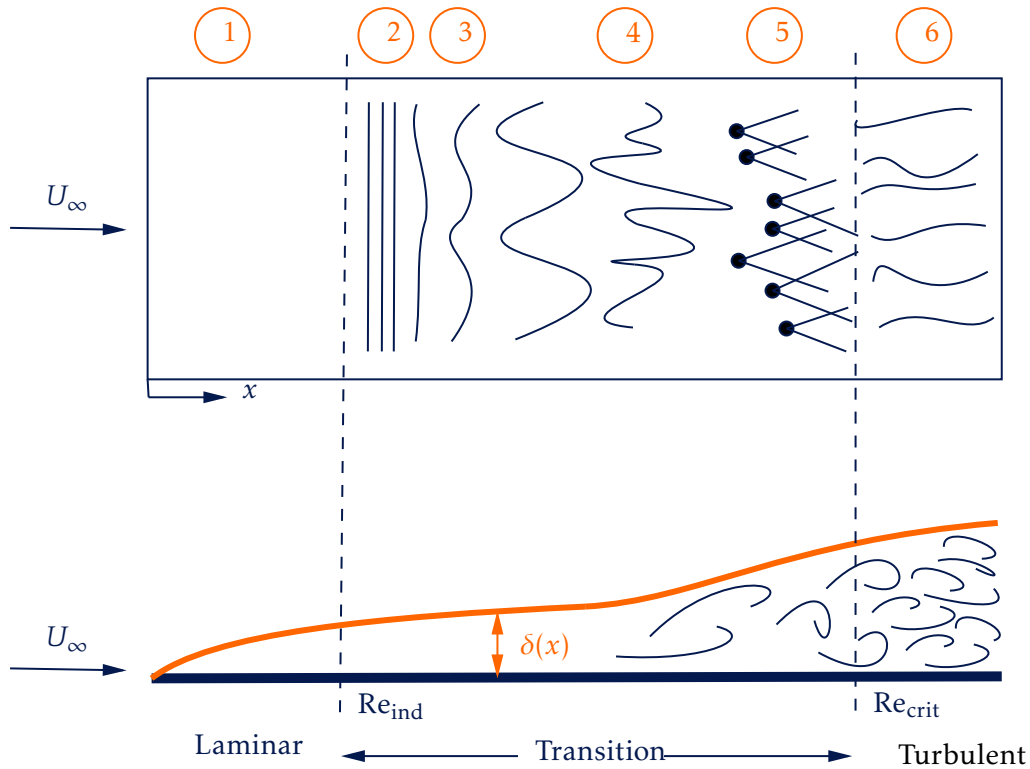
Figure 2.5: Schematic view of the transition in a flat plate boundary layer, reproduced from [60].

Transition can be triggered by different modes at different locations. There exist three transition modes:

- Natural transition (described above),

- Bypass transition,

- Separated flow transition,

- Reverse transition and,

- Wake induced transition (may induce natural transition).

Bypass transition derives its name from the fact that the three first steps of natural transitions are bypassed and turbulent spots are directly formed within the BL. This is the case of high free-stream turbulence levels or incoming wakes flows. Linear stability theory is then irrelevant and if the pressure gradient is favorable, no TS waves are formed.

In separated-flow transition, the laminar BL separates and transition occurs in the free-shear-layer, forming a separation bubble, as detailed in the next section. In LPT, it may occur in an "overspeed" region.

2.4.3   Separation bubbles

One talks of separation bubble when the BL separates because of the adverse pressure gradient then further reattaches to the surface. The typical shape of a separation bubble is shown in Figure 2.6. The recirculation zone can be seen below the dividing streamline. The difference

with Figure 2.4 is the reattachment point R. Note that the streamlines beyond the reattachment point shouldn't be smooth since the flow is, in general, turbulent in this region[3].
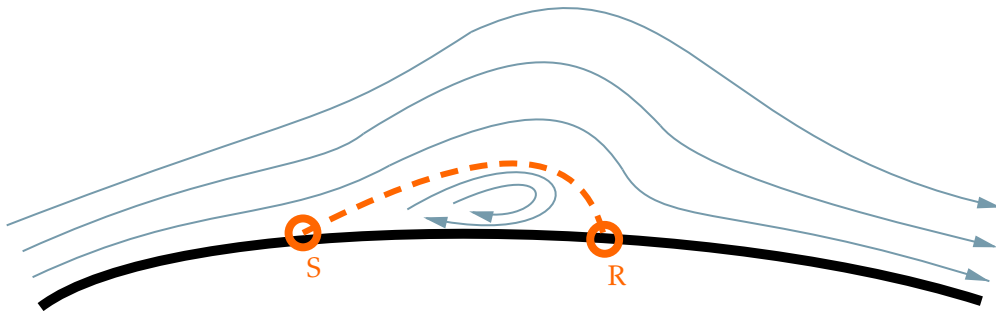
Figure 2.6: Streamlines of the flow along a surface experiencing a separation bubble. The point S denotes the separation location while the point R denotes the reattachment location.

2.4.4 Shock boundary layer interactions

In this work, the flows are transonic, i.e. the values of the Mach number are comprised between 0.7 and 1.2. The free-stream and outlet Mach numbers vary between 0.7 and 0.9. Supersonic flows appear because of local acceleration regions of the flow, especially over the SS and are terminated by weak or strong shocks.

As it has been shown in [6, 35] and will be shown in the continuation of this study, vortices detaching from the trailing edge cause acoustic perturbations. These perturbations are able to go upstream unless the flow is supersonic, in which case the perturbations are "blocked" at the throat of the passage forming a normal shock in the flow.
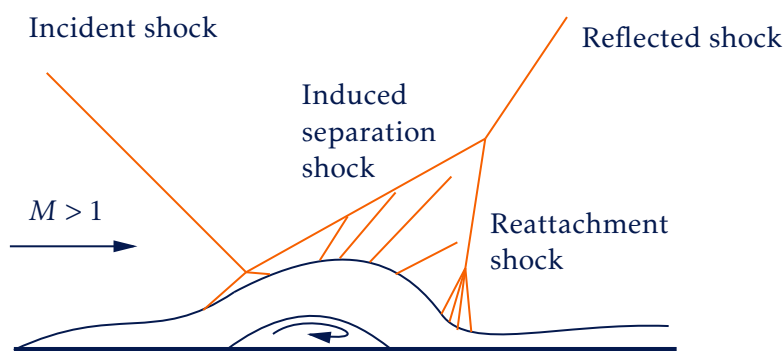
Figure 2.7: Shock boundary layer interactions, reproduced from [66].

Interactions between shock and BL lead to complex physics. Consider an incoming shock that interacts with a BL (Figure 2.7) which is reflected on it. Accross the shock, an important increase in pressure happens such that the pressure downstream the shock is higher than upstream. This increase in pressure strengthen the adverse pressure gradient (if present, e.g. on the SS) and separation can occur. Because of the displacement of the BL which creates an obstacle to the flow, an induced separation shock is formed. The flow being isentropically accelerated on the top of the separation bubble, an expansion fan forms and is terminated with

---

[3]Inverse transition can sometimes occur, but this is very rare.

a reattachment shock. Actually the reflected shock is created by the merging both of the reattachment and the induced shock.

An important thing to note is the location of the separation point: it is a bit more upstream than the incident shock. This is due to the fact that, within the BL, there is a lower velocity so that the region is subsonic. Through this subsonic region, the strong increase in pressure is felt more upstream.

2.5   Wake and von Karman vortex street

Wakes are a special type of free shear flows in the sense that they don't have boundaries. They are of particular interest because of the momentum deficit advected within the flow. Moreover, some of the mean flow is entrained in the wake at its boundaries. It is an important region where Reynolds stresses and TKE are large such that they play a major role in losses. This section details the main characteristics of wakes.

2.5.1   Wake

The typical shape of a planar wake is shown in Figure 2.8. In a wake, the mean flow is such that the crosswise velocity is negligible in front of the streamwise velocity, i.e. $\overline{u} \gg \overline{v}$ and the streamwise gradients are negligible in front of the crosswise gradients, i.e. $\partial/\partial x \ll \partial/\partial y$. As the flow suddenly enters a region of irrotational flow, a highly convoluted interface develops (like in BL) between the wake and the outflow region.
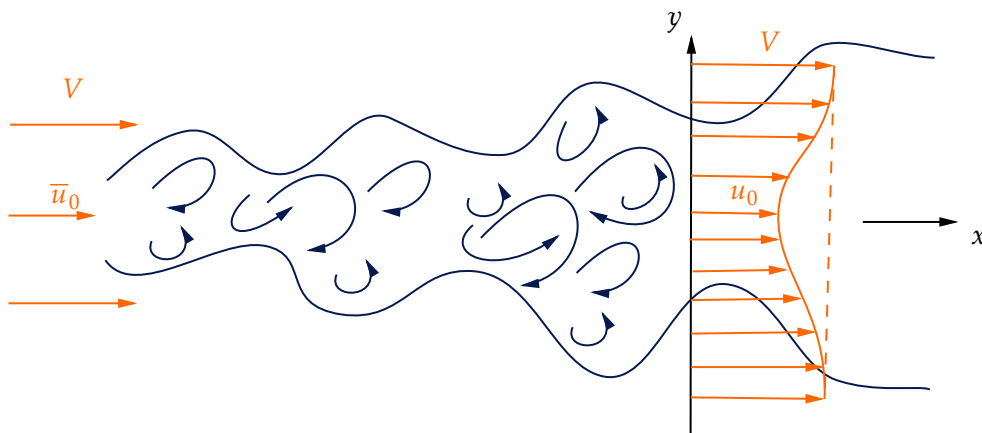
Figure 2.8: Planar wake, reproduced from [16].

Three asumptions can be done when studying a wake:

1. axial gradients of Reynolds stresses are neglected in front of transverse gradients,

2. laminar stresses are neglected and,

3. the transverse component of the mean inertia is neglected.

Using these assumptions and introducing them in the Reynolds averaged NSE leads to

$$\frac{\partial}{\partial x}[\rho\overline{u}(U-\overline{u})] + \frac{\partial}{\partial y}[\rho\overline{v}(U-\overline{u})] = -\frac{\partial\tau_{xy}^R}{\partial y}. \tag{2.24}$$

Integrating this equation shows that the momentum deficit D is constant:

$$D = \int_{-\infty}^{\infty} \rho \overline{u}(U - \overline{u}) \mathrm{d}y. \tag{2.25}$$

Even so, the mass flux is not conserved due to entrainement. The planar wake spreads as $\delta \sim x^{1/2}$ and $\overline{u}_0 \sim x^{-1/2}$. Moreover, the velocity profile is self-similar, i.e.

$$\frac{U - \overline{u}}{\overline{u}_0} = f(y/\delta). \tag{2.26}$$

The streamwise vortices are major contributors to the entrainment and are often called "entrainment eddies", as developed in [20]. They contain large amounts of energy (TKE) and thus Reynolds stresses, which in turn makes them very noisy. Besides this and the fact that they are entraining the outer flow into the wake due to engulfement, it is interesting to study the large scales structures because their flow pattern can be controlled (e.g. chevrons nozzles.)

2.5.2   Vortex street

Consider a two-dimensional blunt body, e.g. an airfoil or a cylinder, immersed in a flow. For low Reynolds number, the vorticity is generated close to the surface because of the no-slip condition. When Re is increased, because of advection the vorticity is progressively squeezed behind the body, forming a stationnary region of recirculation. As detailed in [37] , for a certain Reynolds number, the wake behind the body becomes unstable: oscillation develops in which the velocity is periodic in time and space, this is the von Karman vortex street. Initially studied for the flow past a circular cylinder, it consists in two rows of vortices with opposite sens of rotation and with an amplitude growing downstream. An illustration of the formation of von Karman street for the flow past a turbine blade is shown in Figure 2.9.
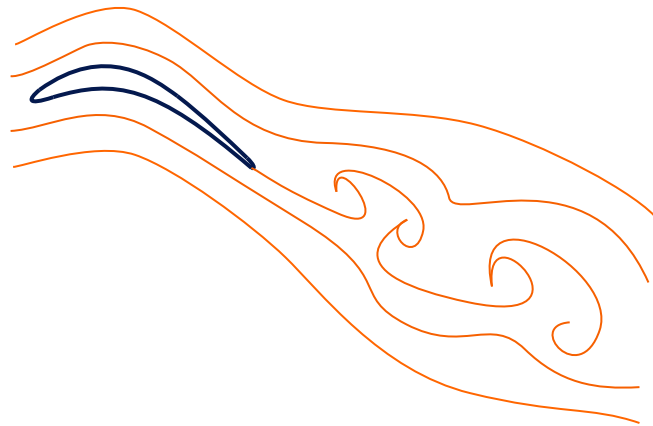
Figure 2.9: Schematic view of the formation of the von Karman vortex street for the flow past an LPT blade.

It was concluded that the rows of vortices are unstable if they are non-staggered or if the ratio of the lateral distance between vortices to their longitudinal distance is 0.28 (e.g. detailed in [37]). It is important to note that the velocity of the vortices moving downstream is slower than the free-stream velocity. For the flow past a cylinder, the vortex shedding takes place for Reynolds number between 80 and 200. Above a certain Reynolds number, the vortex street becomes unstable and the flow becomes irregular and chaotic. Commonly, the shedding frequency is close to the natural frequency of structural modes of vibration of the body. This

is the reason why cylindrical structures are often designed to avoid coherent shedding. The above-mentionned frequency f is often expressed by the Strouhal number:

$$\text{St} = \frac{fL}{U}, \tag{2.27}$$

where L is a characteristic length (e.g. diameter for cylinder) and U is a characteristic velocity. The Strouhal number related to vortex shedding may also be computed by the Roshko empirical correlation for cylinders:

$$\text{St} = \frac{\text{Ro}}{\text{Re}} = \frac{0.212 \cdot \text{Re} - 2.7}{\text{Re}} = 0.212 \cdot \left(1 - \frac{12.7}{\text{Re}}\right), \tag{2.28}$$

where Ro is the Roshko number and Re is the isentropic Reynolds number (see [81]).

2.6 Statistical tools

The inherent characteristics of turbulent flows suggest that any theory of turbulent flows must be statistical. Single realizations of such flows are random, chaotic and different at each repetition. However, statistics are reproducible and predictable. For these reasons, this section highlights the main statistical tools that are used to study turbulent flows.

2.6.1 Averages

Consider a flow which is defined in all points of its definition domain in the three-dimensional space and at any time t by its velocity field $\mathbf{u}(\mathbf{x}, t)$. The true mean of the velocity is given by

$$\langle \mathbf{u}(\mathbf{x}, t) \rangle = \int_{-\infty}^{\infty} \tilde{\mathbf{u}} \cdot \text{pdf}(\tilde{\mathbf{u}}; \mathbf{x}, t) \mathrm{d}\tilde{\mathbf{u}}, \tag{2.29}$$

where pdf is the probability density function. In practice, this mean is approximated by estimates. An average can by a time (if statistically stationnary over the period T), an ensemble (if repeatable over a sample of size N) or a spatial (if homogeneous in the space of size L^3) average, respectively:

$$\langle \mathbf{u}(\mathbf{x}) \rangle_T = \frac{1}{T} \int_t^{t+T} \mathbf{u}(\mathbf{x}, t') \mathrm{d}t',$$

$$\langle \mathbf{u}(\mathbf{x}, t) \rangle_N = \frac{1}{N} \sum_{k=1}^{N} \mathbf{u}^{(k)}(\mathbf{x}, t), \tag{2.30}$$

$$\langle \mathbf{u}(t) \rangle_L = \frac{1}{L^3} \int_{\mathbf{x}}^{\mathbf{x}+\mathbf{L}} \mathbf{u}(\mathbf{x}', t) \mathrm{d}\mathbf{x}'.$$

These estimates converge to the mean when T, N or L tend to infinity.

2.6.2 Correlations

Correlation between two variables directly refers to the connection between these two variables, and is opposite to independence. Consider a flow around a cylinder. The velocity fluctuations u' will be similar but maybe out of phase for two points that are close to each other, meaning they are correlated. The same variable will be very different for two points that are far from each other, meaning that they are uncorrelated. This concept permits to measure the turbulent state of the flow with the velocity correlation tensor (two-point correlation):

$$Q_{ij}(\mathbf{x}, \mathbf{r}, t) = \langle u_i'(\mathbf{x}, t) u_j'(\mathbf{x} + \mathbf{r}, t) \rangle. \tag{2.31}$$

2.6.3   Probability distribution functions

Consider a randow variable X. Its probability density function is defined such that:

$$P(a < X \leq b) = \int_a^b \mathrm{pdf}(x)\mathrm{d}x,$$
$$\mathrm{pdf}(x) \geq 0, \tag{2.32}$$
$$\int_{-\infty}^{\infty} \mathrm{pdf}(x)\mathrm{d}x = 1.$$

Its mean is defined as

$$\mu = \int_{-\infty}^{\infty} x\,\mathrm{pdf}(x)\mathrm{d}x. \tag{2.33}$$

The variance of X, which represents the deviation from mean, is

$$\sigma^2 = \int_{-\infty}^{\infty} (x - \mu)^2 \mathrm{pdf}(x)\mathrm{d}x. \tag{2.34}$$

The skewness factor, which represents the asymmetry of pdf, taking $\mu = 0$, is

$$\mathrm{skew}(X) = \frac{1}{\sigma^3} \int_{-\infty}^{\infty} (x - \mu)^3 \mathrm{pdf}(x)\mathrm{d}x. \tag{2.35}$$

The flatness factor or kurtosis represents the weight of pdf tail or intermittency:

$$\mathrm{kurt}(X) = \frac{1}{\sigma^4} \int_{-\infty}^{\infty} (x - \mu)^4 \mathrm{pdf}(x)\mathrm{d}x. \tag{2.36}$$

For a Gaussian distribution, $\mathrm{kurt}(X) = 3.0$ and $\mathrm{flat}(X) = 0$. Large values of $\mathrm{kurt}(X)$ indicate intermittent signal.

2.7   Literature review

As introduced above, LPT have been studied for several decades. With a view to provide a first glance at the behavior of the performance parameters and more generally to familiarize with the different concepts, a literature review is provided in this section.

2.7.1   Transition and separation bubbles in low pressure turbines

The flow in turbomachines is turbulent in the majority of components. However, flow over surfaces, e.g. over blades, can be laminar, transitional or turbulent.

In order to study transition in LPT, where pressure gradients are important, a common method is to use the momentum thickness Reynolds number Re_θ to account for turbulent mixing and the acceleration parameter K to account for pressure gradients effects. The latter is defined as

$$K = \frac{\nu}{U_{\mathrm{is}}^2} \frac{\mathrm{d}U_{\mathrm{is}}}{\mathrm{d}s}, \tag{2.37}$$

where U_{is} is the local isentropic velocity outside the BL. Basically, K is positive for favorable pressure gradients, negative for adverse pressure gradients and zero for zero pressure gradient (ZPG). These two parameters are used in the overwhelming majority of studies on the subject. Mayle reviewed the state of the art in laminar-turbulent transition in gas turbine engines in

[47]. Figure 2.10 as well as the following development are drawn from this paper. The figure shows the different possible modes of transition with respect to Re_θ and K. The stability criteria marks the limit above which TS waves appear in the BL. The separation criteria was introduced by Thwaites [69] and is defined as

$$\text{Re}_{\theta,S} K_S = -0.082. \tag{2.38}$$

It is clear that separation is very likely to appear for large adverse pressure gradient which is
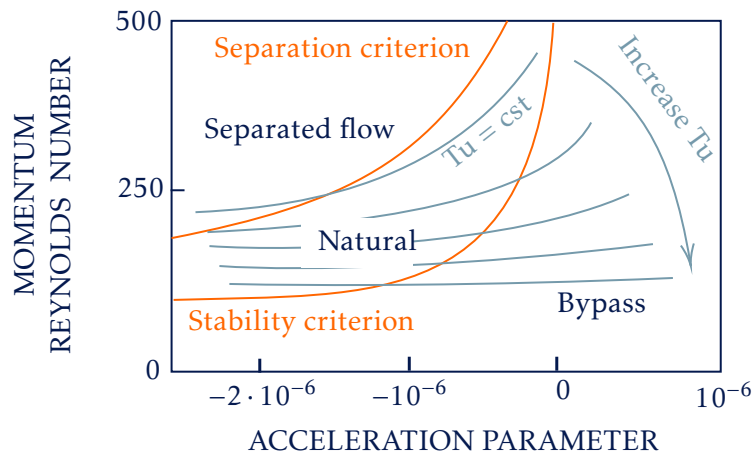
Figure 2.10: Modes of transition with respect to the Reynolds number and the acceleration parameter, reproduced from [47].

the case on SS of LPT. Actually, the flow over the SS of LPT is generally laminar to transitional before it separates. Hence, depending on transition and separation locations, the transition can be either natural (for low Tu), bypass (for high Tu) or separated (if separation occurs early). Moreover, it is important to note that transition is an unsteady three-dimensional phenomenon affected by periodic mechanisms, such as passing wakes. In the transonic regime, trailing edge shocks may also induce transition, bypassing the first steps of natural transition. It should additionally be said that according to this graph, transition in favorable pressure gradients (e.g. PS of LPT) essentially consists of bypass mode. In some particular cases ($K > 3 \cdot 10^{-6}$), reverse transition, also called relaminerization, can be triggered. For such cases, transition cannot occur.

In a more general way, it can be stated that, at low inlet Tu, transition in separated flows is controlled by the momentum thickness Reynolds number and the acceleration parameter at separation, respectively $\text{Re}_{\theta,S}$ and K_S.

As free-stream turbulence increases and at ZPG, it has the effect of boosting the production of turbulent spots. Parallely, the momentum thickness Reynolds number at which transition starts is reduced. At low free-stream turbulence, other phenomena have to be taken into account as the effect of Tu becomes negligible. Indeed, while at high Tu transition takes place in bypass mode without TS waves, at low free-stream turbulence transition is more affected by acoustic disturbances rather than Tu. It has to be noted that this thesis focus on the case with no free-stream turbulence such that transition is mainly affected by these acoustic pre-turbations. On the other hand, turbulence has more effect for favorable pressure gradient than for adverse ones. As the turbulence level decreases and the acceleration parameter increases, the momentum thickness Reynolds number at the onset of transition, defined as the location where intermittency factor becomes greater than 0, $\text{Re}_{\theta,t}$ increases. Hence, for low free-stream turbulence, the effect of acceleration is significant.

A mode of transition that is of prime importance here is the separated-flow transition. As detailed in [34], separated-flow transition through separation bubbles may be used to boost LPT efficiency. Mayle [47] distiguishes two types of separation bubbles: short and long bubbles. The difference between these two is their effect on the pressure distribution. While short bubbles have a local small displacement effect, long bubbles have a strong effect on the pressure distribution. Among other parameters, Reynolds number is significant to the bubble modes and may cause bubble bursting, i.e. change from short to long bubble. Bursting dramatically increases losses as shown in Figure 2.11. As detailed in [45], at high Reynolds number (a), the flow transition is triggered far upstream. Despite this transition, turbulent separation occurs and the losses increase dramatically because profile, shear layer (2) and friction losses due to the high turbulent mixing (3) add to each other. If the Reynolds number is decreased, turbulent separation vanish (b) and the transition point moves downstream. This allows to laminar separation to take place. It is in this region that the separation bubble forms, thanks to the transition of the flow that occurs after the separation but soon enough to permit reattachment. The losses are then dominated by wall shear layers and wake beyond TE. Further decreasing the Reynolds number, transition occurs to late for the BL to reattach. A drastic increase in losses occurs (d), produced by the mixing out of separation in the wake (2). In this region, the losses firstly grow quite fast because the transition is moving downstream. A maximum is reached when the transition is at the TE. Then, the losses are increasing mostly because of the growing free shear layer thickness with decreasing Reynolds number (bubble bursting.)

Figure 2.11: Loss coefficient with respect to Reynolds number, reproduced from [34].

Figure 2.12 illustrates the pressure distribution around a separation bubble. This curve represents time and space average as the flow is unsteady and three-dimensional. It is typically encountered on SS of LPT where the flow undergoes laminar separation then reattaches later thanks to transition. The upstream region is characterized by a practically constant pressure distribution while the downstream region experiences a pressure recovery. The former consists in an unstable shear flow with turbulent produced at x_t.

Mayle's review then introduces two complementary parameters to the study of separated-transition: the Reynolds numbers based on the condition at separation and based on the distance $(x_T - x_S)$ and on the distance $(x_t - x_S)$. The presented results are based on different measurements performed by Gault [23], Gaster [22], Roberts [58] and Bellows [5]. Results are not detailed in this document since a very good explanation is already provided in [47]. However the interesting drawn conclusions are presented hereafter. It is shown that the key parameter
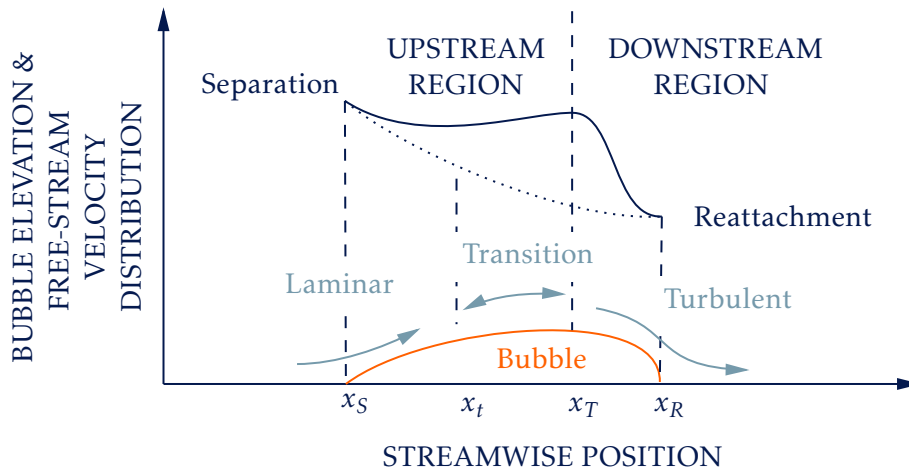
Figure 2.12: Pressure distribution around a separation bubble, reproduced from [47].

is not the length of transition, but the length of the instabe laminar shear layer. Once transition is triggered, the effect of turbulence is (surprisingly) not significant because it is blurred by instabilities of the velocity profile: the transition depends only on the separation Reynolds number. This suggests that there are more than one mode of separated-flow transition.

Hatman and Wang [24] proposed a prediction model for separated flow transition, mainly based on low free-stream turbulence level and flat plate measurements, where three separated-transition modes are distinguished (see Figure 2.13): transitional, laminar short bubble and laminar long bubble modes. The former is characterized by a natural transition starting upstream of the separation location. It happens when the flow separates at high Reynolds numbers and low adverse pressure gradient. In the second one, the onset of transition is induced downstream of separation by inflexional instability. It occurs at low Reynolds numbers and moderate adverse pressure gradients. In the last one, the onset of transition is induced downstream of separation as well, however the transition completion is delayed. It takes place at low Reynolds numbers and strong adverse pressure gradients. They are the result of KH superposed with TS instabilities where the predominance on one type to another dictates the transition mode. It has been shown in this model that the location of the maximum bubble displacement is the controlling parameter for the separated flow behavior while experimental data are better correlated with the distance Reynolds number Re_S rather than with the momentum thickness Reynolds number Re_θ. The paper results in a procedure for predicting separated-flow transition and a criteria for separated-flow transition summarized in Table 2.1.

2.7.2   Loss in low pressure turbines

Loss are defined as entropy generation mostly coming from viscous effect in boundary layers and mixing process, shock waves and heat tansfer. Loss coefficients may be defined in a lot of different ways. The energy and pressure loss coefficients have been defined in Equation (2.11). These are very satisfactory and useful for design but may be ambiguous when dealing with rotating blade rows. Thus, Denton [17] states that the only precise way to define them is entropy creation, which does not depend on whether the frame is rotating or not. However, it has to be noted that this thesis focus on a linear low pressure turbine cascade (see Chapters 3 and 4). Stationnary and adiabatic behavior implies that stagnation (total) temperature is constant such
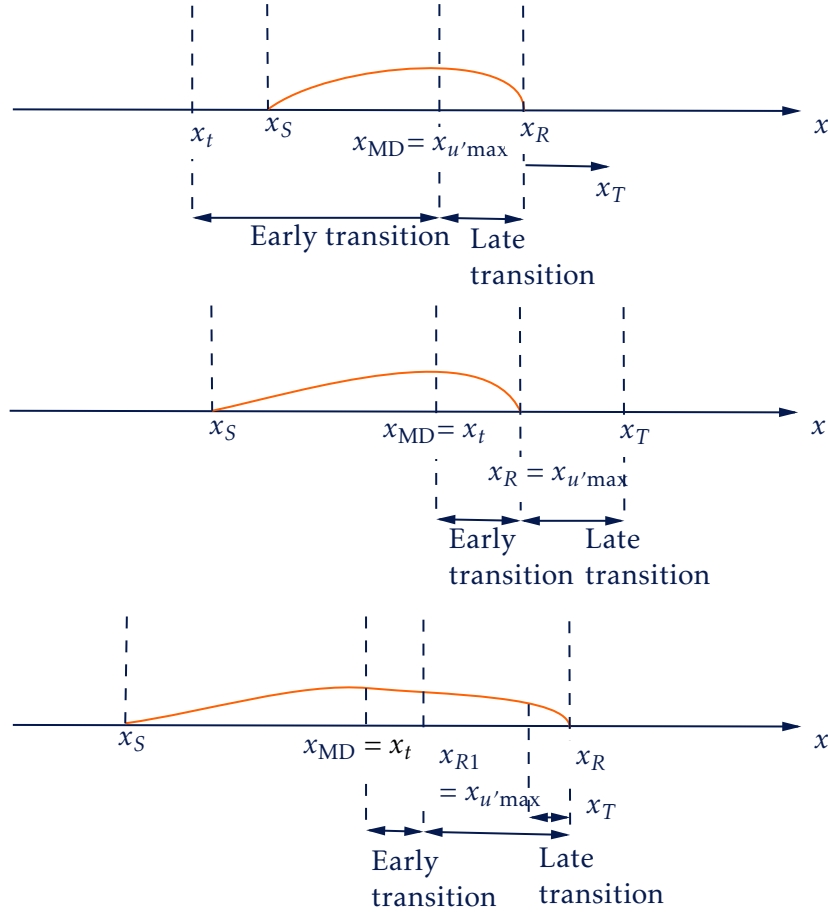
Figure 2.13: Time-average representations of transitional separation mode (top), laminar short bubble mode (center) and laminar long bubble mode (bottom) as presented by Hatman and Wang [24].

Table 2.1 Criteria for separated-flow transition, reproduced from [24].

Laminar separation, $\text{Re}_\theta < 320$			Transitional separation, $\text{Re}_\theta > 320$
Laminar separation long bubble	Intermediate stages		Transitional separation mode
$K_S < -1.3 \cdot 10^{-6}$, $\text{Re}_{x,S} < 2.05 \cdot 10^5$, $\text{Re}_{\delta^*,t}/\text{Re}_{\delta^*,S} > 2$ $\text{Re}_{x,S} < \text{Re}_{x,t}$, $\text{Re}_{x,t} = \text{Re}_{x,\text{MD}}$, $\text{Re}_\theta < 240$	$-1.3 \cdot 10^{-6} < K_S < -0.3 \cdot 10^{-6}$, $2.05 \cdot 10^5 < \text{Re}_{x,S} < 4.5 \cdot 10^5$, $\text{Re}_{\delta^*,t}/\text{Re}_{\delta^*,S} = O(1)$		$K_S > -0.3 \cdot 10^{-6}$, $\text{Re}_{x,S} > 4.5 \cdot 10^5$, $\text{Re}_{\delta^*,t}/\text{Re}_{\delta^*,S} < 1$ $\text{Re}_{x,S} > \text{Re}_{x,t}$, $\text{Re}_\theta > 320$
	Laminar separation short bubble mode, $\text{Re}_{x,S} < \text{Re}_{x,t}$, $\text{Re}_{x,t} = \text{Re}_{x,\text{MD}}$, $240 < \text{Re}_\theta < 320$	Laminar separation dominant transitional mode, $\text{Re}_{x,S} < \text{Re}_{x,t}$, $\text{Re}_{x,t} < \text{Re}_{x,\text{MD}}$, $\text{Re}_\theta > 320$	

that entropy changes depend only on stagnation (total) pressure:

$$s - s_{\text{ref}} = c_p \ln\left(\frac{T}{T_{\text{ref}}}\right) - R \ln\left(\frac{p}{p_{\text{ref}}}\right) = -R \ln\left(\frac{p_{02}}{p_{01}}\right) \approx -R \frac{\Delta p_0}{p_{01}}, \quad (2.39)$$

where c_p is the heat capacity at constant pressure. This implication suggests that, in the scope of this thesis, loss of stagnation pressure well represent changes in entropy. Note that although the latter equation gives a good quantification of the entropy creation, it is not necessarily true for transonic Mach number. Indeed, at such Mach numbers, energy separation occurs in the wake of the blade. It implies that the pitchwise temperature distribution is not constant.

In BL, the rate of entropy creation per unit volume can simply be interpreted as viscous shear work converted to heat. Most of this generation is concentrated near the surface, i.e. in the inner region of the layer (see Section 2.4), especially for turbulent flows where it occurs in the laminar sublayer and the logarithmic regions. In order to provide a satisfying estimation of the dissipation coefficient, the full details of BL have to be known. The dissipation coefficient is generally less dependant of the state of BL for turbulent BL than on the skin friction coefficient. Indeed, as introduced earlier, turbulent BL are characterized by a fuller velocity profile, implying lower shape factor (H) values and higher mixing, such that friction is more important than in laminar BL. It is possible to provide an estimation of the dissipation coefficient with the help of correlations depending on whether the BL is laminar or turbulent. These are addressed in [17] but not recalled in this document. In the same paper, the effect of Mach number on skin friction is said negligible. One of the concentration point of this thesis is the separation and transition in BL. However loss in BL are not addressed.

The second major contributor in entropy creation are mixing processes that can occur whenever shear acts in the flow, e.g. at the interface between separated BL and mean flow or in the wake of the blade. They are generally associated with turbulence with complex mechanisms such that it is often complicated to quantify local rates. As often it is however easier to perform a momentum and energy budget on a control volume from which overall entropy creation can be deduced. This method is used to compute loss in the wake behind a trailing edge, called base flow. Its computation requires the BL quantities upstream of the TE and the base pressure. The latter is expressed in terms of a base pressure coefficient, noted c_{pb}, given by

$$c_{pb} = \frac{p_b - p_{\text{ref}}}{(1/2)\rho U_{\text{ref}}^2},$$ (2.40)

where p_{ref} and U_{ref} are reference quantities in Denton's analysis and will be taken respectively as total inlet pressure and isentropic outlet velocity in this thesis. Combining this with BL contribution leads to

$$\zeta_b = \frac{\Delta p_0}{(1/2)\rho V_{\text{ref}}^2} = -\frac{c_{pb}t}{w} + \frac{2\theta}{w} + \left(\frac{\delta^* + t}{w}\right)^2,$$ (2.41)

where w may be taken equal to the throat of the passage, (noted o in this document) t equals to the TE thickness (diameter if circular, noted d_{TE} in this document). The derivation of this equation is given in [17]. It has to be noted that this equation does not take into account any unsteady process such as von Karman vortex street formation. In case of separated BL at TE, this model must be adapted because the value of displacement thickness may be larger than the trailing edge thickness. The extra loss is computed as

$$\zeta_{\text{sep}} = \left(\frac{\delta^{*2} + 2t\delta^*}{w^2}\right).$$ (2.42)

It can be seen that small separations do not cause large loss while large separations do. Finally, the effect of increasing the Mach number at TE is to increase the base coefficient.

The third important contributor to loss are shock waves that involve generally high viscous normal stresses and heat conduction. In normal shock waves, entropy creation scales as $(M^2 - 1)^3$. In oblique shock waves, for the same upstream Mach number, the loss are reduced since

only the normal component is to be taken into account. Sometimes shock can be benefical in compressors thanks to the compression work they provide. It is obviously not the case in turbines in which shocks are not desirable, but often encountered if the turbine operates at transonic velocities. The most problematic are not shocks developing in the passage, as they are usually oblique, but shock systems developing at TE because they can generate large TE loss.

2.7.3   General considerations

Table 2.2 lists different articles that investigate the flows and losses in LPT[4]. It can be seen that a large range of outlet isentropic Reynolds number has already been covered.

Table 2.2 Reference studies and their main conditions.

References	Year	Type	M	Re	f_{red} [Hz]	Tu [%]
Vera and Hods. [74]	2002	Exp.	~ 0.64	$190,000$	-	-
Vazq. et al. [71]	2006	Exp. and RANS	0.5 to 0.9	$120,000$ to $315,000$	-	4.0%
Coull et al. [13]	2010	Exp.	-	$50,000$ to $220,000$	0.314 to 0.942	3.0%
Pacciani et al. [50]	2010	Exp. and RANS	0.6 to 0.7	$80,000$ to $250,000$	Steady	0.8 to 2.6%
Michalek et al. [48]	2010	Exp.	0.65	$80,000$ to $160,000$	Steady	0.8 to 3.2%
Benyahia et al. [4]	2011	RANS and Exp.	0.6 to 0.65	$80,000$ to $250,000$	Steady to 0.68	0.8 and 1.8%
Vazq. and Torre [72]	2012	Exp.	0.61 to 0.92	$275,000$ to $280,000$	0.4	-
Dähnert et al. [15]	2013	Exp.	-	$80,000$ to $300,000$	Steady	0.5%
Michelassi [49]	2014	DNS	0.405	$60,000$ to $100,000$	Steady to 1.22	0.5 to 3.2%
Börn. and Nieh. [7]	2020	Exp.	0.2-1.05	$17,120$ to $200,389$	Steady	7.7%

Coull et al. [13] investigated velocity distributions for LPT by means of a flat plate experiment. Unsteady wakes were simulated to mimic the conditions encountered in real turbomachinery flows. The general observations consist in separation just after the velocity peak. The generation of losses is dominated by the mixing in the reattachment process, mixing in the turbulent BL and effects of wakes / BL interactions. In the same line of though than Zhang et al. [82], shifting the velocity peak, i.e. the loading, towards the TE was found to be beneficial. The introduction of wakes suppress the separation bubble but increase high loss turbulent regions. In higher Reynolds number flows it increases the loss production. In such flows, the reduced frequency should not be increased, while it should be for lower Reynolds number flows.

Pacciani et al. [50] showed through a CFD (RANS, LKE) study on T106C and T108 blades that LKE concept can be used to study transition and BL separation in LPT as long as the

---

[4]In that table, the third colomn refers to the used method, i.e. if it is experimental (exp.) or numerical (RANS, LES or DNS). The symbol f_{red} designates the reduced frequency of incoming wakes.

Reynolds number isn't too low. It suggests that RANS models are not sufficient to provide a complete description of the flow in low pressure turbines at such low Reynolds number conditions. Figure 2.14a shows the isentropic Mach number distribution over the blade SS for the T106C at $Re = 80 \cdot 10^3$, $M = 0.7$, $Tu = 0.8\%$ and $M = 0.65$ and $Tu = 2.6\%$. The curve for the T108 blade is drawn for $Re = 70 \cdot 10^3$, $M = 0.6$ and $Tu = 1\%$. The T108 is more front loaded than the T106C with a velocity peak occuring soon on the suction side. The two curves for the T106C show that altought the small difference in outlet Mach number, the inlet turbulence intensity plays an important role in the displacement effect of the bubble. The velocity peak is shifted downstream as the Mach number increases. Figure 2.14b shows the pressure defect in the wake for both T106C (only at first conditions) and the T108. Benyahia et al. [4] provided a RANS
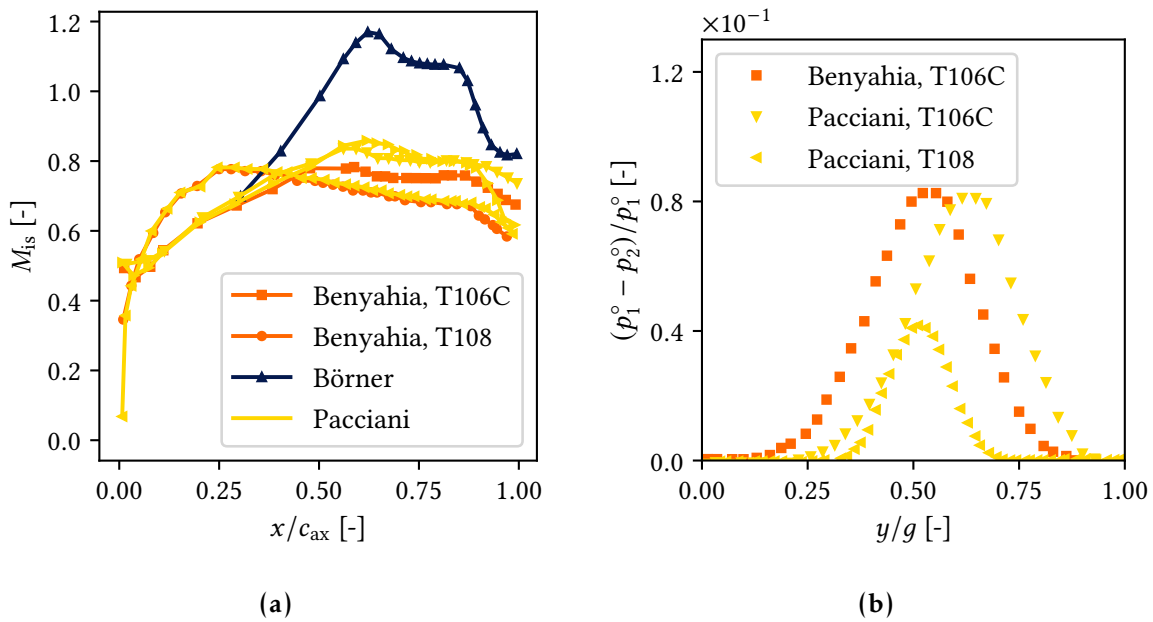
Figure 2.14: Isentropic Mach number along the suction side (a) and pressure defects in the wake at $x/c_{ax} = 1.45\%$ (b) from different references. Benyahia et al. [4] studied the T106C blade at $Re = 80 \cdot 10^3$, $M = 0.65$ and $Tu = 0.8\%$ (■) and the T108 blade at $Re = 80 \cdot 10^3$, $M = 0.6$ and $Tu = 0.8\%$ (•). Börner and Niehuis [7] considered the conditions $Re = 100 \cdot 10^3$, $M = 0.95$ and $Tu = 7.7\%$ (▲). Pacciani et al. [50] studied the T106C blade at $Re = 80 \cdot 10^3$, $M = 0.65, 0.7$ and $Tu = 0.8$ (▼), 2.6% (▶) and the T108 blade at $Re = 70 \cdot 10^3$, $M = 0.6$ and $Tu = 1\%$ (◀).

and experimental study of the T106C and T108 blades at $Re = 80,000$ with inlet turbulence between $Tu = 0.8$. The isentropic Mach number distribution over the SS and the total pressure loss in the wake of the T106C blade are shown in Figure 2.14. Their results for the T108 well match with that of Pacciani et al. [50]. Their results for the T106C added to that of Pacciani et al. [50] allow to have a wider understanding of its behavior.

The third curve of Figure 2.14a, at much higher isentropic Mach number, comes from the work of Börner and Niehuis [7]. They inverstigated the dynamics of shock interacting with other flow features as BL are seldom investigated in literature. The paper proposes such an study on a transonic LPT at high subsonic exit Mach numbers. Flow experiences a large separation bubble described by hot-films measurements. Schlieren images allow to see an unsteady normal shock on the SS which is interacting with the laminar BL. It has been shown that transition is amplified by the shock interaction. Moreover, the shock and BL pulsations are associated with low frequencies of the order of ~ 700 and 1800 Hz.

Michalek et al. [48] provided a study of the T106C with and without inlet turbulence intensity for exit Mach number of $M_{2,\text{is}} = 0.65$ and Reynolds number of $\text{Re}_{2,\text{is}} = 80,000$ to $160,000$. Figure 2.15 shows the isentropic Mach number distribution over the SS and the intermittency factor for different conditions. It can be seen that transition and reattachment are faster for higher Reynolds number. Again, typical shape of the isentropic Mach number distribution is retrieved. On the other hand, the intermittency factor shows that the BL is turbulent at TE. Mikálek et al. then correlate the characteristic points, especially separation location with

(a) Isentropic Mach number distribution.

(b) Intermittency factor.
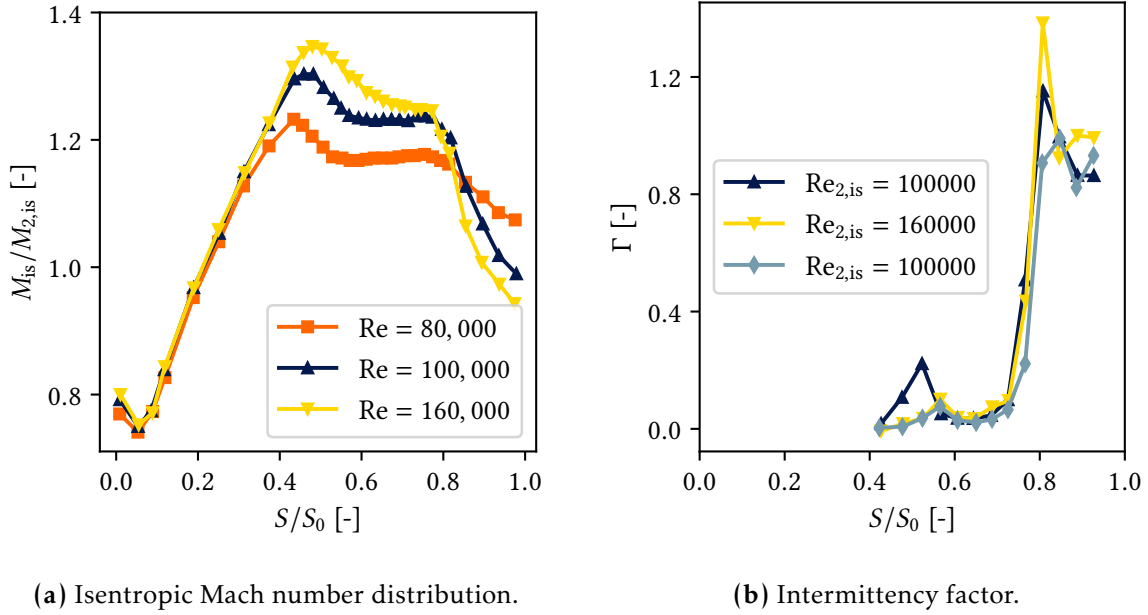
Figure 2.15: (a) Isentropic Mach number distribution along the SS of the T106C for three different Reynolds number without turbulence grid (■, ▲ and ▲) and (b) intermittency factor evolution along the suction side for two Reynolds numbers with (▲ and ▲) and without (▼) turbulence grid with Tu = 1.8%, reproduced from [48].

transition using Hatman and Wand's concepts. Figure 2.16a illustrates the Reynolds number at separation with respect to the acceleration parameter at separation. The figure can directly be related to the Figure 2.10 where the momentum Reynolds number is correlated to the K_S. Actually, both representation are intuitively equivalent. However the Reynolds number correlate better than the momentum Reynolds number. But the use of the momentum Reynolds number allows to make a clearer classification (see Table 2.1). For high negative values of the acceleration parameter, the data correlate well with Hatman and Wang as well as with Thwaites models. In this figure, Hatman and Wang's curve is given in [24] by

$$\text{Re}_{s,S} = 5750 - \frac{215,000}{K_S \cdot 10^6} - \frac{45,000}{(K_S \cdot 10^6)^2} - \frac{5750}{(K_S \cdot 10^6)^3} - \frac{250}{(K_S \cdot 10^6)^4}. \tag{2.43}$$

Besides, Thwaites curve is obtained using Equation 2.38 and Houtermans correlation from [32]:

$$\text{Re}_{\theta,S} = 0.74\text{Re}_{s,S}^{0.488}. \tag{2.44}$$

Figure 2.16b shows the Reynolds number at the onset of transition with respect to the Reynolds number at separation. Again, Pacciani's et al and Michalek's et al. data correlate well with Hatman and Wang as well as with Houtermans correlation.
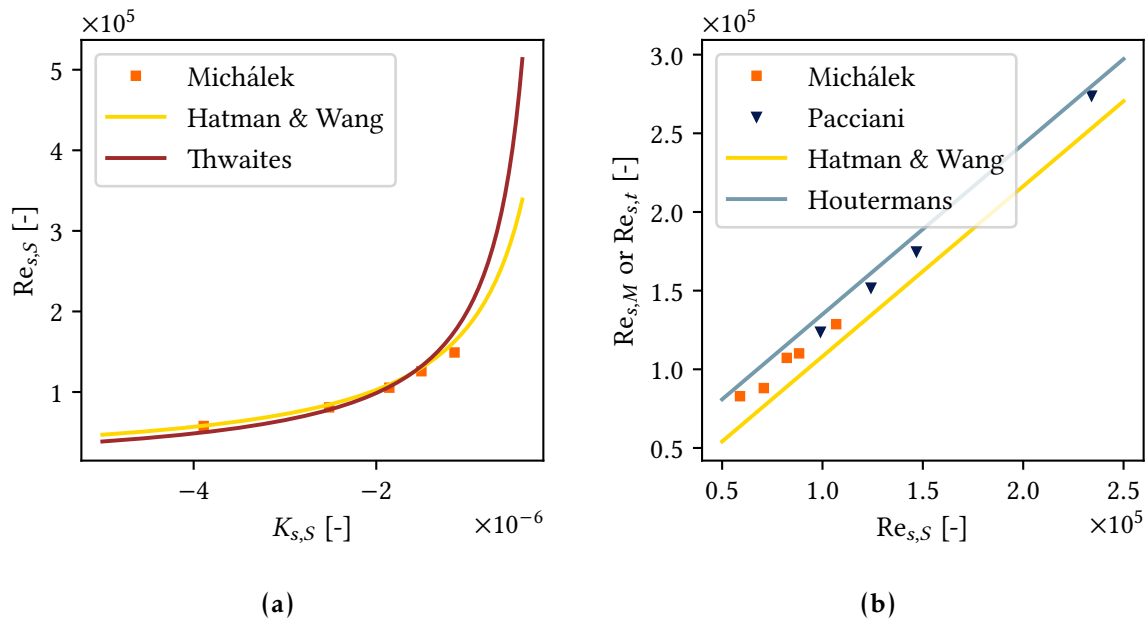
(a)

(b)

Figure 2.16: Reynolds number at separation with respect to the acceleration parameter at separation with no grid (a) and Reynolds number at the onset of transition with respect to the Reynolds number at separation (b), reproduced from [48].

The effect of Mach number on the loss generation of LP turbines has been experimentaly studied by Vazquez et al. [72]. They showed that compressibility allows to reduce the number of blades and increase the velocity ratio. The dominant contributor to losses is the variation of the pressure distribution over the airfoil surface. The very interesting conclusion on the LPT efficiency is that the efficiency increases thanks to the lower blade loading and the compressibility effects. Efficiency increase of 0.6% to 1% can be reached by reducing the number of components. These improvements can however be gain only at Mach numbers around 0.9.
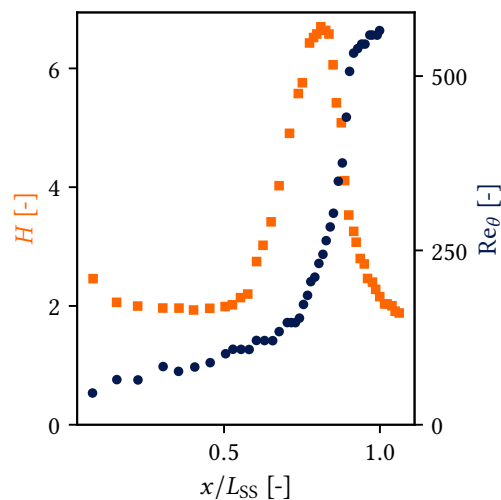
Figure 2.17: Boundary layer shape factor H and momentum thickness Reynolds number Re_θ computed by Dänhert et al. [15] for $Re = 80 \cdot 10^3$ and $Tu = 0.5\%$.

Michelassi's paper [49] presents a DNS simulations of a T106 linear cascade, varying turbulence level, reduction frequency and Reynolds number. Again, they showed that turbulence and incoming wakes permit to reduced or even suppress the separation bubble depending on the Tu and the reduced frequency. The dominant contributor to losses with attached BL is the momentum deficit. Turbulence reduce the mixed-out losses only for conditions with no incoming wakes, while it causes increase in losses for some of the investigated reduced frequency because of the wake mixing.

Dähnert et al. described the transition process interating with separation bubbles at low Reynolds number ($80,000$ to $300,000$) and low turbulence intensity. They showed that the type of instability involved are the KH instability mode. Figure 2.17 shows the shape factor and the momentum thickness Reynolds number for an outlet isentropic Reynolds number of $80,000$. The shape factor starts with a laminar value. The maximum of the shape factor indicates the onset of transition because it corresponds to the location of non zero intermittency. Then it decrease rapidly due to an increase in momentum thickness and a decrease in displacement thickness which is characteristic of transitional flow. It is shown later in this paper that intermittency reaches 1 before the end of the SS, implying turbulent flow before TE.

Chapter 3

Experimental environment

Since the beggining of the project, several works have already been undertaken. One of the major contribution has been provided by the VKI through an experimental campaign aiming to test the blade at on- and off-design conditions. The measurements were carried out on site at the S-1 / C facility and are documented in [40, 41, 43, 44]. As introduced earlier, one of the goals of the campaign was to fill the gap in experimental data dealing with unsteady wakes, purge streams, leakage and secondary flows. The data can thus be used with a view to validate further CFD models.

This thesis is in line with the continuity of the SPLEEN project and the experimental campaign that has been performed in this scope. The following chapter addresses different consideretions about the experimental measurements. The cascade design is firstly introduced with the blade geometry and the experimental apparatus. The main sensors that are used are shortly discussed as well as the quantity that are measured. The chapter is entirely based on [40, 41, 43, 44] from which come the large majority of the ideas.

3.1 Cascade design

The VKI S-1 / C facility in which the test case was developed is illustrated in Figure 3.1. As it
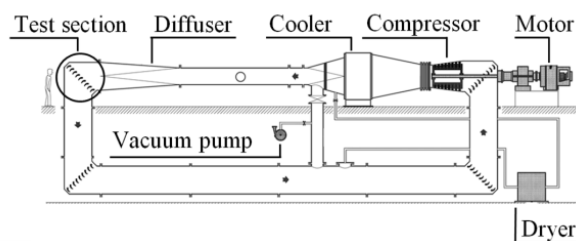
Figure 3.1: VKI S1-C wind tunnel, taken from [43].

can be seen, it consists in a closed-loop facility. The flow circulating inside the latter is generated by a 615 kW 13 stages axial flow compressor associated with a heat exchanger that allows to keep the temperature at ambiant conditions. The Reynolds and Mach numbers can be regulated independently respectively by controlling a pressure valve and adjusting the compressor rotational speed. This is a key feature permitting to test the cascade at low Reynolds and high Mach numbers.

The test setup can be visualized in Figure 3.2. A WG system, consisting in rotating bars, and a turbulence grid were added in front of the cascade to permit incoming wakes and turbulence, respectively, to be simulated. The cascade is composed of 23 airfoils in total, comprising

an interchangeble central bade. Depending on the test, the latter can be a smooth blade or a blade equipped with sensors. As the test case aims to study the effect of purge and leakage flows and secondary vortices in the linear cascade, some modifications of the facility had to be performed, giving rise to a particular design of the cascade. Among others, the endwall had to be translated in order to host the purge flow system, requiring the addition of a BL lip. Fig-
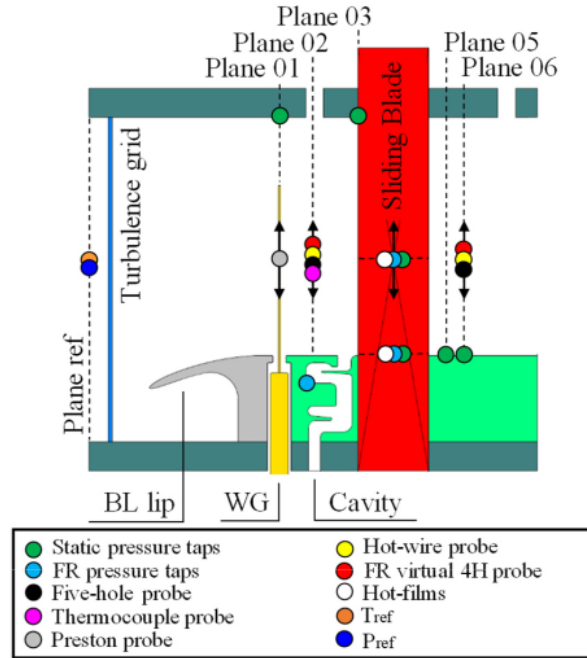

Figure 3.2: SPLEEN C1 cascade complete test setup with measurement planes and techniques, taken from [43].

ure 3.2 shows the different sensors and their locations. The data used in this study come mainly from the static pressure taps (green), the five-hole probes (black) and the hot films (white).

A section view of the SPLEEN C1 turbine blades and their geometric parameters are given in Figure 3.3. It is important to specify that even if the maximum thickness of the blades
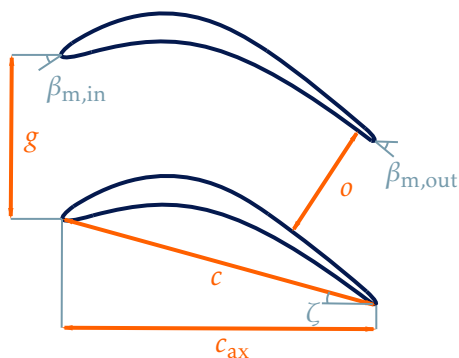
Parameter	Value
True chord, c [mm]	52.280
Axial chord, c_{ax} [mm]	47.610
Pitch, g [mm]	32.950
Span [mm]	165.000
TE radius, $d_{\mathrm{TE}}/2$ [mm]	0.435
Throat opening, o [mm]	19.400
Inlet angle, $\beta_{\mathrm{m,in}}$ [deg]	37.300
Outlet angle, $\beta_{\mathrm{m,out}}$ [deg]	53.800
Stagger angle, ζ [deg]	24.400
Maximum roughness, Ra [μm]	1.670

Figure 3.3: The SPLEEN C1 cascade passage geometry, reproduced from [39, 40, 41]. The geometry is not to scale.

well represent the engine configurations, the TE radius was enlarged for the installation of

the experimental instrumentation. The other parameters such as the pitch-to-chord ratio was chosen to alleviate separation on the SS. The objectives were to obtain an engine representative pressure distribution, especially near the LE.

The test campaign was articulated in three different phases:

- Phase 1: No incoming wakes (no WG) nor purge flow (flat continuous bottom endwall),

- Phase 2: Incoming wakes (WG installed), no purge flow

- Phase 3: Incoming wakes and purge flow (cavity installed).

This thesis only focuses on the phase 1, i.e. without WG nor cavity flows. Therefore, the measurements at the midspan plane are used in order to limit three dimensional effects.

Figure 3.2 informs on the reference system and the measurement planes. The reference total pressure and temperature were measured at the reference plane. The turbulence grid (TG) that is installed after the reference plane consists in a cartesian grid that triggers a certain level of turbulence in the inlet flow. Plane 01 is then located at the WG location while plane 02 is located between the WG and the cascade. The LE of the cascade corresponds with the plane 03 and the TE to the plane 04. Plane 05 and 06 are then located in the outlet flow field to characterize the turbine outlet. As it can be seen in Figure 3.2, each of the plane is equipped with sensors which are described in the next subsection.

3.2   Instrumentation

Axial locations of the six measurement planes are given in Table 3.1. These planes may also be seen in Figures 3.2 and 3.4.

(a) Reference system.

(b) Measurements planes.
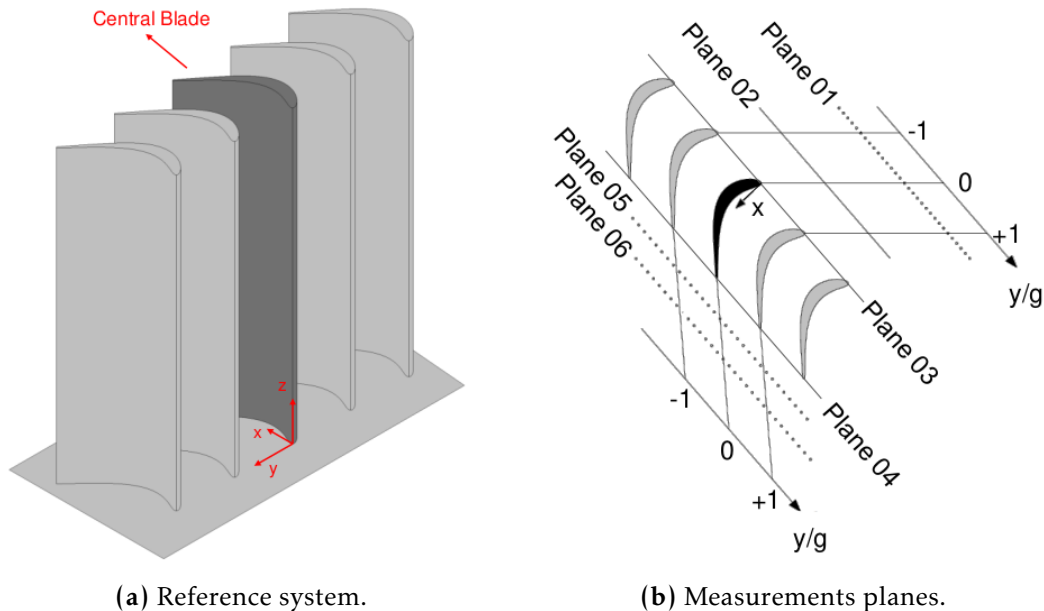
Figure 3.4: (a) Measurements reference system and (b) location of the measurement planes, taken from [40].

3.2.1   Probes

The test case were undertaken using several probes under different measurement scopes details of which are provided in Table 3.2. The total pressure is measured upstream of the turbulence

Table 3.1 Axial location of measurement planes, reproduced from [40].

Upstream		Blade		Downstream	
Plane 01	Plane 02	Plane 03	Plane 04	Plane 05	Plane 06
$-1.12c_{\mathrm{ax}}$	$-0.50c_{\mathrm{ax}}$	$0.00c_{\mathrm{ax}}$	$1.00c_{\mathrm{ax}}$	$1.25c_{\mathrm{ax}}$	$1.50c_{\mathrm{ax}}$

grid with two Pitot tubes, one at midspan and the other at a third width from the sidewall, in order to verify if the spanwise pressure gradient is zero, associated with an absolute pressure sensor WIKA P-30. Besides the total temperature is also measured upstream of the TG, with a K-type bare thermocouple. The pressure at planes 01, 03, 05 and 06 are measured by means of time-averaged pneumatic pressure taps along the upper endwall with diameter of 1 mm and along four pitches for planes 05 and 06. A single tap is also used to monitor the cascade base static pressure in order to properly regulate flow conditions and avoid interference. The pressure is recorded with the help of two Scanivalve MPS4264 miniaturized piezoresistive pressure units. More details and uncertainties are provided in [43].

Table 3.2 Probes of SPLEEN C1 experimental campaign, reproduced from [40].

Type	SPLEEN nomenclature	Measurement scopes
Preston boundary layer probe	P-PNEU-BL-01	Boundary layer profile and status (integral parameters)
Thermocouple type-K probe	P-ThermoK-01	Inlet Temperature profile
Single hot-wire measurement ($\parallel$ to the endwall)	P-HW-01	Inlet free-stream turbulence intensity + Boundary layer profile and status
Single hot-wire measurement ($\parallel$ to the cascade spanwise direction)	P-HW-02	Bar and blade wake turbulence intensity and length scales
Fast response virtual 4h probes	P-FR-4H-01	Unsteadiness of inlet and outlet flow conditions (p_0, pitch and yaw angle)
Pneumatic virtual 4h probe	P-PNEU-4H-01	Inlet and outlet flow conditions (p_0, pitch and yaw angle)
Miniature pneumatic 5h probe (Cobra-shaped) upstream measurements	P-PNEU-C5H-01	Inlet pitch and yaw angle (p_0, pitch and yaw angle)
Miniature pneumatic 5h probe (L-shaped) downstream measurements	P-PNEU-L5H-01	Outlet flow conditions (p_0, pitch and yaw angle

Only some interesting points about the probes of Table 3.2 are discussed in this section. More details can be found in [40, 41, 43, 44]. The probes were allowed to move in the pitchwise and spanwise directions and to rotate thanks to different motors with an accuracy of ±0.1 mm and a yaw accuracy of ±0.1 deg. It is important to note that two different probes, oriented parallel to the cascade endwall and parallel to the probe axis, are used for the HW measurements at the inlet. The former allows to characterize the free-stream turbulence at the inlet and BL profile. The latter is used to measure the WG (not the focus in this thesis) and blade turbulence

intensity and length scales. The turbulence intensity is measured by a HW probe in constant temperature mode associated with Dantec Dynamics Streamline Pro anemometer. The signals were acquired during 3 seconds at a frequency of 120 kHz.

3.2.2 Blade surface measurements

For the blade measurements of the cascade equipped with 23 adjacent blades, five different versions of the central blade were employed. During the probe measurements however, a smooth blade is used. The central blade thus consists in a sliding instrumented blade, which allows to take measurements along the spanwise direction by translating the array of sensors. The sensors that were used for this purpose are listed in Table 3.3 and the geometries of the instrumented blades are shown in Figures 3.5 and 3.6.

Table 3.3 Blade surface sensors of SPLEEN C1 experimental campaign.

Type	SPLEEN nomenclature	Number	Measurement scopes
Suction side pneumatic taps	B-PNEU-SS	24	Blade static pressure profile
Suction side fast response sensors	B-FR-SS	7	Blade static pressure distribution and statistics
Pressure side pneumatic taps and fast response sensors	B-PNEU-FR-PS	17 and 1	Blade static pressure distribution and statistics
Hot-film gauges	B-HF	53 (32 on SS, 21 on PS)	Quasi-wall shear stress distribution and statistics

3.2.3 Limitations

An important limitation concerns the manner in which are used these sensors. The hot wires and films allow only to measure the quasi-wall shear stress along one particular direction while the wall shear stress is function of two curvilinear directions along the blade surface. The actual shear stress can be precisely determined in the numerical scope, but is not defined in a rigorous way in the experimental study. In theory, the surface mounted hot-films can measure the wall shear stress by

$$\tau_w = \left(\frac{Q}{\Delta T \cdot k}\right)^3, \tag{3.1}$$

where Q is the convective heat flux, ΔT is the temperature difference between the fluid and the hot film and k is the heat transfer coefficient. In order to make this measurement reliable, an extensive calibration is required. Only a qualitative equivalent of the wall shear stress, called the quasi-wall shear stress, could be measured and is defined as

$$\tau_q = \left(\frac{Q - Q_0}{Q_0}\right)^3 \approx \left(\frac{E - E_0}{E_0}\right)^3, \tag{3.2}$$

where Q is the total dissipated power by each sensor [W], Q_0 is the total dissipated power without flow [K], E is the bridge voltage with flow [V] and E_0 is the bridge voltage without flow.

(a) B-PNEU-SS

(b) B-FR-SS

(c) B-PNEU-FR-PS
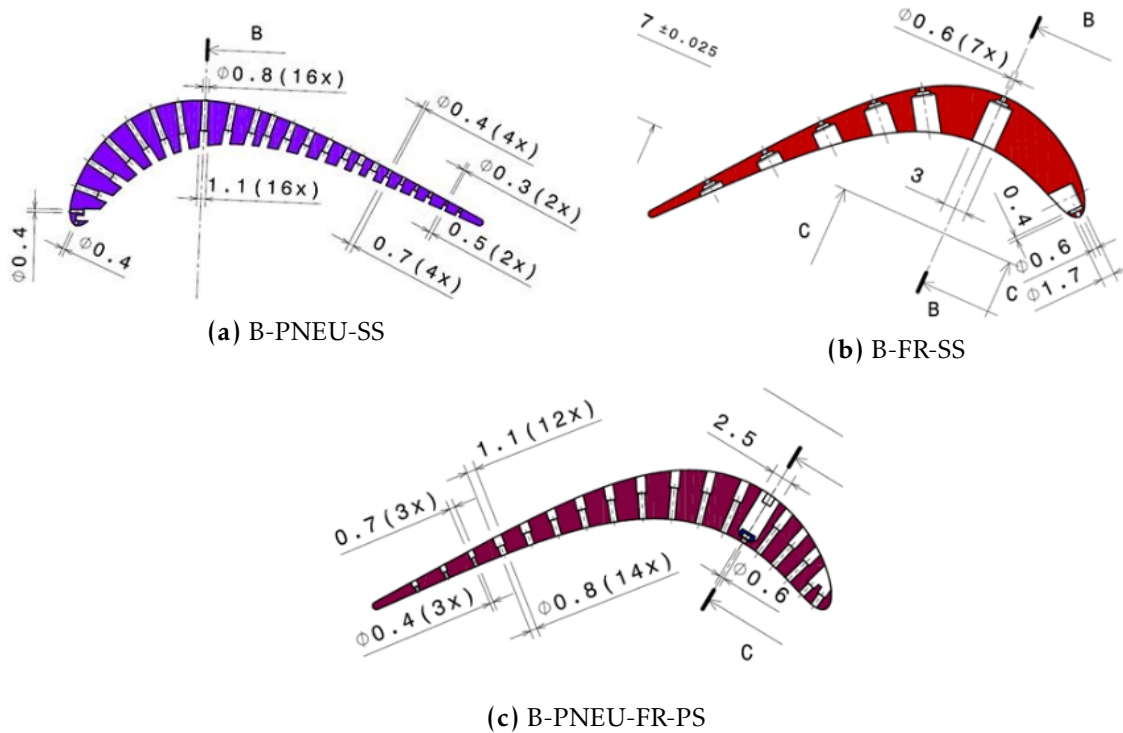
Figure 3.5: Blade measurements pneumatic and fast response sensors locations and dimensions, taken from [40].
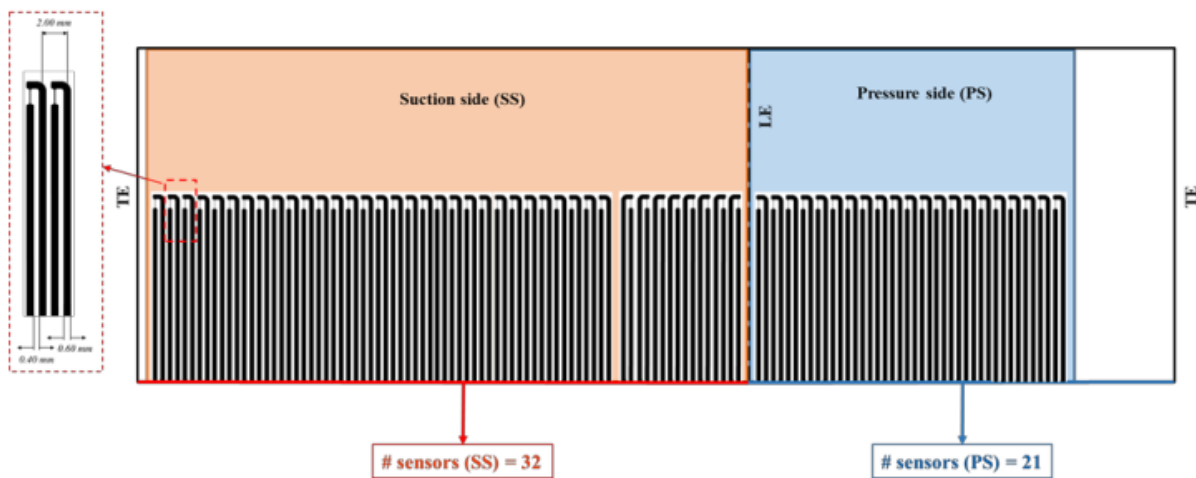

Figure 3.6: Blade measurements hot films sensors locations and dimensions, taken from [40].

Moreover, this voltage had to be corrected to compensate the increase of flow temperature and blade metal temperature during testing days. The comparison between numerical and experimental data will then only be qualitative for this quantity. This does not prevent us of finding precise and meaningful numerical results nor locating precisely the separation location.

Additionally, the sensors and probes have a certain size, which can disturb the flow. It is especially the case for cobra, L-shaped probes and Pitot tubes placed within the flow. The potential field is slightly changed as well as the blade loading, as investigated in [42, 70]. This effect can be decreased by decreasing the size of the probes. However at a certain level, this downsizing is not possible anymore. It can also introduce total pressure losses and induce

additional turbulence level in the cascade. This has been investigated in [40].

Most of these problems are not met in numerical computations: Numerical computations are non-intrusive and don't require correctly calibrated sensors. Experiments aim to represent real conditions. Numerics allow to circumvent the encountered limitations of experiments but are based on mathematical and physical models which are often ideal. Another striking difference is the computational cost of these computations. Once installed, experimental tests can be used to record several seconds of flow in a relatively reasonable amount of time. However, when the used technique is DNS, computations may last weeks for only some milliseconds of flow. Moreover, while the resolution highly depends on the type of sensor in experiments, in CFD the resolution depends on the timestep, which depends on stability and convergence considerations. Finally, it is important to note that errors are also inherent to numerical simulations, depending on the boundary conditions[1], the used method, the grid refinement, etc. Depending on the spatial and temporal discretization, the error may be reduced but will always be present. These considerations are detailed in the next chapter.

3.3   Operating conditions

Refering to Chapter 2, the operating conditions are defined by the outlet quantities, i.e. at plane 06:

$$Re_{is,out} = Re_{is,06} \equiv Re, \tag{3.3}$$
$$M_{is,out} = M_{is,06} \equiv M. \tag{3.4}$$

As the geometric parameters of the cascade are fixed, the only way to vary the Reynolds number is by changing the density and the velocity. As detailed above, this is permitted thanks to the VKI S1-C wind tunnel. The different conditions that have been studied are given in Table 3.4. The letters B and F denote respectively blade and flow field. On-design conditions are highlighted in blue and the conditions investigated in the experimental study are highlighted in orange. They correspond to conditions encountered during the cruise. It is important to note that a turbulence intensity of Tu = 2.5% is targeted in the experimental study while it is zero in the numerical study. Moreover, as stated in [48], the background free-stream turbulence is naturally of 0.9% inside the facility.

Table 3.4 Investigated conditions in the experimental studies, reproduced from [44].

		M			
		0.7	0.8	**0.9**	0.95
Re	$65 \cdot 10^3$	B	B	B	-
	$\mathbf{70 \cdot 10^3}$	**B,F**	B,F	**B,F**	**B,F**
	$100 \cdot 10^3$	B	B	B	B
	$120 \cdot 10^3$	B	B,F	B,F	B

---

[1]Boundary conditions are the first source of errors in numerical computations.

Chapter 4

Numerical environment

Numerical results play an important role in this work as it constitutes its main contribution to the SPLEEN project. The chosen level of fidelity is DNS, that computes all range of scales as detailed above. DNS has been chosen rather than RANS or LES because a sharp understanding of the physics is sought. Compressibility, separation and transition to turbulence are omnipresent in LPT and interact with each other. The utilization of RANS or LES would kill the small scales and in turn turbulence would not be represented with the needed accuracy. However DNS requires important numerical resources and can't be performed on a regular computer. The numerical resources for such a simulation can be estimated to be of the order of Re^3. It is therefore possible for the studied conditions in LPT but to this purpose high performance computers are needed. In addition, in order to decrease the numerical cost and increase the accuracy, higher order methods are used. In the scope of this thesis the selected method is ArgoDG, developed in [9, 27], which implements the discontinuous Galerkin method. The DGM presents properties and advantages for elliptic and hyperbolic problems.

This chapter introduces the numerical environment: the HPC and Zenobe, ArgoDG and the DGM. It also details the simulation setup, i.e. the domain, the mesh, the boundary conditions (BC) and the settings, that were used to obtain the presented results and that were initially defined in [6, 35].

4.1   High performance computer and ArgoDG

The end of the twentieth century and the beginning of the twenty-first was marked by the emergence of computer technologies and all the benefits that come with them. From a scientific point of view it can be seen as a complement to experimental methods, i.e. this is a way to perform calculations and simulations that wouldn't be possible in reality. In some particular cases, simulations are the only way to study a phenomenon. Indeed some experiments can be cost or practically prohibitive or even impossible. In general it is interesting to have both experimental and numerical results to compare them. It allows to take benefits from the complementarity of experiments and simulations. In the context of turbomachinery measurements are often intrusive[1]: they modify the flow field by introducing perturbations, turbulence or modifying the potential field even if the probes are very narrow. Finally, simulations capabilities are based on computer power, especially for DNS. Computer power is mostly defined by memory capacity, total compute processors and processors performance. For all these reasons, HPC is needed to achieve precise turbomachinery DNS calculations.

Scientific computing can be defined [12, 21] as "The efficient computation of constructive

---

[1]There are some exceptions, as particle image velocimetry (PIV), Schlieren (e.g. [7]), etc.

methods in applied mathematics". It is used in material sciences, weather forecasting, heating, automotive, biomedical engineering, electrical engineering, aerospace, etc. A list of the 500 best performing HPCs is provided at top500.org. In Belgium, HPCs are managed by the "Consortium des Equipements de Calcul Intensif" (CECI), funded by the "Fond national de la recherche scientifique" (FNRS). There are six clusters in total but the one used in this work is Zenobe, shown in Figure 4.1, which is the Tier-1 cluster of Cenaero [63]. It was the 475th world most powerful computer in the world in June 2016 but is no longer in this list.

Figure 4.1: Photo of Zenobe Tier-1 HPC, taken from [10].

Zenobe was build in 2011. At that time, it contained 3300 cores but it was upgraded in 2013 with 8200 cores and 2015 with 5760 cores. Nowadays, it is composed of 13,536 cores with up to 64 GB of RAM each as stated in [10]. It is interconnected with a QDR/FDR (Quad Data Rate / Fourteen Data Rate) mixed Infiniband network, which is the best interconnecting solution for current high-performance and data center clusters, and have access to a fast 350 TB GPFS filesystem. Zenobe has a power of 330 TFLOPS, i.e. $330 \cdot 10^{12}$ floating operations per second, and a total storage of 470 TB. Each user has a quota of 50 GB in his home directory.

In Zenobe, each node controls 24 central processing units (CPU), which are working in parallel. The computation time and resources are managed by PBSPro version 13 (see [77]). It offers two queues:

- large: it is the largest one with 8208 cores by 24 cores per node. The jobs are limited to 24 hours walltime, using at least 96 and at most 4320 CPU.

- main: it contains 5760 (24 per node) last-generation Haswell cores. There is no time limitation.

Thanks to the PBS server, numerical resources are equally distributed between users. Jobs are submitted through a *.pbs file informing on the required time, the amount of CPU, the input and output directories, etc.

4.1.1 ArgoDG

The fundamental tool that is used in this work to perform DNS is ArgoDG, implemented in Zenobe. ArgoDG is a 3D DNS solver that was created in Cenaero (see [9, 27]) and was already used in several EU programs such as Adigma, IDIHOM, Tilda and HiFiTurb. The domain geometry and mesh can be built with Gmsh and the data can further be read with ParaView or are exported as *.dat / *.csv files. Simulations are controled by *.in input files, which specifies all the parameters of the simulation (e.g. directories, initial solution, mesh, topology, probes sets, time dependence parameters, physics of the problem, boundary and initial conditions, etc.). A lot of flexibility is allowed in the parametrization of the simulations. For example, it is possible to choose the type of polynomial, define a stabilisation method or set other options.

Solution, i.e. density, momentum and energy density, is computed over the whole domain. There is also a large range of possible outputs that can be obtained from the solution. In addition to the domain, it is feasible to output data over lines or at particular points using probes. On the other hand, post processing can also be performed on ParaView.

In turbomachinery, especially in this project, DNS is empowered thanks to special methods, called higher order methods. Indeed, simple FEM (rather used to solve parabolic or elliptic problems) is not suitable for flows while stabilized FEM is suitable for incompressible flows. Besides, FVM or FDM could be used (for convection-diffusion problems). The FVM is usually considered powerfull for CFD thanks to the manipulation of numerical fluxes. The solution is constantly approximated in each volume and the continuity requirements at their interfaces are relaxed. At the contrary, the main idea behind the FEM is to impose continuity at the elements interfaces while performing polynomial interpolation of the solution within each element. FVM is more suitable for compressible than incompressible flows. The FEM allows to reach higher order solution but can be problematic when solving convection-diffusion equations or problems containing discontinuities, typically shocks. The main issue is the difference between standard, second order industrial type CFD on one hand and high order methods on the other. The latter are required to resolve the fine scales of the turbulence which are high-frequency with respect to the mesh, which would otherwise be dissipated away and convected at the wrong speed. The last two decades have been marked by the emergence of the *discontinous Galerkin method*. This method combines the strength both of the FEM and the FVM, permitting to reach higher orders while being stable for convection-diffusion problems. The combination of both method is done by relaxing the continuity requirements at the element interfaces, rather making the use of numerical fluxes, and performing high order polynomial interpolation within elements. ArgoDG combines the DGM for convective problems with the SIPDG for diffusive fluxes.

An illustration is given in Figure 4.2 to provide a brief glance at the method principles. In this figure, a trial space $\mathcal{U}_h^N$, with the mesh size h and the number of elements N, is represented. It converges to the solution space as the mesh size is reduced. The general idea behind the FEM is to require the residual of the equations to be orthogonal to all members v of a suitably chosen test space $\mathcal{V}_e^N$. Galerkin variational formulation consists in choosing $\mathcal{V}_e^N = \mathcal{U}_h^N$. The trial space of DGM is broken, i.e. its elements consist of vectors of functions which are fully regular within the element but not necessarily continuous across elements, as detailed in [19, 28]. This makes the interest of DGM: any shape function can be supported on a single element, the order of interpolation can change from element to element and there is a full freedom for the choice of basis functions within an element.
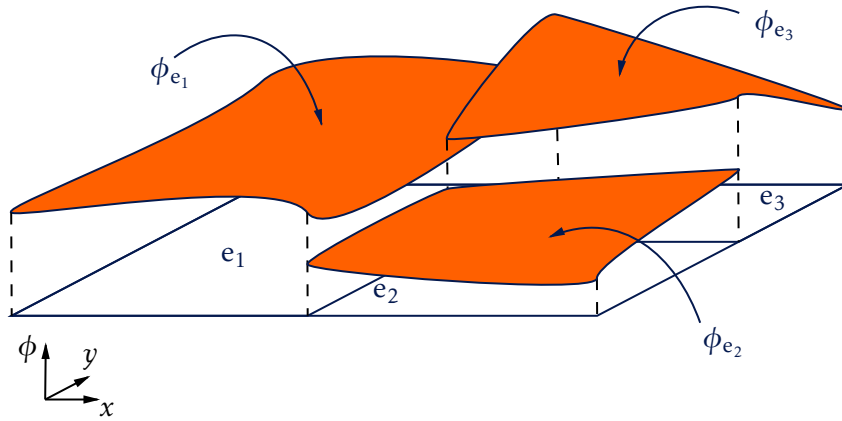
Figure 4.2: An element of the DGM broken space, reproduced from [28].

4.2   Pre-processing of the cases

Flow conditions considered for the numerical study are summarized in Table 4.1.

Table 4.1 Flow conditions of the test case.

Quantity	Symbol	Value			Units
Is. out. Reynolds number	Re	$70 \cdot 10^3$			[-]
Is. out. Mach number	M	0.7	0.9	0.95	[-]
Inlet total pressure	$p_{0,\text{in}}$	$10,779.39$	9500.24	9318.31	[Pa]
Outle static pressure	p_{out}	7771.16	5617.12	5213.22	[Pa]
Inlet total temperature	$T_{0,\text{in}}$	300			[K]
Flow angle	α	36.3			[°]

Selecting a DNS model implies to resolve the NSE as they stand, without introducing any averaging beforehand. Compressibility, viscosity as well as turbulence with an expected three-dimensional flow are to be taken into account, while computational costs are a less binding limitation. This justifies the choice of the method for which no turbulence closure model is needed. Modelling shocks and transition together is a cumbersome task that is handled by HPC and DGM.

The discontinuous Galerkin fluid problem in ArgoDG is set up needing particular requirements in terms of grid generation, boundary and initial conditions, schemes and solvers, etc. These considerations are addressed in the following section.

4.2.1   Computational domain and mesh

In a linear turbine cascade, the flow around each one of the blades can be assumed the same. The analysis can thus be limited to a single blade associated with periodic BC allowing to take the effects of the adjacent blades into account. The computational domain that has been defined in [6] is shown in Figure 4.3. As building arguments, the solution should not be impacted by the domain. It is ensured by setting inlet and outlet boundaries far enough to the blade, respectively at distances of $2 \cdot c_{\text{ax}}$ and $2.4 \cdot c_{\text{ax}}$ from the blade LE and TE. Generally, it is imposed by the position of the different stages blade rows (rotor-stator) of the turbomachine. Here, the focus is on the linear turbine cascade and its self-induced effect which justify this choice.

Moreover, the outlet is further away than the inlet in order to have a larger region to analyse the wake. On the other hand the distance between the top and bottom is determined by the blade spacing. The geometric parameters of the cascade are given in Figure 3.3.
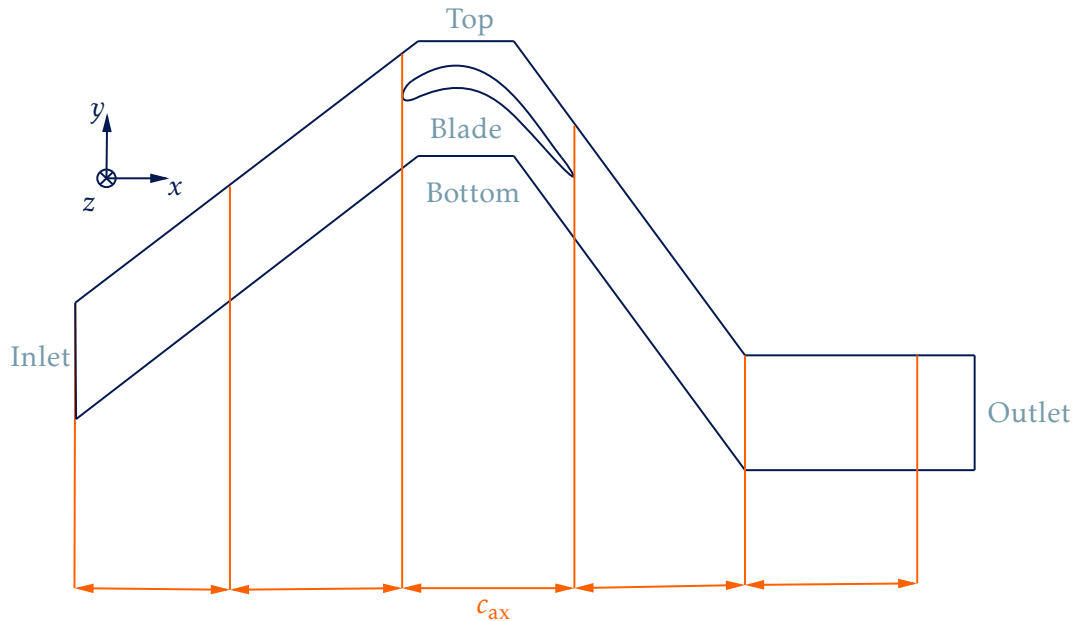
Figure 4.3: Computational domain, reproduced from [6].

Once the computational domain is defined, it must be meshed. Different versions of the mesh were built in [6] then reused in [35]. The computational domain was the same for both of the meshes, the differences laying in the size of their elements. The second mesh was defined after the first one was deemed to be tainted by lack of precision. In this section, only the final mesh, that reached convergence, is detailed. The meshes were coded with Gmsh 4.5.6 with the help of *.geo scripts.

The mesh is presented in Figure 4.4. The mesh consists in an unstructured mesh far from the blade and a O-type structured mesh of thickness of 0.76 mm close to the blade. The element close to the blade have a tangential length of 0.38% of the real chord c and an exponential biaising of ratio 1.2 is used. Three refinement zones may be identified: the LE, TE and the base region. Near the LE and TE, the element sizes are of 0.08% of c while they are of 0.76% of c in the base flow. In the passage refinement zone, which extends from LE to $1.5 \cdot c_{ax}$, the cell sizes are of 1.5% of c while the maximum element size in the domain is of 7.5% of c in regions where precision isn't required. The base flow refinement zone, which extends from TE up to $0.5 \cdot c_{ax}$, shows a reference cell size of 0.75% of c. The elements adjacent to the surface are forced to fit with it with the help of curved element of order 2 and an order of resolution of 3. Finally, the mesh was extruded in the z direction (see Figure 4.3) on 10 layers resulting in spanwize element of size of 0.35% of c.

The quality of this mesh was checked in [6]. It was stated from the statistics that the mesh contains no prismatic elements. The Jacobian ratio, defining the validity of the mesh, is comprised between 0.145 and 1 with a high average of 0.73. The gamma coefficient, that is the ratio of inscribed over circumscribed radius and thus can be interpreted as the skewness, ranges between 0.25 and 0.9 with an average of 0.82 and values of 0.9 close to the blade. These statistics give confidence about the quality of the mesh which ensures a high accuracy associated with low memory requirements.

The idea behind the grid was to have the best possible spatial resolution around the blade.
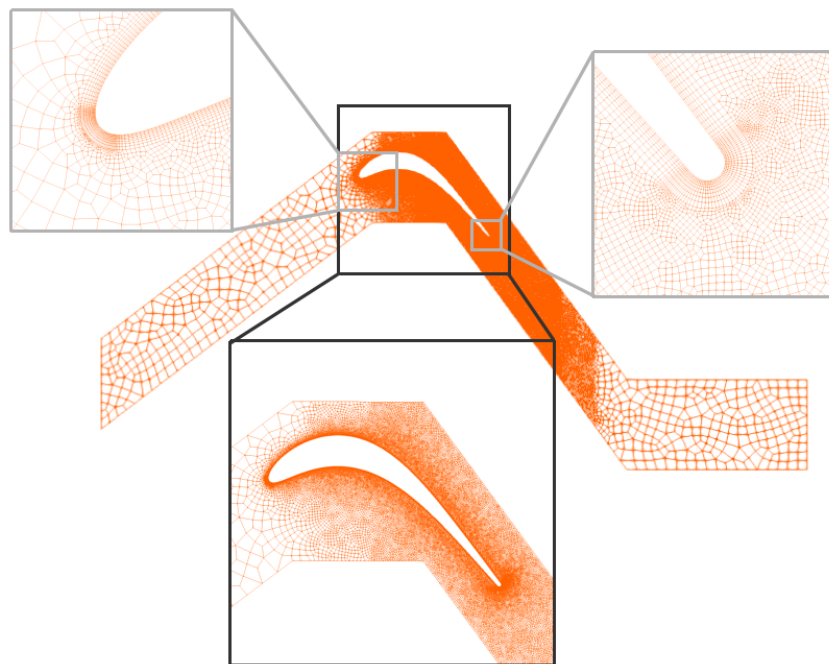
Figure 4.4: Computational grid.

Refering to Chapter 2 and especially Figure 2.3b, a good spatial resolution of the mesh is associated with values of wall units ranging between 5 and 10, which comes from a tradeoff between computational cost and accuracy. However, in this analysis, the wall units must range between 15 and 30. This is explained by the fact that elements are of third order, meaning that the first node is actually at the computed length scale divided by 3.

The normal and tangential resolutions are shown in Figure 4.5. The trends are identical for the three conditions, with a more oscillatory behavior for the low Mach number case. The curves are snapshots at mid-span, however since convergence is reached (see next section), they are representative of average resolution, or at least of the same order. The resolution critera is respected everywhere on the blade. Even if it does not exceed the maximal value, the peak at LE can be ignored since it corresponds to the LE anomaly encountered in unsteady simulations. Very low values appear at the beginning of the PS and the end of the SS, which means that the mesh is finer than wanted in these regions. Moreover, the global normal resolution is much lower than the maximal limit discussed in Chapter 2 for a even greater precision but a higher computational time.

Capabilities of ArgoDG and Zenobe are maximized by using a partitionned mesh, which may drastically accelerate the calculations. The idea is to use the parallelisation of the CPU working in a node. Each node controlling 24 CPU, the number of partition is fixed at 96, i.e. four times the number of CPU in a node such that the computation takes the same amount of time in each node. Moreover, the chosen multiple of 24 is based on a tradeoff between speed and computational resources: more partitions means faster computations but requires more CPUs. The distribution of tasks is then controlled by Zenobe and the *.pbs submission file.

The flow physics requires an unsteady simulation of which the average must converge to a fixed value: the flow is said statistically steady, i.e. the time average doesn't change over time. To ensure that transitient features are no longer present in the flow, a convergence study must be undertaken. Such convergence studies were performed in [6] for the case $M = 0.9$ and

(a) Normal resolution.

(b) Tangential resolution.
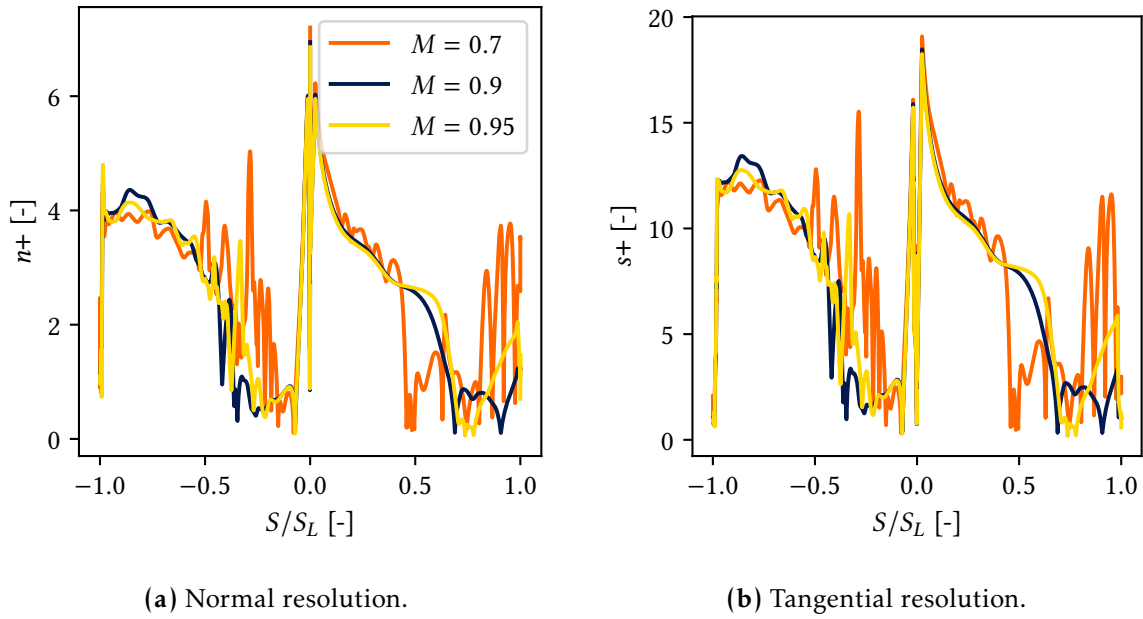
Figure 4.5: Snaptshots of the wall resolution along the blade SS and PS at midspan for each studied conditions.

in [35] for the case[2] $M = 0.95$. These considerations are still provided in this thesis for the sake of precision and rigor, especially for the case $M = 0.7$ which wasn't checked. Figure 4.6 shows the convergence for the three cases. It is studied in terms of density convective fluxes difference at the boundaries, i.e. the idea is to check if continuity is satisfied in the domain. The y-axis is thus the outlet subtracted with the inlet density fluxes. The x-axis is the time step, where the first time step corresponds to the first mesh that was used which induced large osciltions for the next steps. At steady state, the mass flow rate through the inlet and the mass flow rate through the outlet should cancel each other. The averages (dashed lines in the Figure 4.6) are computed using the last 1000 time step in order to avoid the effect of the first time steps. In average, this criterion is satisfied for each case. However, a highly oscillatory behavior remains, that is even stronger for the low Mach number case. To circumvent this problem, steady state was considered reached in [6] neglecting the small error. Figure 4.6 also shows the CPU time with respect to the time step. Here, CPU time has been divided by the number of used CPUs, i.e. 4 CPUs per node with 192 nodes, and rescale to days. It can be seen that these simulations take a very long time to reach convergence. Again, in [6] the number of time steps required to reach convergence was computed to be 10000 for the $M = 0.9$ case, which corresponds to 6 to 10 days of computation. The number of days of computation for $M = 0.7$ far exceeds this number, while the cases $M = 0.9$ and 0.95 runned for almost 15 days. Finally, the cases will continue to run after this thesis. All these considerations justify the choice of neglecting the small oscillations and focus only on the converged average.

4.2.2   Boundary conditions

The solved equations and the domain geometry for the three cases are the same: the only difference resides in the BC. They play an important role in the simulation and are the main

---

[2]The convergence study for this particular case, $M = 0.95$ does not appear in the disseration but convergence was assumed to be reached.

(a) $M = 0.7$.

(b) $M = 0.9$.

(c) $M = 0.95$.
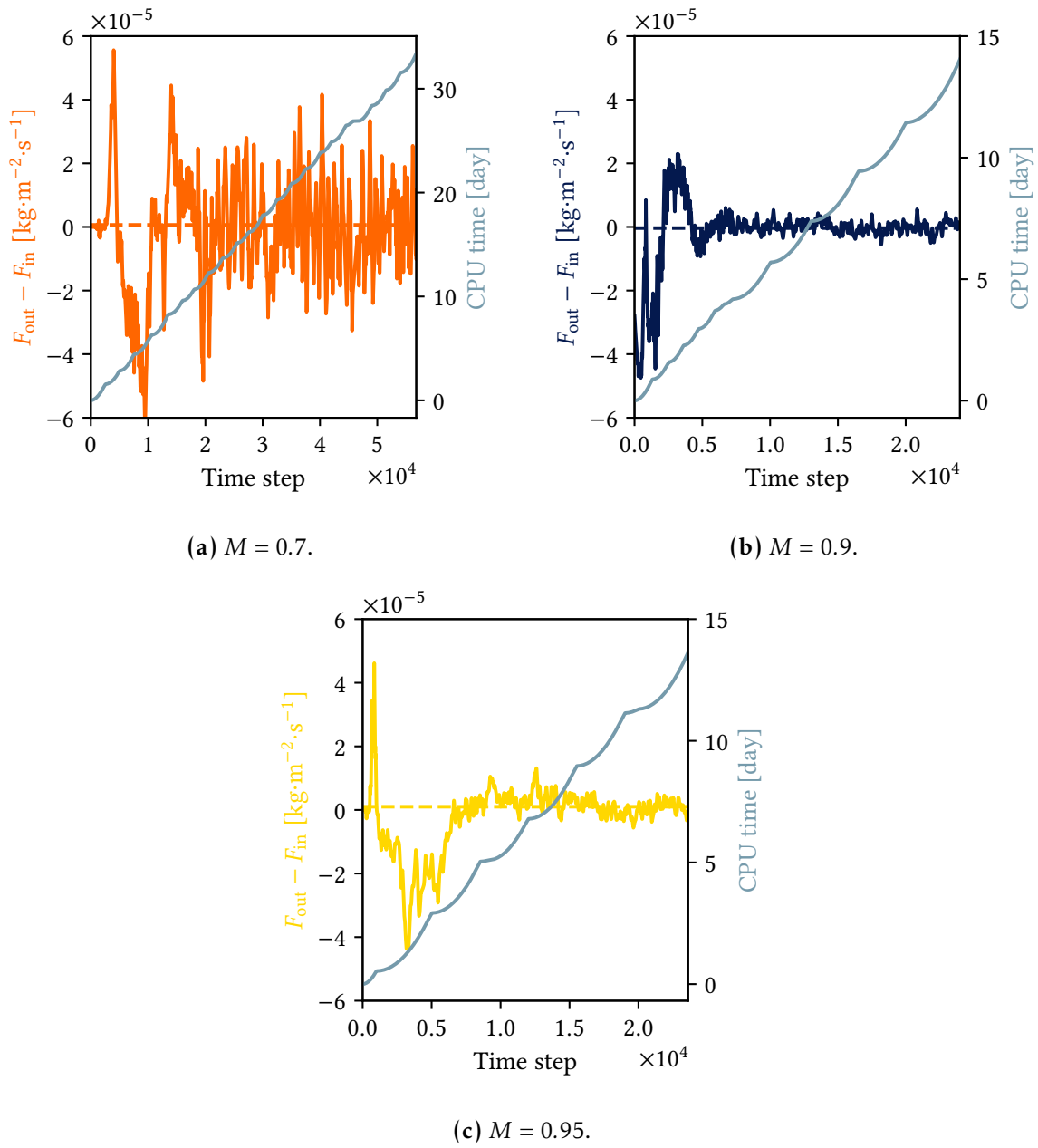
Figure 4.6: Convergence of the density flux budget in the domain for the cases $M = 0.7$, 0.9 and 0.95.

contributors to errors. Five boundaries can be distinguished in Figure 4.3: the inlet, the outlet, the top, the bottom and the blade. BC must be defined on all these boundaries.

Periodic BC are assigned to the top and bottom permitting to simulate the influence of the other blades. No-slip and adiabatic conditions are enforced at the blade surface, i.e. velocity and energy transfer are zero at the surface.

Since the equations are unsteady and transonic conditions are reached within the flow, 3 quantities are imposed at the inlet and 1 quantity is imposed at the outlet (see [29, 67]). The quantities imposed at the inlet are the total pressure, the total temperature and the flow angle. At the outlet, the static pressure is fixed. The BC are summurized in Table 4.1.

Some verifications may be undertaken after reaching the convergence. The method con-

sists in imposing the value of the first element after the inlet. It allows to have a state of the effect of the boundaries on the solution. It was found in [6] that the only parameter to change was the inlet total pressure with less than 0.9% of variation due to the penalty method (see next section). In the wake, only 1% of variation was found in static pressure. Moreover, the change in Mach number was of the order of 10^{-6} at the inlet. The effect of boundaries was also investigated by plotting the streamlines in the flow at the inlet. Finally, in order to check the effect of periodic boundary in *z*, turbulent coherent structures were computed and showed to be smaller than the extrude distance. For all these reasons, the effect of boundaries can be assumed to be minimized.

Two suggestions were made in [6] to verify the boundaries effect more deeply:

1. Perform different simulations and convergence studies with different domain and mesh, which is prohibitive in view of CPU time and,

2. Check the spanwise correlations to ensure that turbulent structures are not broken by the extrude distance.

4.2.3 Schemes and solvers

Now that the mathematical model and the BC have been fixed, the equations must be discretized using adequate numerical schemes. The solved equations are the continuity, momentum and energy equations. The fluid properties as fixed to ideal gas, with $\gamma = 1.4$ and $R = 287.06\,\mathrm{J\,kg^{-1}\,K^{-1}}$, and the Sutherland viscosity law of Equation 2.6 allows to derive the viscosity. In order to perform non-dimensionalization, a reference pressure and temperature have been fixed as well, respectively $p_{\mathrm{ref}} = 6000\,\mathrm{Pa}$ and $T_{\mathrm{ref}} = 260\,\mathrm{K}$.

Since the solved equations are unsteady, a temporal discretization scheme must be defined. The idea is to chose a scheme that is not too dissipative in order to avoid to kill turbulent structures. The second order backwards difference time-integration scheme (implicit BDF2) with a non-tolerance of 10^{-4} and a Jacobian matrix frozen for 2 steps. The time step is fixed at 10^{-7} for each case in order to satisfy the CFL condition.

The Jacobian matrix depends on the number of degree of freedom, this matrix cost a large amount of computational time. A way to accelerate the computation is to freeze the matrix, i.e. the solver will consider a constant Jacobian for a fixed number of timesteps. This method is also used for the space discretization, inside a timestep.

Besides, the spatial discretization is chosen to be SIPDG, i.e. symmetric interior penalty discontinuous Galerkin. These techniques (SIPG) were initially introduced for elliptic and parabolic problems. The interior and boundary penalty means that subsets of finite element spaces are not necessary to approximate the Dirichlet boundary conditions. It is needed for discretizing the viscous terms of the NSE. Unlike in classical FEM, additional terms on the cell boundaries are needed for consistency and stability. Note that here, no specific adaptation of the scheme is used for the computations of the shocks: they are sufficiently weak, such that no stabilization is required. These considerations are actually out of the scope of this thesis. However what may be remembered is that DGM is more suitable than FVM and FEM for non-linear convection-diffusion problems, characterized by viscosity and steep gradients (shocks, discontinuities), because the solution is approximated by a piecewise high order polynomials within the cells and continuity requirements are relaxed at the interfaces. The DGM thus contributes to convective problems, i.e. upwind fluxes, which can be interpreted as a central flux combined with a penalitation of the solution difference. Besides, the SIP covers the diffusive subsystem, i.e. diffusive fluxes. More details can be found in [19].

Note that, as the simulations are considered to be converged, it is not of prime necessity to review the initial conditions. They have been chosen in the first work in order to boost

the convergence rate by imposing the inlet flow direction as well as the Mach number. The Mach number was fixed to 0.01 in the axial direction and total temperature and pressure were imposed on the whole domain. In this way, acoustic perturbations are forced to propagate and convergence is reached faster.

Chapter 5

Results and discussion

This chapter presents the results obtained for different Reynolds and Mach numbers, i.e. low ($70 \cdot 10^3$) Reynolds number and low (0.7), moderate (0.9) and high (0.95) Mach numbers[1]. This large range gives the possibility to understand the flow behavior in on- and off-design conditions and the have a deeper comprehension of compressibility effects. The cases are compared with experimental data as well as between them.

With a view to visualize the flow and sharpen intuition, a section is firstly dedicated to the flow visualization. Blade loading for each case is then presented with the isentropic Mach number and the skin friction coefficient distributions over the blade. They are compared to experimental measurements as well as between them. Subsequently, the boundary layer developing on the pressure and suction sides are further studied using the velocity profiles and the BL parameters. A first state of the turbulent behavior of the BL is proposed. Afterwards the wake is investigated using pressure losses, flow deviation and Reynolds stresses. Finally, a sharper study of the wake with spectra is performed.

5.1 Passage visualization

An interesting feature of turbomachinery CFD is the visualization of the passage. It allows to have a general vision of the flow. In this thesis, the postprocessing is partly undertaken in ParaView as it constitutes a robust opensource visualization software. Three fields are explored in this section: the Mach number, the vorticity and the density gradients ($\nabla \rho / \rho$) fields.

Figure 5.1 provides snapshots of the Mach number in the flow field for Re = $70 \cdot 10^3$ and $M = 0.7$, 0.9 and 0.95. For each cases, the PS experiences a large separation bubble. However, this separation is smaller for the low Mach number case for which the flow seems highly perturbated at reattachment. The bubble is smaller for the highest Mach number case as well, with turbulent quantities formed at reattachment and convected downstream. For the moderate Mach number case, the flow reattaches more smoothly. the suction side also experiences separation for $M = 0.7$ and 0.9. For $M = 0.95$ no statement can be drawn at this point.

The flow field between the blades is quite perturbated for the lowest Mach number case: acoustic perturbations are created at the TE by vortex shedding and go upstream before being attenuated. Besides, for these conditions vortex shedding is triggered just in front of the TE, forcing the BL to be modulated and periodically decreasing the displacement effect of the BL perpendicular to the wall. The wake is highly perturbated, composed of non-staggered vortices spaced in a non-uniform way. It suggests that the vortex street is unstable (see Section 2.5.2). Turbulent decay is important in the wake associated with a high concentration in Reynolds

---

[1]Note that the terms low, moderate and high are not used in an absolutely quantitative sense but in order to differentiate the cases.

stresses and a strong turbulent intensity (see Section 5.5). The flow fields between the blades

(a) $M = 0.7$ **(b)** $M = 0.9$

(c) $M = 0.95$
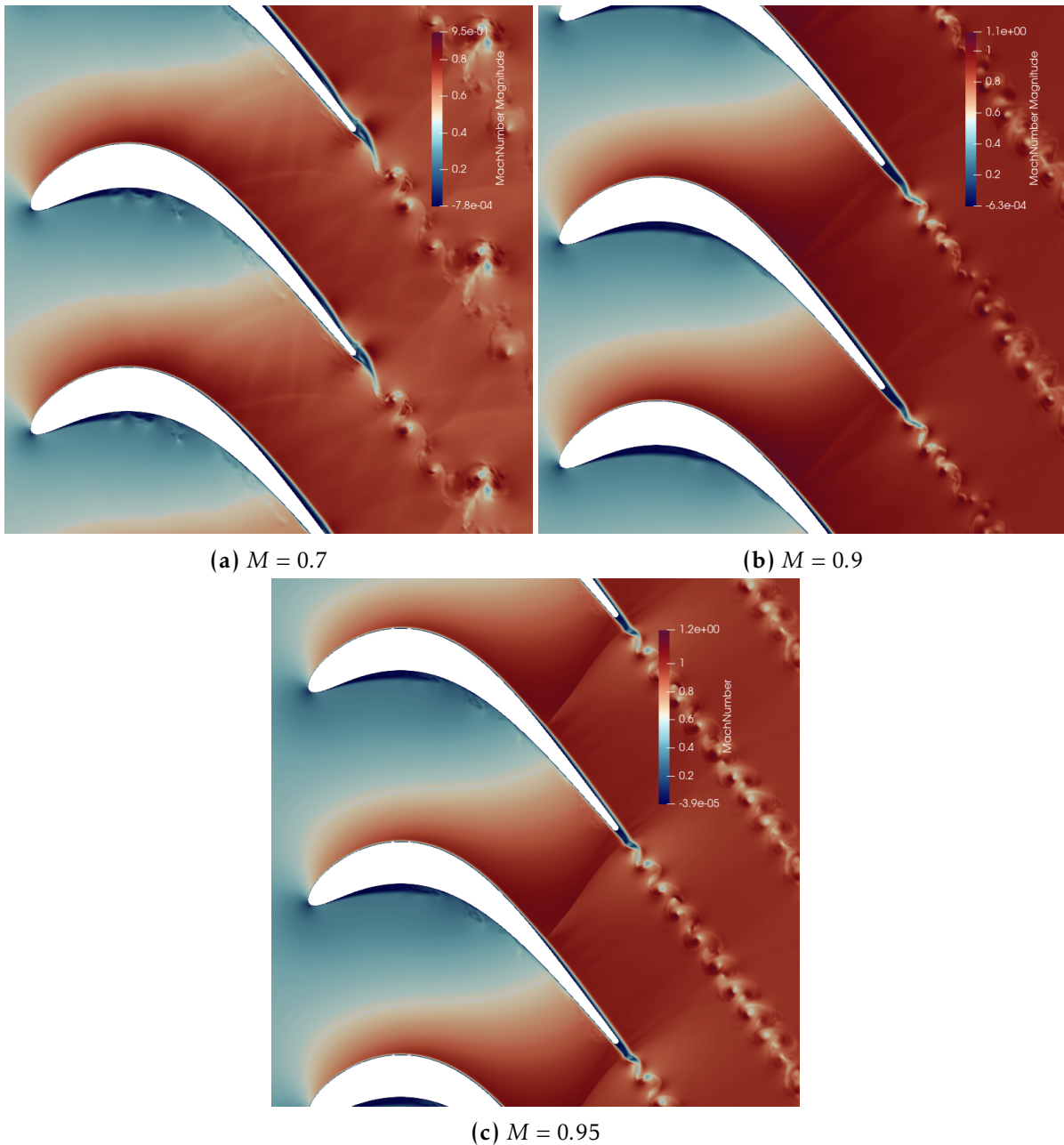
Figure 5.1: Contour of the Mach number M in the passage for $Re = 70 \cdot 10^3$, $M = 0.7$ (a) and $M = 0.9$ (b) and $M = 0.95$ (c).

for $M = 0.9$ and $M = 0.95$ are characterized by a shock developing from the SS up to the TE of the next blade. At $M = 0.95$, another shock develops from the TE on the SS and interacts with the wake of the adjacent blade. The location corresponds to the throat of the passage, where sonic velocities are reached. This shock prevent the acoustic perturbations created by vortex shedding in the wake to go upstream, which results in a cleaner flow in the passage. This could be the origin of the stronger shedding for the low Mach case, i.e. the traveling upstream disturbances may interact with the PS separation bubble, forming stronger turbulent structures. For the two highest outlet isentropic Mach numbers, the steep gradients at the TE due to the shock and delay the vortex shedding after the TE. This is more pronounced for the

$M = 0.9$ case, although the density gradients are weaker at TE. Actually, this is related to the status of the BL on the SS. At $M = 0.7$, the flow is attached and shedding interacts with the bubble because it is very close to the TE. At $M = 0.9$, the flow should be separated. Therefore, there is a larger stagnation region behind the TE of the blade and the shedding is delayed. Moreover separation of the base flow is also more prominent for this case.

Figure 5.2 shows snapshots of the vorticity in the flow field for the three cases. Separation over the PS is clearly visible by the shear layers at the interfaces with the freestream. For the

(a) $M = 0.7$ (b) $M = 0.9$

(c) $M = 0.95$
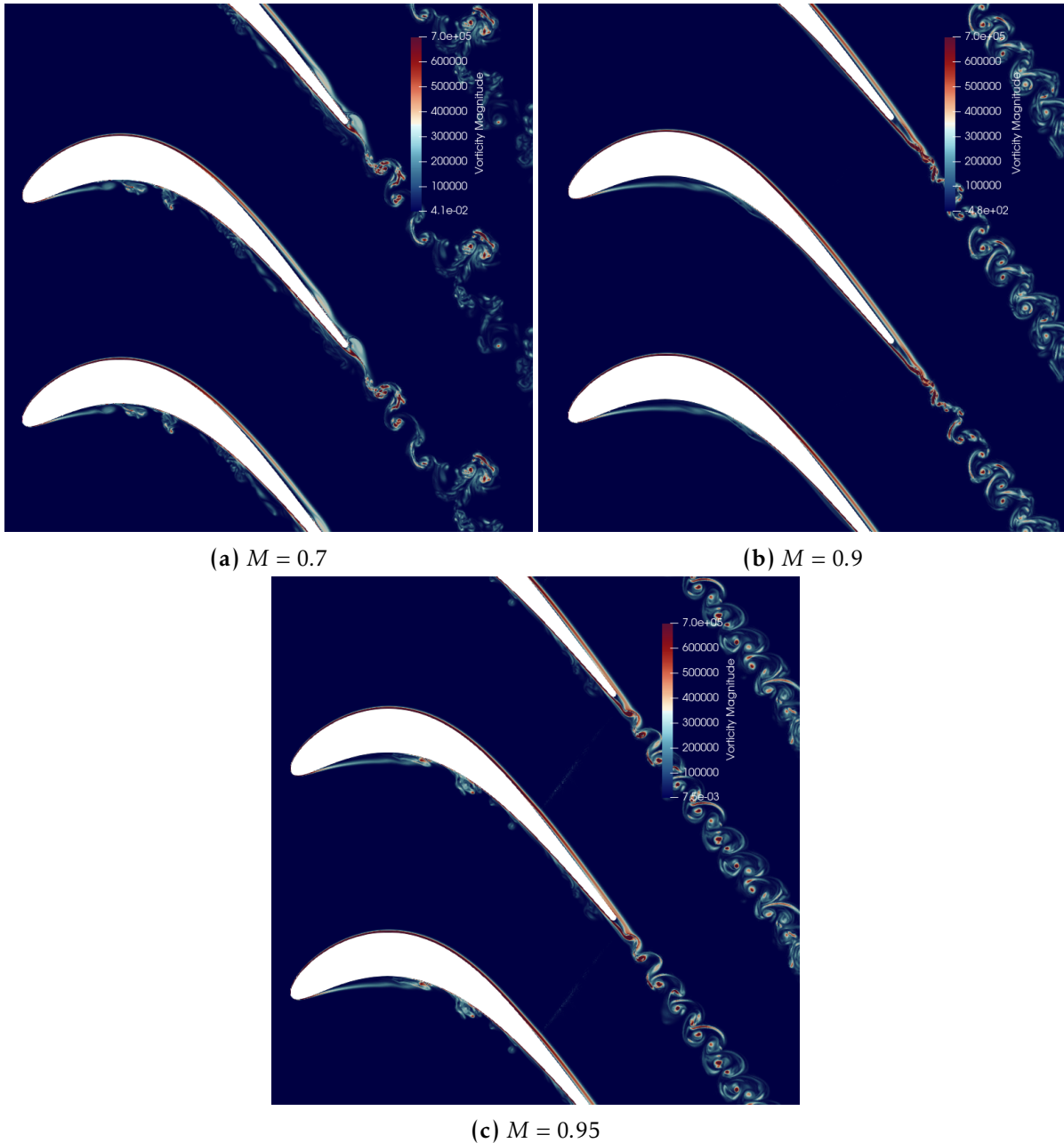
Figure 5.2: Contour of vorticity in the passage for Re $= 70 \cdot 10^3$, $M = 0.7$ (a) and $M = 0.9$ (b) and $M = 0.95$ (c).

low Mach number case, turbulent structures are formed quite soon while this phenomenon is delayed for the high Mach number case. For the moderate Mach number case, this phenomenon is not clearly seen. Separation on the SS for the low Mach number case is also distinguished by

the shear layer, which ends by vortex roll up in front of the the TE. Separation is also seen for the moderate Mach number case. However, for the high Mach number case it cannot be stated. In addition, the same observations as above can be done for the wake.

Figure 5.3 gives snapshots of the density gradients in the flow field for the three conditions. Acoustic perturbations are much more visible and permit to see that the three flows are different in nature. Indeed for the low Mach number case, acoustic perturbations that are

(a) $M = 0.7$ (b) $M = 0.9$

(c) $M = 0.95$
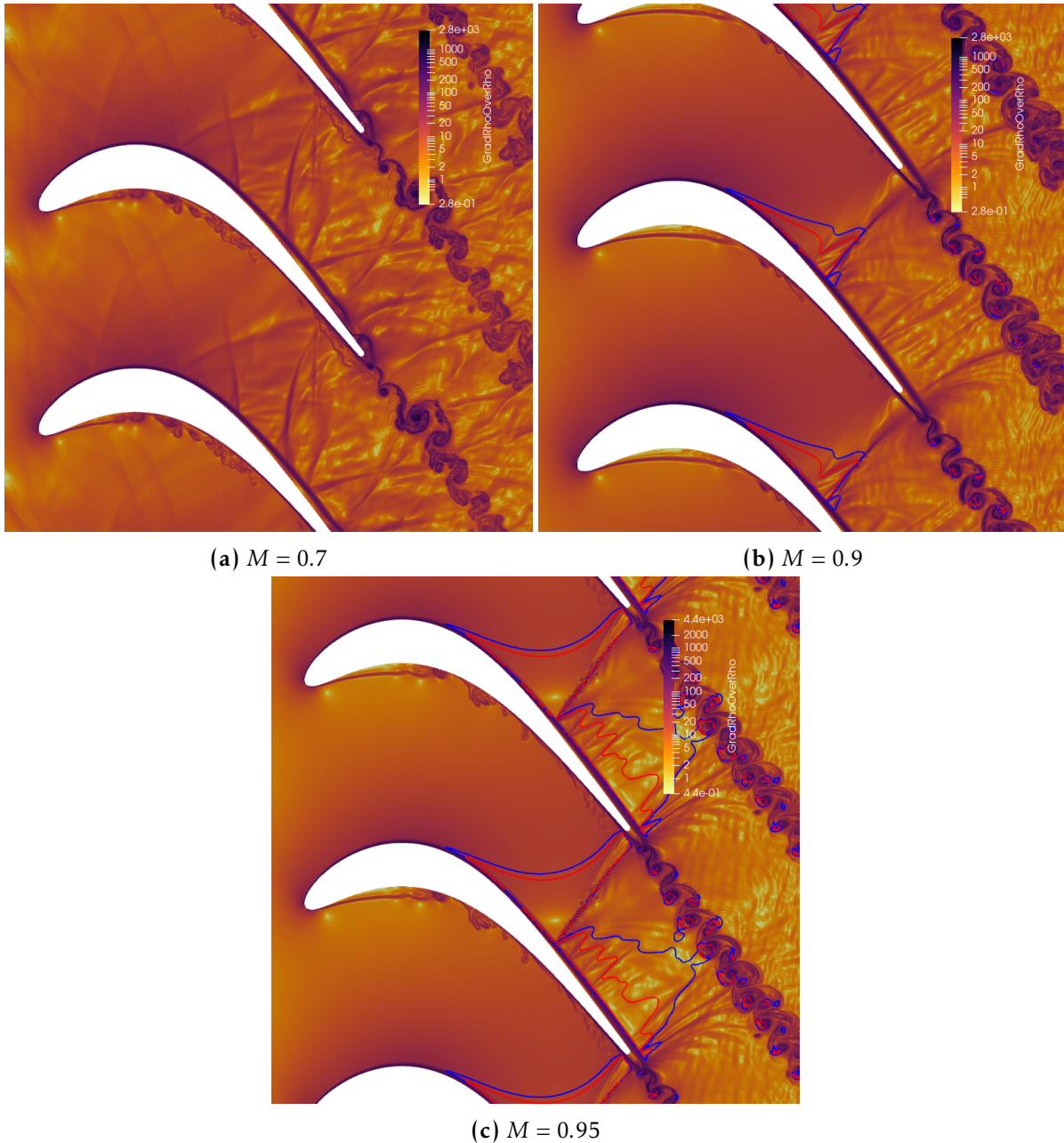
Figure 5.3: Contour of $\nabla \rho / \rho$ in the passage for Re $= 70 \cdot 10^3$, $M = 0.7$ (a) and $M = 0.9$ (b) and $M = 0.95$. In (b) and (c), the bleue lines correspond to the contours of $M = 0.99$, the red lines correspond to the contours of $M = 1.01$.

formed in the shedding region of the blade wake can propagate downstream at a velocity $U + a$, where U is the velocity magnitude of the flow and a is the speed of sound. They are also able to propagated upstream with a velocity $a - U$ although they are dissipated at the front of the

blade. Their reflective property is assessed by the "V" shapes formed on the blade SS. These shapes are due to vortex shedding at TE, just above of the SS, which involve density perturbation that propagate along a sphere (circle in two dimensions). This behavior is not observed for the higher Mach number cases because of the shock that occurs at the throat of the passage (roughly at $S/S_L \approx 0.7$). For the high Mach number case, the passage is choked, i.e. sonic conditions are reached at throat for each pitch as suggested by the contours of $M = 0.99$ and 1.01 in Figure 5.3c. Figure 5.3b shows that it is not the case for $M = 0.9$.

5.2 Blade loading

The blade loading is studied thanks to the isentropic Mach number distribution along the blade in terms of time and spanwise averages of in term of space-time diagrams at midspan.

Figure 5.4 gives the time and spanwise averages of the numerical and experimental isentropic Mach distribution for the three conditions. The upper curve corresponds to the SS while the lower corresponds to the PS.
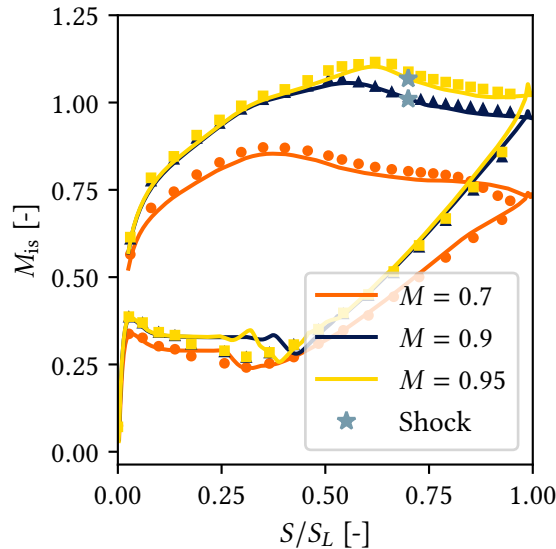
Figure 5.4: Time and spanwise averages of the isentropic Mach number and static pressure distribution along the blade for Re = $70 \cdot 10^3$ and $M = 0.7$, 0.9 and 0.95. Symbols represent the experimental measurements acquired in [43, 44]. The shocks are located by the star symbols.

On the PS for the three cases, agreement concerning the separation bubble is found with the previous visualization of the flow. This separation bubble is not predicted by the experimental curve for which there is no plateau in the pressure distribution. This might be due to the fact that experimental test case uses an inlet turbulence level of Tu = 2.5% while there is no injected turbulence in the numerical setup. For this reason, the mixing is more important in experimental conditions which should permit to avoid separation. Besides, for the remaining part of the PS, pressure are matching well even if it is slightly underestimated in numerical results.

The suction side results show also a good match with experimental results for $M = 0.9$ and 0.95. However, a small gap is observed for the low Mach number case. Moreover, the pressure recovery is not seen for this case while it is in experimental results. The effect of increase the Mach number, that was already stated in several previous studies (see [44]), is to shift the

velocity peak. For this reason, the adverse pressure gradient develops on a smaller part of the blade as the Mach number increases. In contrast, due to the very similar evolution at the front part of the blade suction side up to the suction peak at $M = 0.9$, the pressure rise between the suction peak and the trailing edge is smaller than one could expect.

Moreover, it has to be noted that turbulence seems to be significant at low Mach numbers. Indeed, turbulence plays an important role in the extent of separation bubble at low Mach numbers. The lower turbulence in the numerical simulations results in lower turbulent spots production which in turn results in a larger extent transition. The fact that the BL does not become turbulent results in a larger separation bubble and utlimately impacts the SS loading all the way to TE as seen in previous works, e.g. Pacciani [50].

5.3   Wall shear stress

The wall shear stress is investigated using the skin friction coefficient along the blade. First, the skin friction is time and spanwise averaged and compared with the experimental quasi-wall shear stress. Then, the time evolution of the skin friction coefficient is used to have a better view of the phenomena, especially separation. In each figure of the highest Mach cases, the average shock location is depicted with a vertical gray line. It has to be reminded that separation is determined as the location where the skin friction reaches negative values. Finally, the graphs are built in a compact way, allowing to analyze the PS and SS together. For this, the quantities are usually plotted with respect to the blade curvilinear coordinate along the PS, designated by negative abscissa, and SS, designated by positive abscissa.

Figure 5.5 provides the time and spanwise averages of skin friction along the PS (negative abscissa) and SS (positive abscissa) for the three cases. The solid lines correspond to the magnitude of skin friction (always positive), while the dashed lines correspond to the skin friction parallel to the blade, considering its sign. The shaded regions are delimited by the maximum and minimum values of $c_{f,s}$ for each case.

The same trends are observed for these three. Referring to Section 2.4, separation can be located thanks to negative values of $c_{f,s}$. Such conditions are reached on the SS at $M = 0.7$ at $S/S_L \approx 0.584$ and at $M = 0.9$ at $S/S_L \approx 0.688$. Over the SS, the skin friction shows a conventional shape, i.e. a decrease in the front part of the SS, separation (or very low values), stagnation in the rear part of the SS after separation (if any) and slight growth close to the TE. The shift in separation between the low and moderate Mach number cases is due to the shift in velocity peak at high Mach numbers. A consequence of this is stronger gradients at the highest Mach number than for low Mach number cases for which the slope in the region before separation is more progressive. This trend is also observed in Figure 5.4. The skin friction is characterized by highly oscillating values for the low Mach case, suggesting transitional flow in the region of TE. It is not observed for $M = 0.9$. However it does not return to positive values before the TE such that reattachment is not triggered in average. For $M = 0.95$, the skin friction reach very small values but never equals negative values, which suggests no separation in average for these conditions. Note that the steep gradient before the low values of c_f corresponds to the location of the shock. Indeed, the shock is located by the gray line in Figures 5.5b and 5.5c. The skin friction tends to collapse at the location of the shock as the Mach number increases.

On the PS, the bubble is also observed and is in accordance with the previous statements. The large gap between maximal and minimal values also suggests a turbulent reattachment. This behavior is stronger for the low Mach case. It was also observed in Section 5.1. The bubble is thus smaller at low Mach number than at $M = 0.9$ and 0.95. Note that even if the oscillating behavior is softer for these later cases, the skin friction still oscillates, which indeed suggests turbulent reattachment. The skin friction over the PS then increases until the TE for each

(a) $M = 0.7$

(b) $M = 0.9$

(c) $M = 0.95$
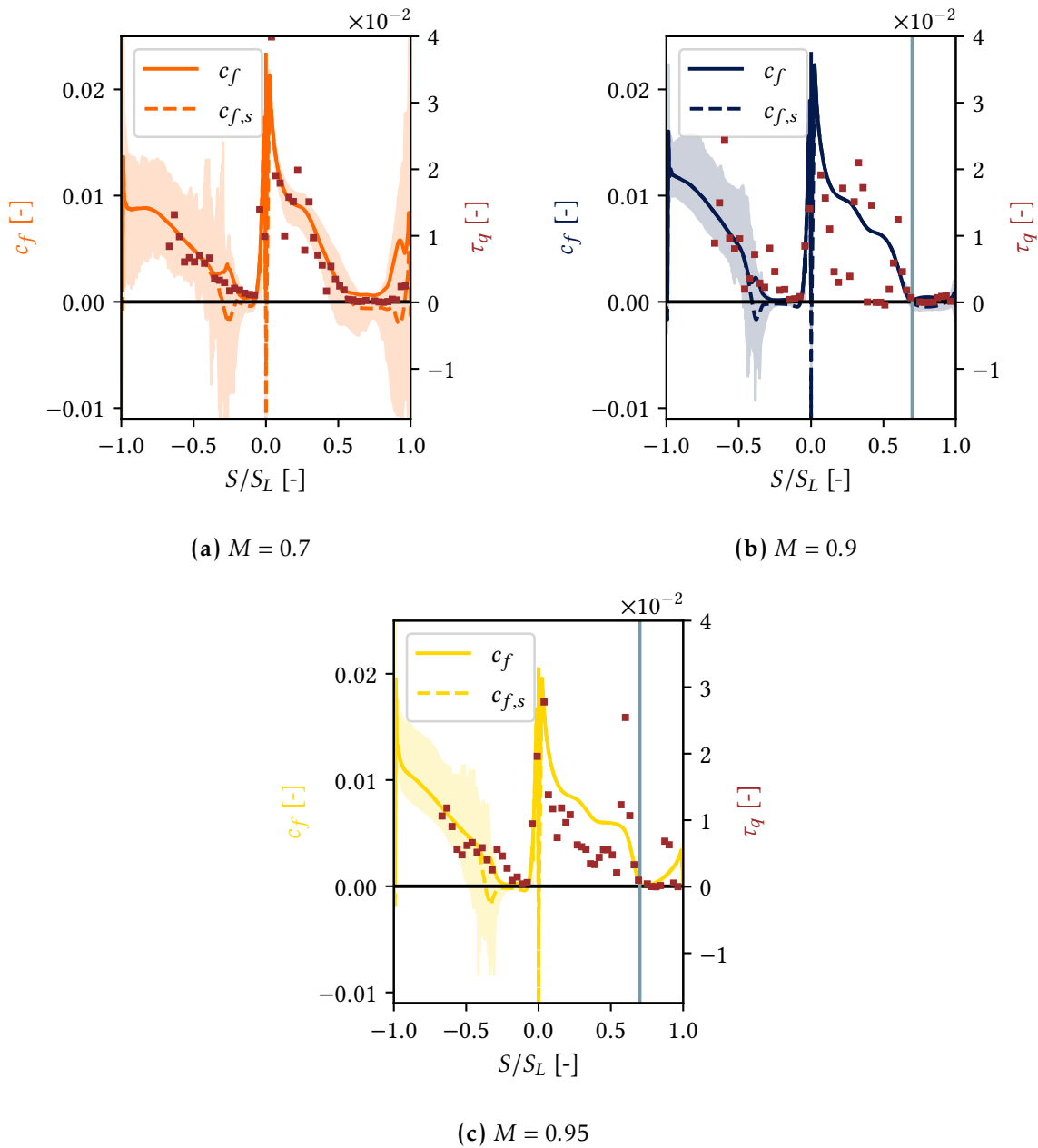
Figure 5.5: Time and spanwise averages of the skin friction coefficient along the blade for Re $= 70 \cdot 10^3$ and $M = 0.7, 0.9$ and 0.95. Shaded areas correspond to the gap between maximal and minimal computed values. Squares represents hot-films measurements of the quasi-wall shear stress τ_q acquired in [43, 44]. The shock at $M = 0.9$ and 0.95 are located by the gray line.

case. This is explained by the favorable pressure gradient that acts on the fluid in this region. Besides, it might lead to reversed transition (see next section).

The main behavior of the skin friction is well matched by the quasi-wall shear stress at low Mach. However, at higher Mach numbers, the values are quite oscillating over the SS. The PS is still well represented. The experimental data generally stay within the extrema (the shaded areas). The separation is usually well catched by experiments.

In order to have a better view of separation, the space-time diagram of wall shear stress at midspan is provided in Figure 5.6. For the low Mach number case, the separation position over

(a) $M = 0.7$

(b) $M = 0.9$

(c) $M = 0.95$
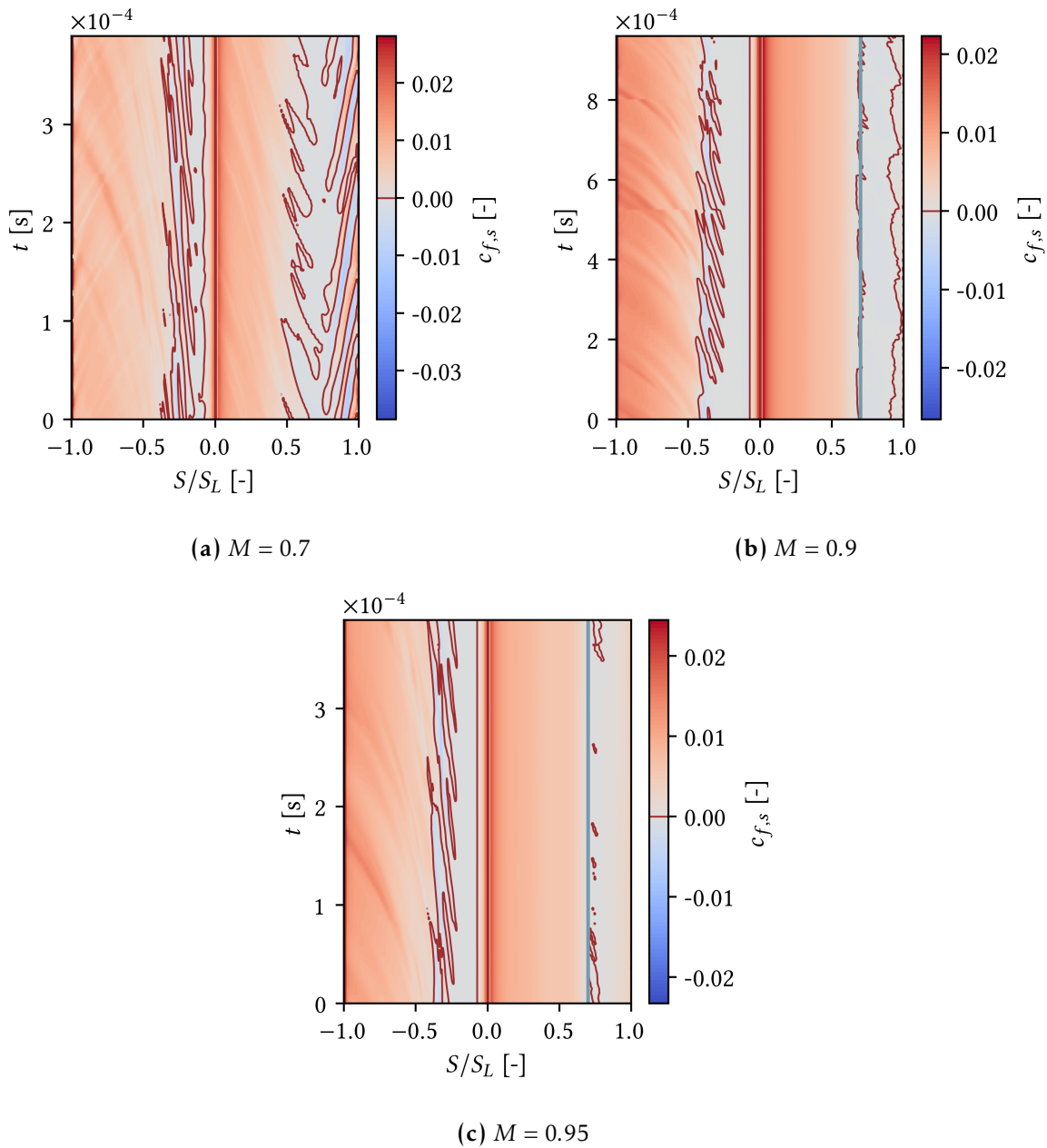
Figure 5.6: Space-time diagram of the wall shear stress at mid-span for Re $= 70 \cdot 10^3$ and $M = 0.7$, 0.9 and 0.95. The shocks are shown by the gray line.

the SS is not constant. This is also the case of the reattachment location. Figure 5.5 shows very low values of c_f at TE. This result combined with the space-time diagram allow to conclude that reattachment is periodic, i.e. the separation bubble periodically burst. Some perturbations are able to go upstream, thanks to the subsonic encountered velocities. The bubble at the front of PS is quite messy, with vortices detaching and flowing downstream, as shown in Figure 5.1a. This directly echoes the statements made in the flow visualization: acoustic perturbations are able to go upstream.

For the moderate Mach number case, the separation position is less variable than for the low Mach case. The reattachment location is variable as well, but this behavior is softer than at low Mach. The separation location well matches with the average shock location. On the PS,

the bubble is cleaner and also experiences vortex shedding at reattachment.

Finally, the high Mach number case seldom reaches separation conditions on the SS. Small bubble sometimes form after the average shock location but their extent is small. The same behavior as for the other case is observed on PS. This was also observed by Khateeb [35].

5.4 Boundary layer

This section aims to describe separation and transition in the BL with time and spanwise averaged data extracted using ParaView. As in the previous section, the results are usually presented along the SS and PS with respect to the curvilinear coordinate. Negative values of the latter correspond to the PS while positive values correspond to the SS. Moreover, it has to be noted that the data extracted from ParaView have been transformed to be able to express them in wall coordinates. Indeed, in the following figures, y refers to the distance to blade surface and u refers to the velocity parallel to the surface.

Figure 5.7 shows the velocity profiles over the PS (negative values of S/S_L) and the SS (positive values of S/S_L) for the three Mach number cases. The profiles adopt conventional shapes, referring to Chapter 2. Separation can be located by the inflexion points at the wall. If such inflexion points are observed, it means that the flow is subject to inflexional instability and KH rollups, detailed in [60]. The above-mentionned separation bubble over the PS is visible for all cases. It starts early after the LE and reattaches before the mid-chord. It can be seen that the bubble is thicker for the highest Mach numbers, which was observed in Section 5.1. In every case, the separation at TE due to vortex shedding is also present in the velocity profiles.

As expected, the SS experiences different phenomena in function of the conditions. At $M = 0.7$, according to the previous discussions, separation occurs and the flow reattaches periodically just in front of TE. The TE speed profile is a witness to this, as it does not have a fully attached shape. It has to be reminded that the data are time and spanwise averaged. At $M = 0.9$, the separation can easily be seen as well. In average, the velocity profile has not the shape of a reattached flow. The bubble is shifted downstream compared to the lower Mach number case, which shows that the transition has a smaller distance to develop before TE. The highest Mach number case is characterized by no separation over the SS, as discussed above. However, the velocity profiles are unstable, as suggested by their shape around 75% of the SS. This location also corresponds to the shock region.

In order to have a better understanding of the state of the BL and its behavior in the face of separation, the integral parameters, defined in Chapter 2, have been computed and displayed in Figure 5.8. Again, PS (resp. SS) corresponds to negative (resp. positive) values of S/S_L. It should be recalled that H takes values greater than 2 for laminar BL and lower than 2, around 1.4 for turbulent BL.

Over the pressure side, the behavior is quite similar for each case and is very interesting to discuss. After separation, the displacement thickness reach large values, which was expected from the later discussions about the thick bubble. The reached values are lower at $M = 0.7$, wich was also expected. However, the momentum thickness growth is delayed compared to that of the displcament thickness. At first, the shape factor follows the same trend as the latter. Afterwards, the displacement thickness dramatically decreases while momentum thickness gets closer to it: transition has begun. In the reattachment region, the shape factor falls below 2, close to 1.4: the flow is fully turbulent. It is clear that, in the sense of Mayle [47] as well as Hatman and Wang [24], the reattachment is permitted thanks to transition, while the separation is laminar. After reattachment, the shape factor monotonously grows until reaching values close to 2 at TE. This observation suggests that the flow experiences a reverse transition in this region. This kind of transition can only happen in favorable pressure gradient as discussed in

(a) $M = 0.7$

(b) $M = 0.9$

(c) $M = 0.95$
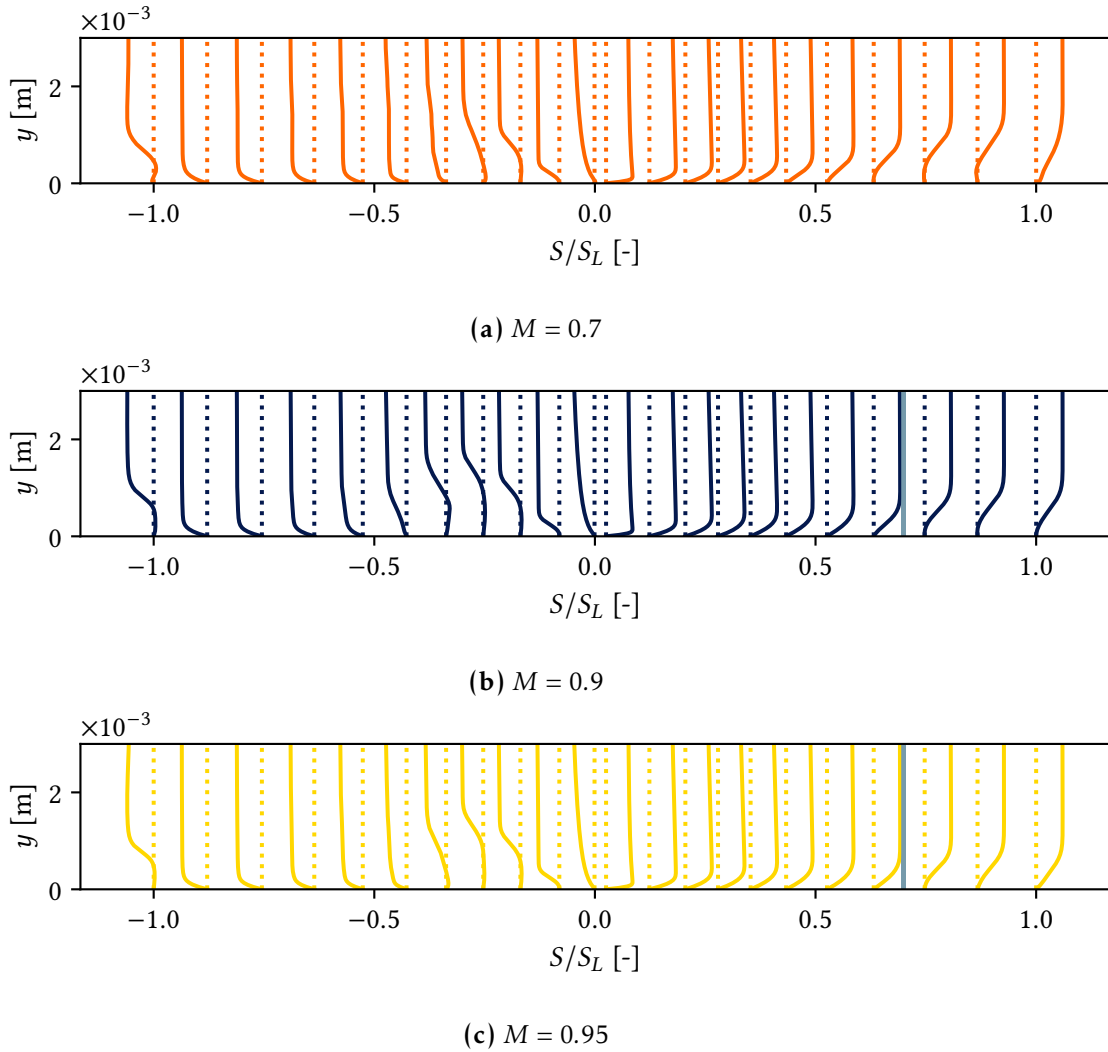
Figure 5.7: Boundary layer velocity profile u/U at different locations of the PS (negative values of S/S_L) and the SS (positive values of S/S_L) for Re $= 70 \cdot 10^3$ and $M = 0.7$, 0.9 and 0.95.

Chapter 2 and in [24, 47]. This occurs at each Mach number.

The BL parameters have a similar behavior face to separation over the SS. At $M = 0.7$, the shape factor is close to 2 before separation, increases because of separation, reaches a maximum value, then decreases until TE. It can be seen that the displacement effect of the bubble is felt slightly upstream of separation, i.e. the shape factor starts increasing around 50% of the SS while separation occurs at 58%. The decrease in shape factor and displacement thickness shows that transition has started. However, turbulent values are not reached before TE in average. At $M = 0.9$, the same observations may be made. However in this case the transition is even less developed than at low Mach. At $M = 0.95$, as already discussed, no separation occurs. However, a certain thickening of the displacement thickness and the shape factor is observed. This is due to the shock, which occurs in the same region than this growth. The gradient in shape factor is steeper than for other cases. After the shock, it reaches a maximum and decrease without reaching 2 before TE. It suggests that transition is also triggered for this case. Moreover, the shock seems to prevent separation. Indeed, values upstream the sonic region tend to collapse more and more (it may also be seen for $M = 0.9$ even if the effect is softer) which could result in a lower pressure gradient.

(a) $M = 0.7$

(b) $M = 0.9$

(c) $M = 0.95$
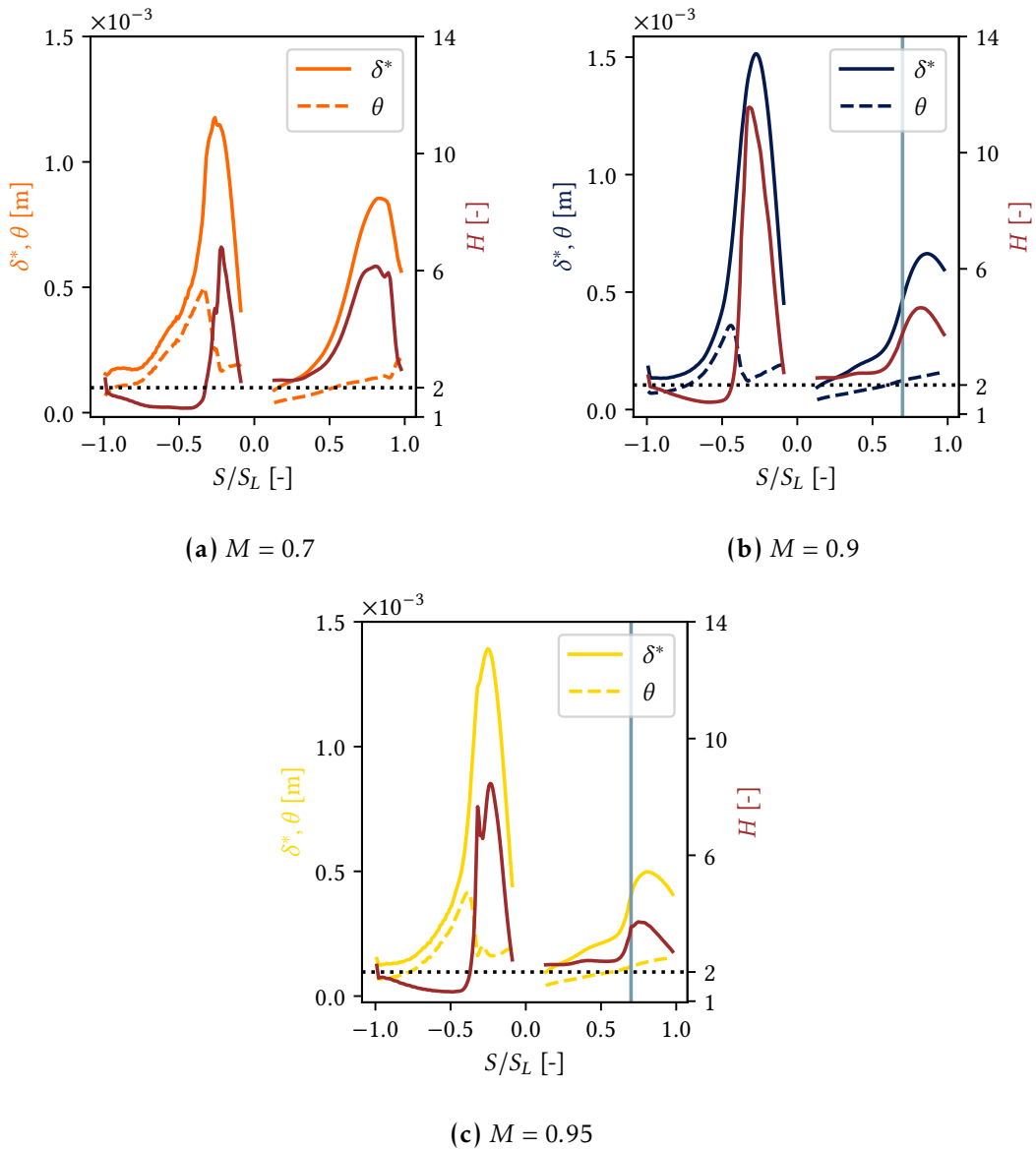
Figure 5.8: Boundary layer integral quantities along the PS (negative values of S/S_L) and the SS (positive values of S/S_L) for Re $= 70 \cdot 10^3$ and $M = 0.7$, 0.9 and 0.95. The gray line designates the average shock location.

Figure 5.9 shows the profiles of $\overline{u'u'}$, $\overline{v'v'}$ and $\overline{w'w'}$ along the PS and SS. Note that the multiplicative factors that were used to scale the profiles are not the same for SS and PS nor for each case. These profiles allow to have a better visualization of the turbulent activity in the BL and are in accordance with previous results. They increase when faced to separation, showing that the onset of transition can be located after separation. The component parallel to the blade experiences higher values than others. At $M = 0.7$, the turbulent activity is more pronounced, especially in the region of the TE. This is also observed at $M = 0.9$. At $M = 0.95$, there is also an increase that is surely due to the shock since there is no separation which again shows that the shock triggers transition and prevents separation. Along the PS, they increase then decrease because of the reverse transition. A strong turbulent activity is observed at the TE, which can be explained by the vortex shedding.

(a) $M = 0.7$

(b) $M = 0.9$

(c) $M = 0.95$
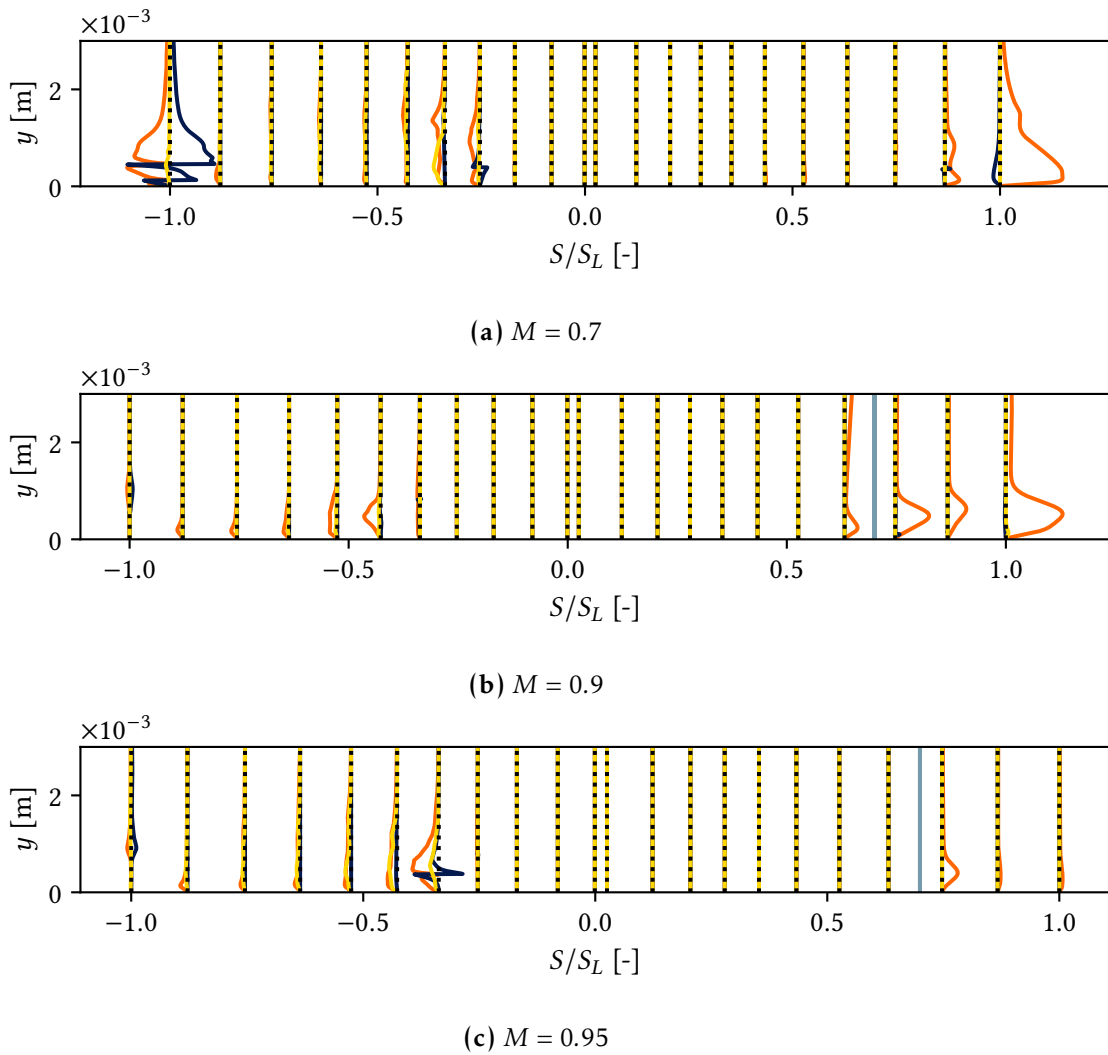
Figure 5.9: Boundary layer profile of RMS of velocity $\overline{u'u'}$, respectively in orange, $\overline{v'v'}$ in blue and $\overline{w'w'}$ in yellow, at different locations of the PS (negative values of S/S_L) and the SS (positive values of S/S_L) for Re = $70 \cdot 10^3$ and $M = 0.7$, 0.9 and 0.95. The gray line designates the average shock location.

Generally, the behavior of the BL is in line with literature observations. For example, the shapes of the curves are validated by the results of Dähnert et al. [15] which are shown in Figure 2.17. However, in this paper, the BL is fully turbulent and permits reattachment.

Finally, Figure 5.10 shows the momentum Reynolds number at separation with respect to the acceleration parameter at separation on the SS at $M = 0.7$ and 0.9. The conditions are contained in the laminar separation long bubble mode, referring to Section 2.7 and [24, 47]. This confirms the early statements about transition over the SS that have been made in the discussions above. The outer regions are discussed in Section 2.7 and shown in Table 2.1. The relatively high negative values of the acceleration parameter are evidence of the strong adverse pressure gradient that acts on the flow in the region of separation. Moreover, the low momentum Reynolds number show that the resistance of the BL to the pressure gradients in this region is not sufficient to prevent separation. Both of these parameters play an important role in separation and transition. Since the bubble mode is the laminar separation long bubble mode, according to Hatman and Wang [24], the onset of transition can be located at the position
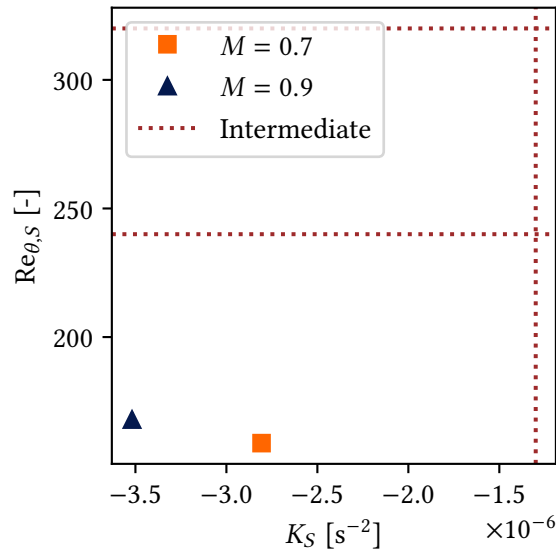
Figure 5.10: Boundary layer state at separation on the SS for the cases $M = 0.7$ and $M = 0.9$.

of maximum displacement thickness. The present results make sense in view of the previous discussions. Moreover, they are along with the literature results, e.g. [24, 32, 48, 50].
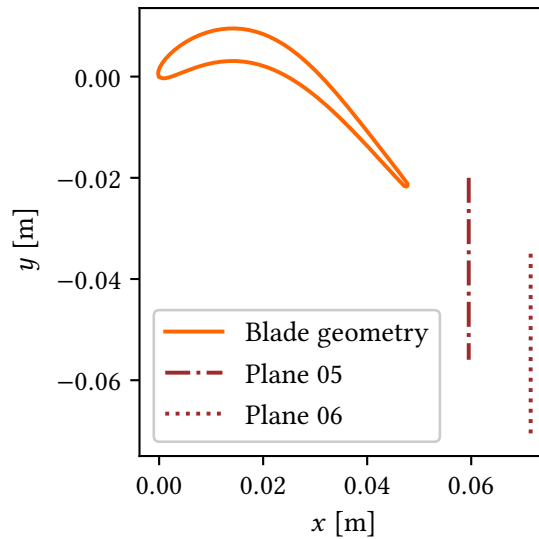
Figure 5.11: Probes locations at plane 05 and 06 for the wake analysis.

5.5 Wake analysis

The wake is investigated through time and spanwise averages of pressure defects and Reynolds stresses and preturbations of the different components of velocity. To characterize the wake as precisely as possible, and to compare the results with experiments, the planes 05 ($0.25 \cdot c_{\text{ax}}$ downstream of the TE) and 06 ($0.5 \cdot c_{\text{ax}}$ downstream of the TE) defined within the experimental

campaign (see Chapter 3) are used. They are shown in Figure 5.11. It has to be noted that the time interval over which data is collected is smaller for the high Mach case, due to time constraints.

Figure 5.12 gives the loss in the sense of total pressure defects (see the second equation of Equation 2.11) for $M = 0.7$, 0.9 and 0.95. It shows clearly that loss increase with the Mach

(a) $M = 0.7$

(b) $M = 0.9$

(c) $M = 0.95$
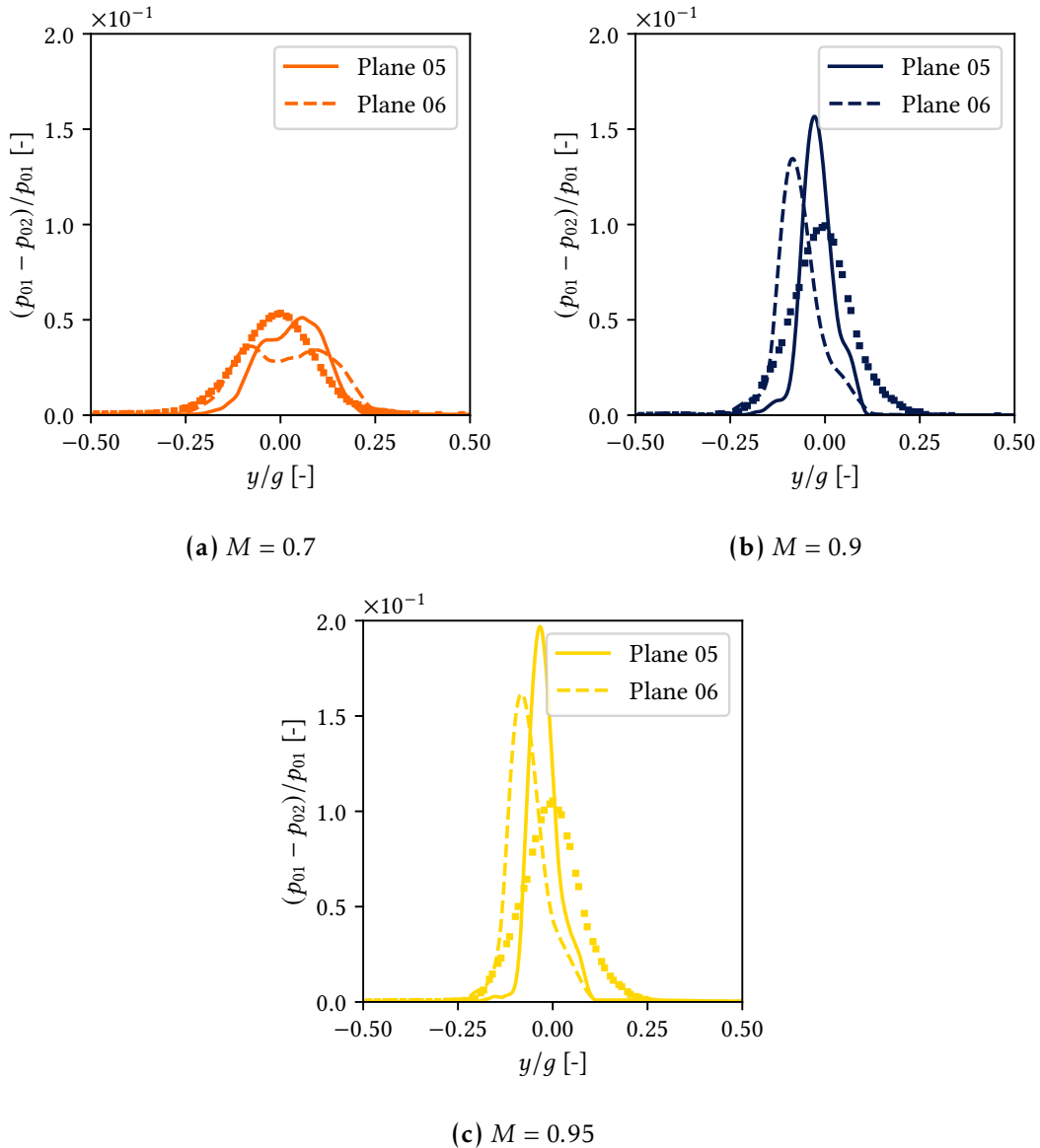
Figure 5.12: Pressure defect at plane 05 ($x = 1.25 \cdot c_{ax}$ after TE) and plane 06 ($x = 1.50 \cdot c_{ax}$ after TE) for the conditions $Re = 70 \cdot 10^3$ and $M = 0.7$, 0.9 and 0.95.

number. This statement is in line with many works, e.g. [47, 50, 62, 71, 72, 74]. Although it is not explored in this study, note that the loss also decrease as Reynolds number and the turbulent intensity increase or for a certain range of reduced frequency of incoming wakes. More information on these subjects can be found, for example, in [4, 13, 25, 32, 48, 71, 74, 82]. Figure 5.12a also shows that the wake is wider for low Mach numbers. Referring to Section 5.1, this may be related to the fact that the vortex street is much messier for this case. As discussed earlier, the vortex street is actually unstable, implying a faster turbulent decay. Moreover, it

has been shown in Figure 5.8 that at $M = 0.7$, the displacement thickness on the SS is larger than at higher Mach number. Simultaneously, the displacement thickness of the PS is smaller than at higher Mach number. For these reasons, the wake thickness decreases with M. For the two highest Mach number cases, this decay is slower, associated to a wake composed of two staggered rows of large eddies. These eddies contain big amounts of macroscopic energy that are convected downstream. This idea of a much faster decay at low Mach is backed up by the different shapes of the curve between the two downstream locations: the wake spread, but its shape change as well. It is not observed at $M = 0.9$ and 0.95. Note however that the results for $M = 0.7$ have to be interpreted carefully. Indeed, it was discussed in Chapter 4 that this case may not be fully converged. The slightly negative values of the pressure defects outside of the wake (the pitches ends) is along with this statement.

Although they are of the same order, a small gap is observed compared to experimental data. This can be explained by the inlet turbulence level issue.

(a) Plane 05

(b) Plane 06
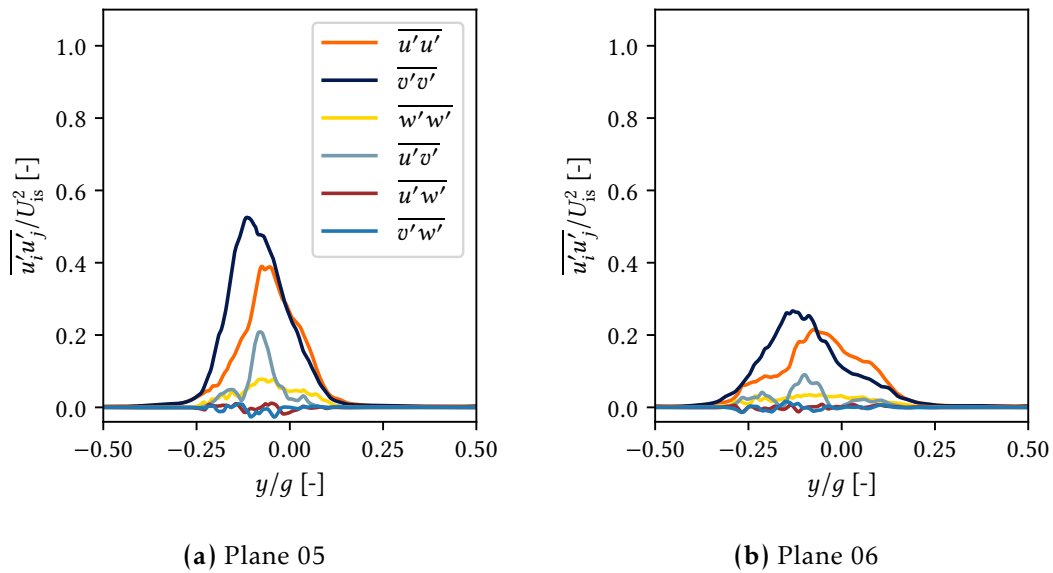
Figure 5.13: Diagonal and non-diagonal components of the Reynolds stresses tensor at planes 05 and 06 for $M = 0.7$.

Figures 5.13, 5.14 and 5.15 provide the components (diagonal and non-diagonal) of the Reynolds tensor. They emphasize on the correlation between velocity fluctuations components. Zero value means that the two considered components of velocity fluctuation are not correlated, i.e. they are never non-zero together in average. They follow the same trends as those observed above for the total pressure defects: the wake spread out in the flow direction. It is because Reynolds stresses are closely linked to turbulent decay and thus losses. For the three studied conditions, and both at plane 05 and 06, the main components that reach significant values are $\overline{u'u'}$, $\overline{v'v'}$, $\overline{w'w'}$ and $\overline{u'v'}$. The concerned components are mostly x and y components. They are due to the von Karman vortex street, which develops especially in the xy-plane. Another general observation concerns the transfer of energy happening between plane 05 and 06 that may be described in a qualitative way at this point. In a general trend, energy is transfered from the major contributors at plane 05 to the other components at plane 06. This associated to the spreading of the wake takes part to the turbulent decay.

Figure 5.13 corresponds to $M = 0.7$. The higher values of the $\overline{v'v'}$ component are surprising and may be due to the issue of convergence debated earlier. Despite of this, the curve shows clearly that the major contributors are x and y components meaning that the flow is

(a) Plane 05   **(b)** Plane 06
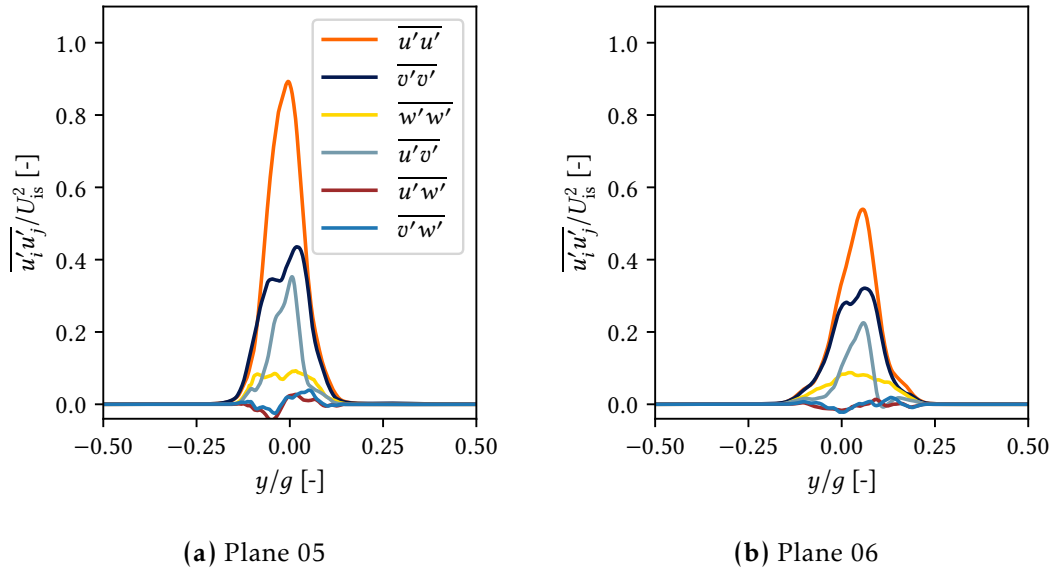
Figure 5.14: Diagonal and non-diagonal components of the Reynolds stresses tensor at planes 05 and 06 for $M = 0.9$.

(a) Plane 05   **(b)** Plane 06
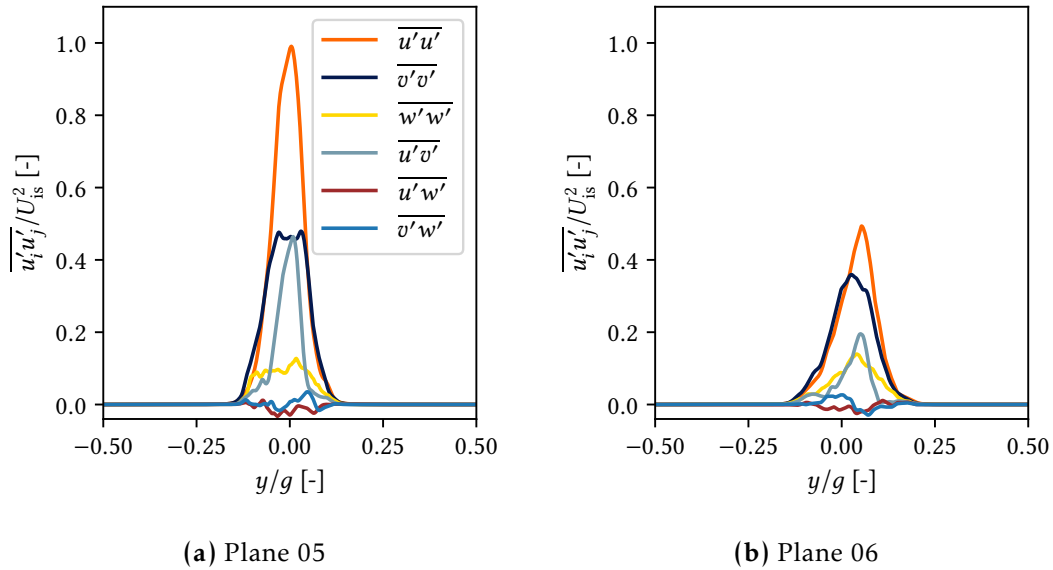
Figure 5.15: Diagonal and non-diagonal components of the Reynolds stresses tensor at planes 05 and 06 for $M = 0.95$.

highly bi-dimensional. However, a correlation exists in the spanwise direction and follows the same trends as other components between plane 05 and 06. Besides, the two last non-diagonal components are spreading as well with oscillating values, indicating the energy transfer and decay.

Figure 5.14 deals with Reynolds stresses at $M = 0.9$. Again, the results are in line with previous statements. Especially, as seen in Figure 5.12b, the spreading of the wake is slower. Moreover, there is no significant change between plane 05 and 06. This is again due to the fact that turbulent decay is slower at higher Mach number.

The same conclusion can be drawn at $M = 0.95$ (see Figure 5.15). A more interesting

observation for this case is the faster decay of the $\overline{u'u'}$ component than that of the others. More particularly, the $\overline{v'v'}$ and $\overline{w'w'}$ components do not decrease a lot between planes 05 and 06. It
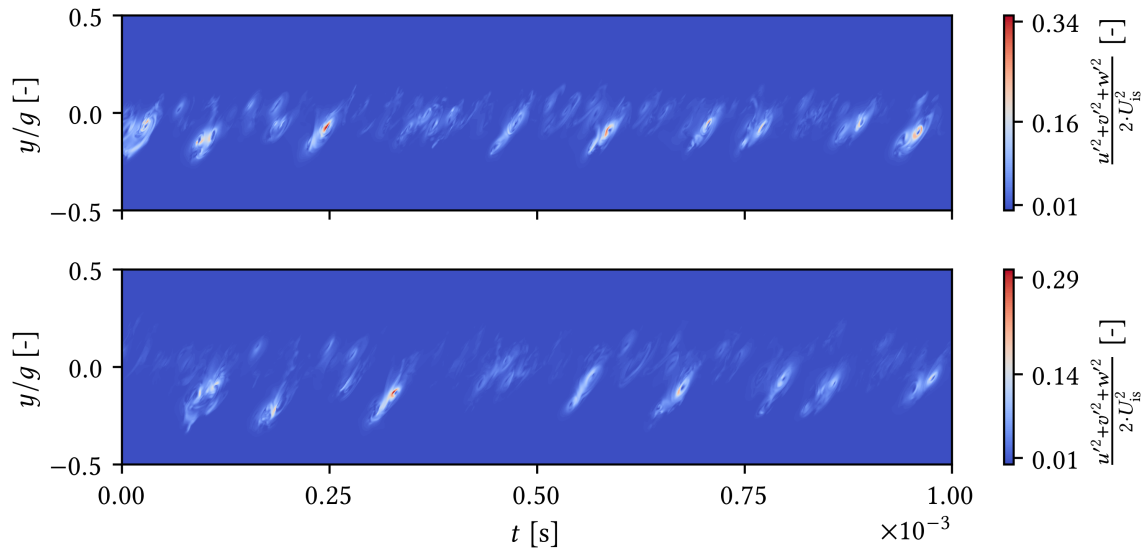
(a)
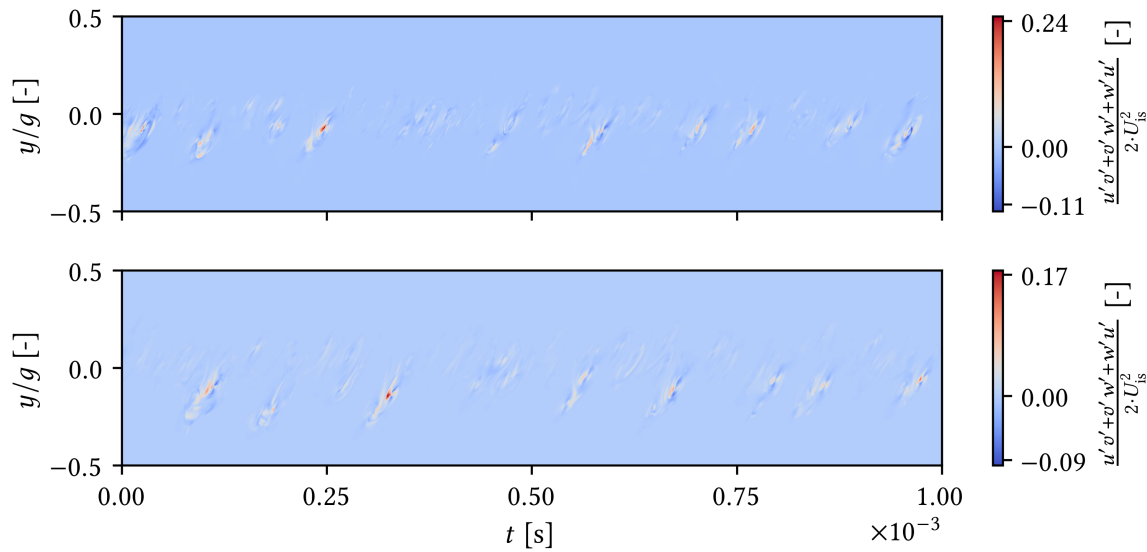
(b)

Figure 5.16: Turbulent activity, represented by $1/2 \cdot (u'^2 + v'^2 + w'^2)/U_{is}^2$ (a), and $1/2 \cdot (u'v' + v'w' + w'u')/U_{is}^2$ (b) at plane 05 (top) and 06 (bottom) for Re $= 70 \cdot 10^3$ and $M = 0.7$.

should be specified that these are based on spanwise and time averaged statistics over a time interval of 1 ms for the low and moderate Mach and 0.4 ms for the high Mach number case. The Reynolds stresses where then derived using regular averaging. However, to state of the density variations, Favre averages were computed as well. No difference were found between both averaging methods such that they weren't included in the core of the document. This means that compressibility have not a significant effect on turbulence in the wake.

The previous results provide an average quantification of losses and turbulent activity in

(a)

(b)
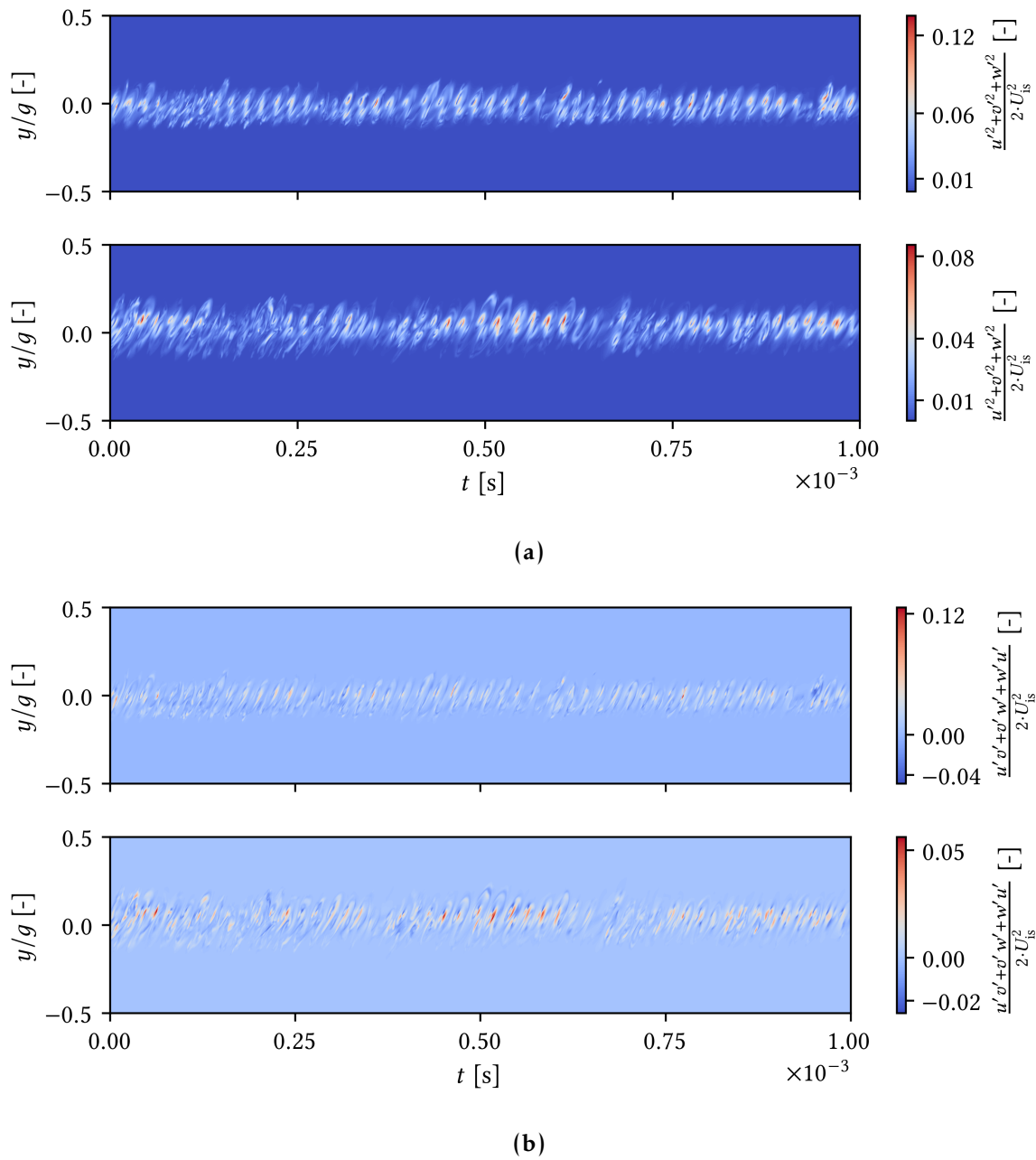
Figure 5.17: Turbulent activity, represented by $1/2 \cdot (u'^2 + v'^2 + w'^2)/U_{is}^2$ (a), and $1/2 \cdot (u'v' + v'w' + w'u')/U_{is}^2$ (b) at plane 05 (top) and 06 (bottom) for $\mathrm{Re} = 70 \cdot 10^3$ and $M = 0.9$.

the wake. However, it is also interesting to look at the time evolution of turbulence. Figures 5.16, 5.17 and 5.18 give the square of velocity perturbations at plane 05 and 06, normalized by the outlet isentropic velocity squared. They are complementary to the previous figures and consitute a good insight to the next section, which deals with spectral analysis. The choice of the first displayed quantity is backed up by the fact that its time averaged gives the turbulent kinetic energy, introduced in Chapter 2, divided by the outlet isentropic velocity squared. Similarly, the second quantity deals, in a manner of speaking, with the non-diagonal terms of the Reynolds stress tensor. Indeed, taking the time-average of these would give the different turbulent quantities given in Figures 5.13, 5.14 and 5.15. They also can be interpreted and

(a)

(b)
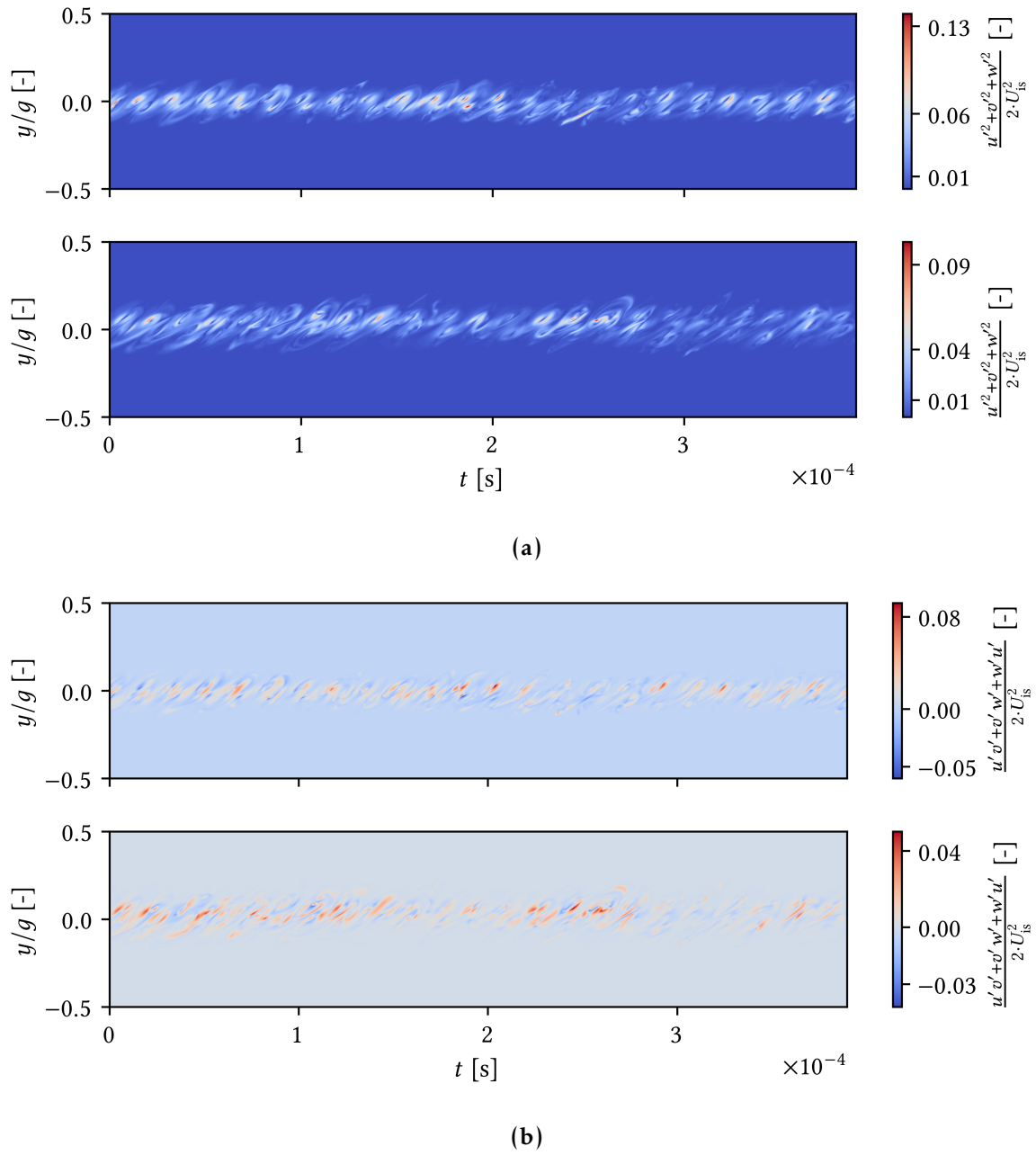
Figure 5.18: Turbulent activity, represented by $1/2\cdot(u'^2+v'^2+w'^2)/U_{\mathrm{is}}^2$ (a), and $1/2\cdot(u'v'+v'w'+w'u')/U_{\mathrm{is}}^2$ (b) at plane 05 (top) and 06 (bottom) for $\mathrm{Re}=70\cdot10^3$ and $M=0.95$.

related to diagonal (top figures) and non-diagonal (bottom figures) of the Reynolds stress tensor. It is important to note that TKE, turbulent intensity and Reynolds stresses are statistical quantities. However, the displayed quantities help to apprehend the turbulent activity passing in the wake at the plane 05 and 06 over time.

Therefore, Figure 5.16 shows the contours of the sum of the products of velocity perturbations at plane 05 and 06 for $M=0.7$. The structures contained in this figures are the passing vortices that are shedded at TE. It can be observed that their intensity is much higher in the center of the wake than in the outter region, which was expected and can also be observed in Section 5.1. Looking at top and bottom contours of Figure 5.16a and 5.16b together, it can be

seen that the passing vortices are shifted of about 0.1 ms between the two planes. Moreover, they are quickly destroyed by turbulence, as suggested by the maximum encountered value at each plane. Besides, the non-diagonal components are less important than the diagonal components. Their magnitude is however of the same order. In the end, the contours reflect the previous results, showing a decay towards the turbulence that is quite developed for this case.

Figure 5.17 deals with the moderate Mach number case. Again, the contours is representative of the previous section and the observations made in Section 5.1, i.e. a more ordered wake than at low Mach. In addition, the intensity of diagonal and non-diagonal components is two to three times smaller than for the low Mach case. This shows that the decay is less developed at high Mach number. This allows to see the details of each vortex detaching from the TE. From this, a higher shedding frequency for this case can be expected than at low Mach number.

Finally, Figure 5.18 shows these quantities for the high Mach number case. The same observations as at moderate Mach number may be made. The wake is apparently getting thinner as the Mach number increase. The outter regions is characterized by very low values of these quantities.

5.6   Spectral analysis

To conclude this study, a spectral analysis of the perturbations created in the wake and propagated upstream is proposed. This is done using Fast Fourier Transform (FFT) with the time signals introduced in the previous section. Like for the wake analysis, the plane 05 and 06, shown in Figure 5.11, are used in order to have an enlarged apprehension of the spectra. The analized time signal is the quantity

$$E = \frac{1}{2} \cdot \left(u'^2 + v'^2 + w'^2 \right), \tag{5.1}$$

computed in the wake at plane 05 and 06. The Fourier transform of the signal is shown in Figure 5.19 for the three cases. Time averages are removed in order to neglect the static signal. The wake analysis showed that increasing shedding frequencies are expected as the Mach number increases. Moreover, previous discussions showed that the shedding at $M = 0.7$ is not as smooth as for other cases.

For each case, the turbulent decay may be seen. The -5/3-law, introduced in Chapter 2, is depicted to show the match with numerical results. The signal stagnates at high frequencies because of the limitations of the time discretization. The harmonics can also be seen. These are easily seen for both of the high Mach number cases. The spectra at $M = 0.7$ is however harder to read because of the early decay.

The shedding frequencies can be computed using the Equation 2.27 and the Roshko empirical correlation of Equation 2.28. For the first, the isentropic outlet velocity and the value St = 0.2 are used. For the second, the Strouhal number is firstly computed using the isentropic outlet Reynolds number. Then, using the same parameters, the frequency is computed. For both methods, the characteristic length is the TE thickness. The results are shown in Tab. 5.1. The observed values are lower than that computed with the two relations. This can be explain by the fact that these computations are based on isentropic outlet quantities. Moreover, they also assume that the boundary layer does not separates before TE. This is in line with the results of Bolyn [6].

To conclude, the FFT of E at different locations along the blade SS (see Figure 5.20d) are depicted in Figure 5.20. The main difference between the low and high Mach numbers is observed: the acoustic perturbations created by vortex shedding at the frequencies appearing in Figure 5.19 are blocked at the throat at $M = 0.9$ and 0.95. While the spectra at $M = 0.7$ are still

(a) $M = 0.7$

(b) $M = 0.9$

(c) $M = 0.95$
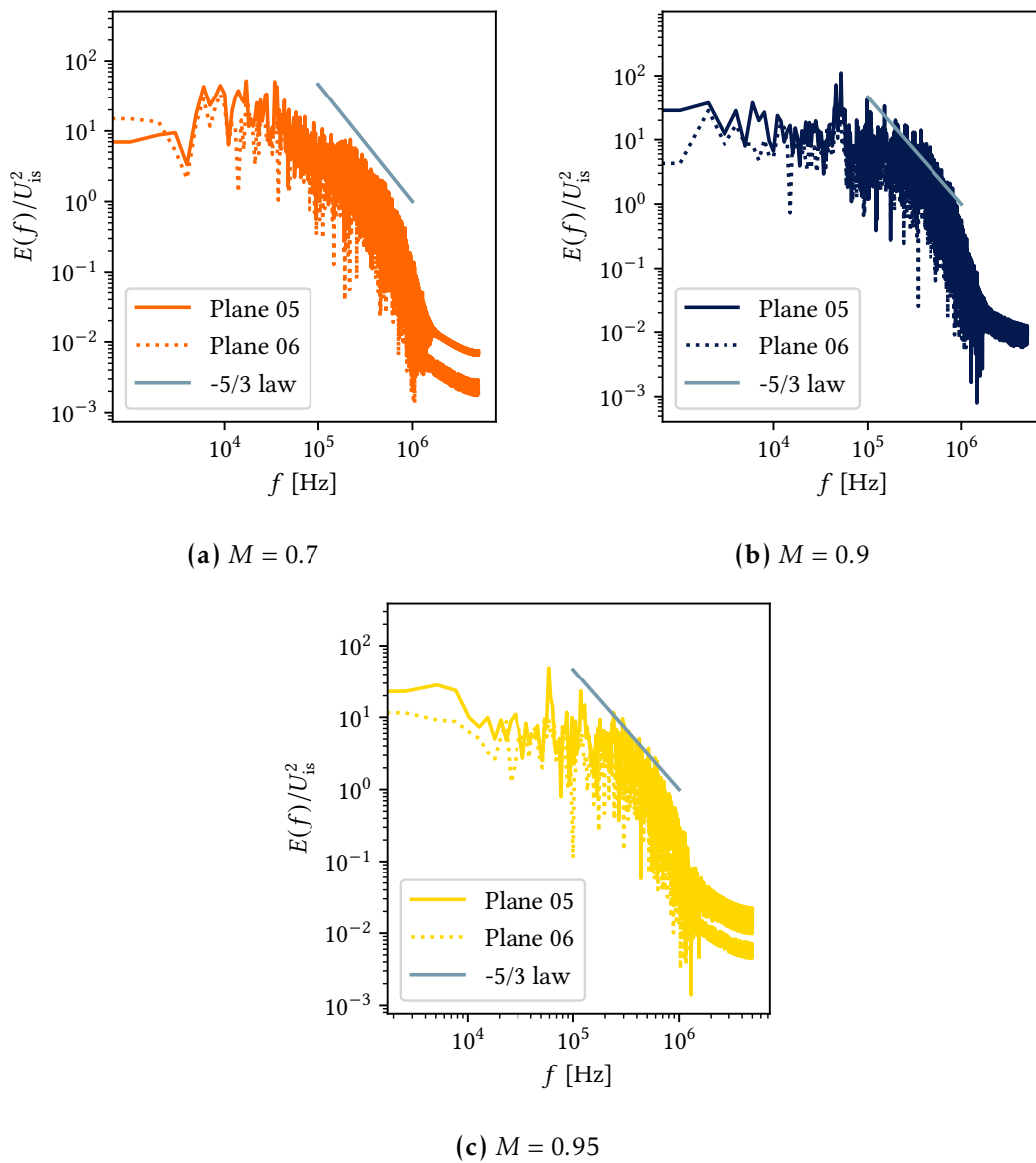
Figure 5.19: Fourier transform of the time signal of velocity perturbations at planes 05 and 06 for Re $= 70 \cdot 10^3$ and $M = 0.7$, 0.9 and 0.95.

Table 5.1 Shedding frequency computed using Strouhal relation, Roshko correlation and numerically observed.

Conditions	St $= 0.2$	St $=$ St$_{\text{Roshko}}$	Computed
$M = 0.7$	52,101 Hz	55,227 Hz	43,017 Hz
$M = 0.9$	60,763 Hz	64,409 Hz	52,031 Hz
$M = 0.95$	66,692 Hz	70,693 Hz	59,090 Hz

visible, the perturbations are less strong at $M = 0.9$ and less visible at $M = 0.95$. This observation is in accordance with Figure 5.3 and more generally with Section 5.1. The probe 3 being the closest to the throat and the shock, its curve in Figures 5.20b and 5.20c may correspond to the shock displacement since it is unsteady, as detailed in [6]. For the high Mach number case

(a) $M = 0.7$

(b) $M = 0.9$

(c) $M = 0.95$

(d) Probes locations.
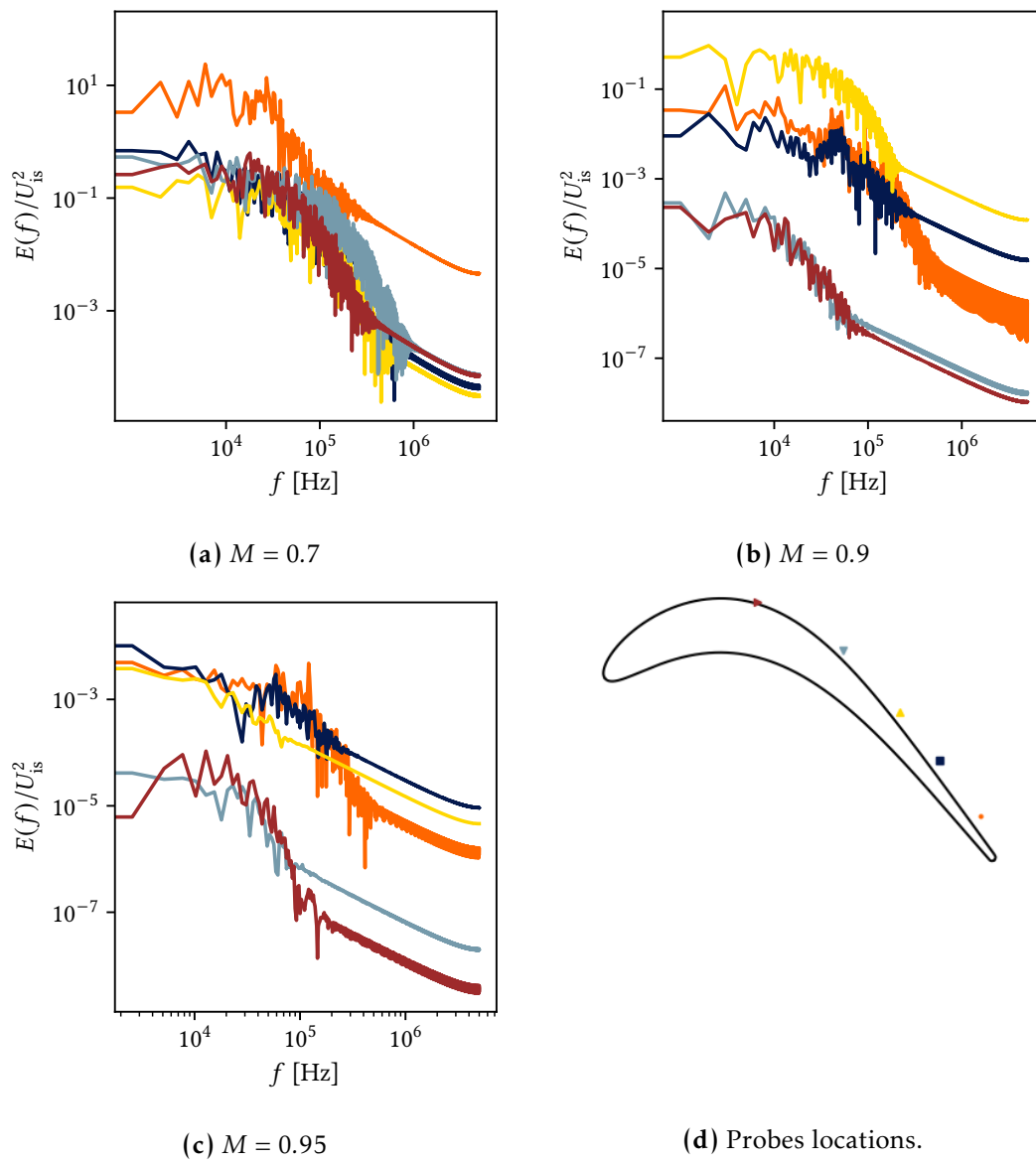
Figure 5.20: Fourier transform of the time signal of the turbulent kinetic energy at different locations over the blade SS (see (d)) for Re = $70 \cdot 10^3$ and $M = 0.7, 0.9$ and 0.95.

($M = 0.95$), the perturbations are also blocked at the TE by the shock developing on the SS.

Chapter 6

Conclusions

In conclusion, this research provides valuable insights into the interaction of separation, transition, and shock in high-speed low-pressure turbines operating in GTF under cruise conditions.

Initially, the physical and mathematical background was reviewed, covering topics such as operating conditions, performance, turbulence, boundary layer separation, wake characterization, and statistical tools. A literature review was conducted to gain an initial understanding of these concepts and assess the potential value of the current work. It was observed that, in the absence of inlet turbulence intensity, separation is likely to occur over the suction side of the LPT, resulting in significant losses. However, transition may cause the flow to reattach before reaching the TE. The acceleration parameter, accounting for pressure gradients, and the momentum Reynolds number, accounting for resistance to separation, were identified as the governing parameters influencing the different bubble modes experienced during separation. The onset of transition, mainly influenced by inflexional instability and acoustic perturbations, occurs at the maximum displacement position for the laminar separation long bubble mode, particularly when turbulent intensity is low. Losses were found to be associated with an increase in entropy and can be approximated by a drop in total pressure. An additional formula indicated that losses increase with the boundary layer momentum and displacement thicknesses, with an additional contribution if separation occurs at the TE. Moreover, losses were shown to escalate with the Mach number.

The mathematical and physical background, as well as the literature review, provided a comprehensive overview and set the foundation for the subsequent discussion in this thesis. The experimental campaign was briefly detailed to introduce the sensors, measurement locations, and operating conditions. The experimental test cases supporting this work were described. The numerical environment, ArgoDG, along with the DGM and the SIPDG, were discussed, noting that convergence was achieved for all three cases, albeit with persistent oscillations in the low Mach number case.

Subsequently, the results were analyzed and discussed. Flow visualization revealed separation occurring over the suction side at Mach 0.7 and 0.9, and over the pressure side in all cases. The wake at low Mach numbers was observed to be wider and more disordered compared to other cases. The isentropic Mach number distributions showed good agreement with experimental results, except for the separation bubble over the pressure side, which was not predicted by experiments. Increasing the Mach number resulted in shifting the velocity peak towards the TE. Skin friction confirmed separation occurring at approximately 58% and 68% of the suction side length for Mach 0.7 and 0.9, respectively, while no average separation was observed at higher Mach numbers. The separation and reattachment locations exhibited oscillations, with periodic bursting at low Mach numbers. The separation location coincided with the average shock location, and as the Mach number increased, the distribution collapsed

toward the shock, resulting in a lower pressure gradient and the absence of separation. Boundary layer profile and integral parameter analysis confirmed laminar separation over the suction side with transition occurring at the maximum displacement position. Turbulent conditions were not reached before the TE. On the pressure side, laminar separation with turbulent reattachment and reversed transition were observed for all Mach numbers until the TE. The suction side's separation bubble mode was identified as the laminar separation long bubble mode. The wake was investigated using two downstream planes, demonstrating that losses increase with the Mach number and that the wake becomes thinner. Turbulent decay was more pronounced at lower Mach numbers. Additionally, a spectral analysis revealed decay following a $-5/3$ power law and computed shedding frequencies of 43 kHz, 52 kHz, and 59 kHz. Probes placed along the suction side confirmed that acoustic perturbations are attenuated by the shock at the throat for Mach 0.9, and by the shocks at the throat and TE for Mach 0.95.

The calculations performed in this thesis utilized the DGM in conjunction with SIPDG, enabling higher order accuracy with coarser meshes compared to other methods. While the solution was found to be relatively insensitive to the position of boundaries, a more rigorous convergence study of the flow domain would be beneficial. This would involve computing spanwise correlations to investigate if turbulence remains intact within the imposed span. Additionally, it was noted that density flux exhibited oscillations at the boundaries for the low Mach number case, which could be resolved by adjusting the time step. Furthermore, optimization of time and space discretizations could be explored, considering alternative approaches to SIPDG.

Post-processing involved time sampling of 1 ms for the low Mach number cases and 0.4 ms for the high Mach number case, focusing on specific phenomena within these restricted time windows. However, larger time samples would be required to analyze lower frequencies, although the observation of higher frequencies was satisfactory. It was observed that the separation bubble on the suction side is strongly influenced by the shock, suggesting the need for a detailed study of the boundary layer in this region for future investigations. The separation bubbles on the pressure side also interact significantly with acoustic perturbations and may play a crucial role in low Mach number vortex shedding. Therefore, these computations warrant further analysis.

In conclusion, this research project successfully characterized separation, transition, and wake behavior in high-speed low-pressure turbines as part of the SPLEEN project. The findings enhance our understanding of the mechanisms governing boundary layer separation and transition on the suction and pressure sides, as well as turbulent decay and losses in the wake.

Nomenclature

Acronyms

BL   Boundary layer

CECI   Consortium des équipements de calcul intensif

CFD   Computational fluid dynamics

CPU   Central processing unit

DGM   Discontinuous Galerkin method

DNS   Direct numerical simulation

FDM   Finite difference method

FDR   Fourteen data rate

FEM   Finite element method

FNRS   Fond national de la recherche scientifique

FVM   Finite volume method

GTF   Geared turbofan

HPC   High performance computer

LES   Large eddy simulation

LKE   Laminar kinetic energy

LPT   Low pressure turbine

NSE   Navier-Stokes equations

PDE   Partial differential equation

PIV   Particle image velocimetry

PS   Pressure side

QDR   Quad data rate

RANS   Reynolds-averaged Navier-Stokes equations

SFC   Specific fuel consumption

SIPDG Symmetric interior penalty discontinuous Galerkin

SPLEEN Secondary and Leakage Flow Effects in High-SPeed Low PrEssurE TurbiNes

SS   Suction side

TFLOPS Tera floating operations per second

TO   Take-off

URANS Unsteady RANS

VKI   von Karman Institute for Fluid Dynamics

WG   Wake generator

Physical quantities

α Flow angle

δ Boundary layer thickness   m

δ^* Boundary layer displacement thickness   m

ϵ Rate of energy of the turbulent decay $\mathrm{W\,kg^{-1}}$

γ Heat capacity ratio

κ Wave number $\mathrm{m^{-1}}$

θ Boundary layer momentum thickness   m

ξ Energy loss coefficient

ζ Pressure loss coefficient

μ Dynamic viscosity $\mathrm{kg\,m^{-1}\,s}$

ν Kinematic viscosity $\mathrm{m^2\,s^{-1}}$

ρ Density $\mathrm{kg\,m^{-3}}$

τ Shear stress $\mathrm{kg\,m^{-1}\,s^{-2}}$

---

a Speed of sound $\mathrm{m\,s^{-1}}$

c True chord   m

c_ax Axial chord   m

c_f Friction coefficient

c_p Pressure coefficient

K acceleration coefficient

k Turbulent kinetic energy $\mathrm{J\,kg^{-1}}$

M	Mach number	
$n+$	Distance to the surface in wall units	
$U+$	Velocity parallel to the surface in wall units	
u_*	Friction velocity	
p	Pressure	Pa
R	Specific gas constant	$\mathrm{J\,kg^{-1}\,K^{-1}}$
Re	Reynolds number	
Ro	Roshko number	
T	Temperature	K
St	Strouhal number	
Tu	Turbulence intensity	

Other Symbols

$\frac{\mathrm{d}\cdot}{\mathrm{d}x_i}$	Total derivative with respect to the variable x_i
$\frac{\mathrm{D}\cdot}{\mathrm{D}t}$	Total derivative
$\bar{\cdot}$	Time average
$\frac{\partial\cdot}{\partial x_i}$	Partial derivative with respect to the variable x_i
in	At the inlet
is	Isentropic
out	At the outlet

List of Figures

List of Tables

Bibliography

[1] Abernethy, R. B., et al. "ASME Measurement Uncertainty." *Journal of Fluids Engineering-transactions of the Asme*, vol. 107, no. 2, ASM International, June 1985, pp. 161-64.

[2] Anderson, John, Jr. *Fundamentals of Aerodynamics*. 5th ed., McGraw-Hill, 2023.

[3] A. Sommerfeld, "Ein Beitrag zur hydrodynamische Erklärung der turbulenten Flüssigkeits-bewegungen", *Proceedings of the 4th International Congress of Mathematicians*, Rome, vol. III, 1908, p. 116-124

[4] Benyahia, Abdelkader, et al. "Prediction of Separation-Induced Transition on High Lift Low Pressure Turbine Blade." *ASME 2011 Turbo Expo: Turbine Technical Conference and Exposition*, Jan. 2011.

[5] Bellows, William J. *An Experimental Study in Leading Edge Separating-reattaching Boundary Layer Flows*. 1985.

[6] Bolyn, Alex. *Detailed Flow Analysis of a Transonic Low Pressure Turbine at Low Turbulence Levels*. University of Liège, 2020.

[7] Börner, Marcel, and Reinhard Niehuis. "Dynamics of Shock Waves Interacting With Laminar Separated Transonic Turbine Flow Investigated by High-Speed Schlieren and Surface Hot-Film Sensors." *Journal of Turbomachinery*, vol. 143, no. 5, ASM International, Apr. 2021.

[8] BSc, V. M. Falkneb, and S. W. Skan. "LXXXV.Solutions of the Boundary-layer Equations." The London, Edinburgh and Dublin Philosophical Magazine and Journal of Science, vol. 12, no. 80, Taylor and Francis, Nov. 1931, pp. 865-96.

[9] Carton De Wiart, Corentin. *Towards a Discontinuous Galerkin Solver for Scale-resolving Simulations of Moderate Reynolds Number Flows, and Application to Industrial Cases*. Université catholique de Louvain, 2014.

[10] *CECI*. ceci-hpc.be.

[11] Cobley, Keith, et al. "Design of New Three Stage Low Pressure Turbine for the BMW Rolls-Royce BR715 Turbofan Engine." *Volume 1: Aircraft Engine; Marine; Turbomachinery; Microturbines and Small Turbomachinery*, June 1997.

[12] Colignon, David, et al. (2022). *High Performance Scientific Computing* [Course lecture]. University of Liège, Liège, Belgium.

[13] Coull, John D., et al. "Velocity Distributions for Low Pressure Turbines." *Journal of Turbomachinery*, vol. 132, no. 4, ASM International, Jan. 2008.

[14] Curtis, E. M., et al. "Development of Blade Profiles for Low-Pressure Turbine Applications." *Journal of Turbomachinery*, vol. 119, no. 3, ASM International, July 1997, pp. 531-38.

[15] Dähnert, Jerrit, et al. "Transition Mechanisms in Laminar Separated Flow Under Simulated Low Pressure Turbine Aerofoil Conditions." *Journal of Turbomachinery*, vol. 135, no. 1, ASM International, Jan. 2011.

[16] Davidson, Peter. *Turbulence: An Introduction for Scientists and Engineers*. Oxford UP, USA, 2004.

[17] Denton, John D. "The 1993 IGTI Scholar Lecture: Loss Mechanisms in Turbomachines." *Journal of Turbomachinery*, vol. 115, no. 4, ASM International, Oct. 1993, pp. 621-56.

[18] DG1D_POISSON - *Discontinuous Galerkin Solution of 1D Poisson Equation*. people.math.sc.edu/Burkardt/py_src/dg1d_poisson.

[19] Dolejší, Vít, and Miloslav Feistauer. *Discontinuous Galerkin Method: Analysis and Applications to Compressible Flow*. Springer, 2015.

[20] Durbin, P., and Pettersson Reif. *Statistical Theory and Modeling for Turbulent Flows*. Hoboken, NJ, United States, Wiley, 2011.

[21] Eijkhout, Victor. *Introduction to High Performance Scientific Computing*. lulu.com, 2010.

[22] Gaster, Michael. *The Structure and Behaviour of Laminar Separation Bubbles*. 1969.

[23] Gault, Donald E. *An Experimental Investigation of Regions of Separated Laminar Flow*. 1955.

[24] Hatman, Anca, and Tao Wang. "A Prediction Model for Separated-Flow Transition." *Journal of Turbomachinery*, vol. 121, no. 3, ASM International, July 1999, pp. 594-602.

[25] Haselbach, Frank, et al. "The Application of Ultra High Lift Blading in the BR715 LP Turbine." *Journal of Turbomachinery*, vol. 124, no. 1, ASM International, June 2001, pp. 45-51.

[26] Hillewaert, Koen and Cagnone Jean-Sebastien [2018]. *CS2 - T106 LPT Cascades*, 5th International Workshop on High-Order CFD Methods.

[27] Hillewaert, Koen. *Development of the discontinuous Galerkin method for high resolution, larg scale CFD and acoustics in industrial geometries*. Université catholique de Louvain, 2013.

[28] Hillewaert, Koen (2021). *The discontinuous Galerkin method Introduction to the theory and practice* [Course lecture]. University of Liège, Liège, Belgium.

[29] Hirsch, Charles. *Numerical Computation of Internal and External Flows: The Fundamentals of Computational Fluid Dynamics*, *Volume 1*. Butterworth-Heinemann, 2007.

[30] Hodson, and Dominy. "Three-Dimensional Flow in a Low-Pressure Turbine Cascade at Its Design Condition." *Journal of Turbomachinery*, vol. 109, 1987, p. 177-85.

[31] Hodson, Howard P., and Robert Dominy. "The Off-Design Performance of a Low-Pressure Turbine Cascade." *Journal of Turbomachinery*, vol. 109, no. 2, ASM International, Apr. 1987, pp. 201-09.

[32] Houtermans, Régis, et al. "Aerodynamic Performance of a Very High Lift Low Pressure Turbine Blade With Emphasis on Separation Prediction." *Transactions of the ASME*, vol. 126, no. 3, Jan. 2004, p. 406.

[33] Howell, Robert, et al. "Boundary Layer Development in the BR710 and BR715 LP Turbines—The Implementation of High-Lift and Ultra-High-Lift Concepts." *Journal of Turbomachinery*, vol. 124, no. 3, ASM International, July 2002, pp. 385-92.

[34] Jean, Hourmouziadis. "Aerodynamic Design of Low Pressure Turbines." *AGARD Lecture Series*, vol. 187, 1989.

[35] Khateeb, Mohammed. *Impact of Operating Conditions on the Transitional Flow in a Low-pressure Fast Turbine Cascade*. University of Liège, 2021.

[36] Kolmogorov, A. N. "The Local Structure of Turbulence in Incompressible Viscous Fluid for Very Large Reynolds' Numbers." *Proceedings of the USSR Academy of Sciences*, vol. 30, Russian Academy of Sciences, Jan. 1941, pp. 301-05.

[37] Kundu, Pijush K., et al. *Fluid Mechanics*. 2015.

[38] Kurzke, Joachim. "Fundamental Differences Between Conventional and Geared Turbofans." *Volume 1: Aircraft Engine; Ceramics; Coal, Biomass and Alternative Fuels; Controls, Diagnostics and Instrumentation; Education; Electric Power; Awards and Honors*, Jan. 2009.

[39] Lavagnoli, Sergio. "SPLEEN - High Speed Turbine Cascade - Test Case Database." *Zenodo*, 26 Nov. 2022, doi.org/10.5281/zenodo.

[40] Lavagnoli, Sergio, et al. "Technical Summary of the Instrumentation, Measurement Techniques and Data Reduction for the Experimental Test Case SPLEEN C1." *SPLEEN - High Speed Turbine Cascade - Test Case Database*, 30 Nov. 2022, zenodo.org. Accessed 6 Feb. 2023.

[41] Lavagnoli, Sergio, et al. "Technical Summary on the linear cascade test section geometry and dimensional control of the manufactured cascade hardware." *SPLEEN - High Speed Turbine Cascade - Test Case Database*, 30 Nov. 2022, zenodo.org. Accessed 6 Feb. 2023.

[42] Lopes, G., et al. "*Instrumentation Interference in a Transonic Linear Cascade*".

[43] Loris Simonassi et al. « An experimental test case for transonic low-pressure turbines - part I : Rig Design, instrumentation and experimental methodology ». In: *Volume 10B : Turbomachinery - Axial Flow Turbine Aerodynamics ; Deposition, Erosion, Fouling, and Icing ; Radial Turbomachinery Aerodynamics (2022)*.

[44] Loris Simonassi et al. « An experimental test case for transonic low-pressure turbines - part 2 : Cascade aerodynamics at on- and off-design Reynolds and Mach numbers ». In: *Volume 10B : Turbomachinery - Axial Flow Turbine Aerodynamics ; Deposition, Erosion, Fouling, and Icing ; Radial Turbomachinery Aerodynamics (2022)*.

[45] Lou, Weiliang, and Jean Hourmouziadis. "Separation Bubbles Under Steady and Periodic-Unsteady Main Flow Conditions." *Journal of Turbomachinery*, vol. 122, no. 4, ASM International, Feb. 2000, pp. 634-43.

[46] L. Prandtl, in *Verhandlungen des dritten internationalen Mathematiker-Kongresses in Heidelberg 1904*, A. Krazer, ed., Teubner, Leipzig, Germany (1905), p. 484. English trans. in *Early Developments of Modern Aerodynamics*, J. A. K. Ack- royd, B. P. Axcell, A. I. Ruban, eds., Butterworth-Heinemann, Oxford, UK (2001), p. 77.

[47] Mayle, R. E. "The 1991 IGTI Scholar Lecture: The Role of Laminar-Turbulent Transition in Gas Turbine Engines." *Journal of Turbomachinery*, vol. 113, no. 4, ASM International, Oct. 1991, pp. 509-36.

[48] Michálek, Jan, et al. "Aerodynamic Performance of a Very High Lift Low Pressure Turbine Airfoil (T106C) at Low Reynolds and High Mach Number With Effect of Free Stream Turbulence Intensity." *Journal of Turbomachinery*, vol. 134, no. 6, ASM International, Oct. 2010.

[49] Michelassi, V., et al. "Compressible Direct Numerical Simulation of Low-Pressure Turbines—Part II: Effect of Inflow Disturbances." *Journal of Turbomachinery*, vol. 137, no. 7, ASM International, June 2014.

[50] Pacciani, Roberto, et al. "A CFD Study of Low Reynolds Number Flow in High Lift Cascades." *ASME Turbo Expo 2010: Power for Land, Sea, and Air*, Oct. 2010.

[51] Pacciani, Roberto, Michele Marconcini, Alberto Arnone, et al. "An Assessment of the Laminar Kinetic Energy Concept for the Prediction of High-lift, low-Reynolds Number Cascade Flows." *Proceedings of the Institution of Mechanical Engineers, Part A: Journal of Power and Energy*, vol. 225, no. 7, SAGE Publishing, Nov. 2011, pp. 995-1003.

[52] Pope, Stephen B. *Turbulent Flows*. Cambridge UP, 2000.

[53] Pohlhausen, K. "Zur Näherungsweisen Integration Der Differentialgleichung Der Iaminaren Grenzschicht." *Journal of Applied Mathematics and Mechanics*, vol. 1, no. 4, Wiley, Jan. 1921, pp. 252-90.

[54] Prandtl, Ludwig. "Über Die Entstehung Der Turbulenz." *Journal of Applied Mathematics and Mechanics*, vol. 11, no. 6, Wiley, Jan. 1931, pp. 407-09.

[55] Pratt & Whitney. "Pratt and Whittney GTF Engine." *Pratt & Whittney*, prattwhitney.com/GTF. Accessed 14 Feb. 2023.

[56] Richardson, Lewis Fry. *Weather Prediction by Numerical Process*. Cambridge UP, 2007.

[57] Rivière, Béatrice. *Discontinuous Galerkin Methods for Solving Elliptic and Parabolic Equations: Theory and Implementation*. SIAM, 2008.

[58] Roberts, William B. "Calculation of Laminar Separation Bubbles and Their Effect on Airfoil Performance." *AIAA Journal*, vol. 18, no. 1, American Institute of Aeronautics and Astronautics, Jan. 1980, pp. 25-31.

[59] Sandberg, Richard D., et al. "Compressible Direct Numerical Simulation of Low-Pressure Turbines—Part I: Methodology." *Journal of Turbomachinery*, vol. 137, no. 5, ASM International, Sept. 2014.

[60] Schlichting, Hermann, and Klaus Gersten. *Boundary-Layer Theory*. Springer, 2016.

[61] Schlichting, H. "Zur Enstehung Der Turbulenz Bei Der Plattenströmung." *Nachrichten Von Der Gesellschaft Der Wissenschaften Zu Göttingen, Mathematisch-Physikalische Klasse*, vol. 1933, Jan. 1933, pp. 181-208.

[62] Sieverding, Claus, and Marcello Manna. "A Review on Turbine Trailing Edge Flow." *International Journal of Turbomachinery*, Propulsion and Power, vol. 5, no. 2, MDPI, May 2020, p. 10.

[63] *Supercalculateur Zenobe | Opérateur Du Supercalculateur Tier-1 De Wallonie*. tier1.cenaero.be/zenobe.

[64] Sutherland, William J. "LII. the Viscosity of Gases And Molecular Force." *The London, Edinburgh and Dublin Philosophical Magazine and Journal of Science*, vol. 36, no. 223, Taylor and Francis, Dec. 1893, pp. 507-31.

[65] Taylor, Geoffrey Ingram. "The Spectrum of Turbulence." *Proceedings of the Royal Society of London*, vol. 164, no. 919, Royal Society, Feb. 1938, pp. 476-90.

[66] Terrapon, V. and Andrianne, T. (2022). *Aerodynamics* [Course lecture]. University of Liège, Liège, Belgium.

[67] Terrapon, V. (2022). *Computational fluid dynamics* [Course lecture]. University of Liège, Liège, Belgium.

[68] Terrapon, V. (2022). *Turbulent flows* [Course lecture]. University of Liège, Liège, Belgium.

[69] Thwaites, B. "Approximate Calculation of the Laminar Boundary Layer." *The Aeronautical Quarterly*, vol. 1, no. 3, Cambridge UP, Nov. 1949, pp. 245-80.

[70] Torre, A. F. M., et al., editors. "Van-probe Interactions in Transonic Flows." *Turbomachinery Technical Conference and Exposing*, ASME, 2022.

[71] Vázquez, Raúl et al. "THE INFLUENCE OF REYNOLDS NUMBER, MACH NUMBER AND INCIDENCE EFFECTS ON LOSS PRODUCTION IN LOW PRESSURE TURBINE AIRFOILS." *Proceedings of GT2006, ASME Turbo Expo 2006: Power for Land, Sea and Air*, May 2006.

[72] Vázquez, Raúl, and Diego Torre. "The Effect of Mach Number on the Loss Generation of LP Turbines." *ASME Turbo Expo 2012: Turbine Technical Conference and Exposition*, June 2012.

[73] Vera, et al. "THE EFFECT OF MACH NUMBER ON LP TURBINE WAKE-BLADE INTERACTION." *Unsteady Aerodynamics, Aeroacoustics and Aeroelasticity of Turbomachines*, 2006, pp. 203-16.

[74] Vera, M. T., and Howard P. Hodson. "LOW SPEED VS HIGH SPEED TESTING OF LP TURBINE BLADE-WAKE INTERACTION." *The 16th Symposium on Measuring Techniques in Transonic and Supersonic Flow in Cascades and Turbomachines*, Sept. 2002.

[75] von Kármán, T., "Festigkeitsproblem im Maschinenbau," *Encyk. D. Math. Wiss*. IV, 1910, pp. 311-85

[76] Wikipedia contributors. "Geared Turbofan." *Wikipedia*, 28 Feb. 2023, wikipedia.com/GearedTurbofan.

[77] "Workload Manager and Job Scheduler for HPC | Altair PBS Professional." *Default*, altair.com/pbs-professional.

[78] W. Mc F. Orr, "The Stability or Instability of the Steady Motions of a Perfect Liquid and of a Viscous Liquid. Part I: A Perfect Liquid", *Proceedings of the Royal Irish Academy. Section A: Mathematical and Physical Sciences*, vol. 27, 1907, p. 9-68

[79] W. Mc F. Orr, "The Stability or Instability of the Steady Motions of a Perfect Liquid and of a Viscous Liquid. Part II: A Viscous Liquid", *Proceedings of the Royal Irish Academy. Section A: Mathematical and Physical Sciences*, vol. 27, 1907, p. 69-138

[80] W. Tollmien, Grenzschichttheorie. *Handbuch der Experimentalphysik*, 1931, pp. 275-79.

[81] Zdravkovich, M. M., and P. W. Bearman. "Flow Around Circular Cylinders—Volume 1: Fundamentals." *Journal of Fluids Engineering*, vol. 120, no. 1, Mar. 1998, p. 216.

[82] Zhang, Xue Feng, et al. "Unsteady Boundary Layer Studies on Ultra-high-lift Low-pressure Turbine Blades." *Proceedings of the Institution of Mechanical Engineers, Part A: Journal of Power and Energy*, vol. 219, no. 6, SAGE Publishing, Sept. 2005, pp. 451-60.